University of Stavanger

Faculty of Science and Technology

MASTER'S THESIS

Study program/Specialization: Petroleum Geosciences Engineering	Spring semester, 2016 Open
Writer: Espen Sigmundstad	(Writer's signature)
Faculty supervisor: Chris Townsend External supervisor(s):	
Title of thesis: Detailed Structural Mapping and Correlation of a Thick Syn-Rift Sequence in the Kerpini Fault Block, Greece.	
Credits (ECTS): 30	
Keywords: Gulf of Corinth LiDAR Syn-rift Structural Modelling Kerpini Fault Block	Pages: 120 +Front Page:14 Stavanger, 13.07.2016

Detailed Structural Mapping and Correlation of a Thick Syn-Rift Sequence in the Kerpini Fault Block, Greece.

by

Espen Sigmundstad, BSc.

Master Thesis

Presented to the Faculty of Science and Technology

The University of Stavanger

The University of Stavanger

July 2016

Acknowledgments

I wish to thank my supervisor Chris Townsend for his encouragement, guidance and patience throughout the course of this thesis. I would also like express my gratitude towards to co-supervisor Alejandro Escalona for all his good advice and encouragement. Also, a thanks goes to Andreas Habel for all your assistance.

Thanks to all my fellow master students at the University of Stavanger for all your support and for all the fun we have had in these last two years. A special thanks to my field partners Sindre Hadland and Stian Seglem Bjåland for our good cooperation and vivid discussions.

I would also like to thank all my friends and family for all the support and encouragement through the course of this master program.

Finally, I would like to extend a special thanks to my girlfriend Maren Stensen for your infinite support, motivation and patience these last five years.

Abstract

Detailed Structural Mapping and Correlation of a Thick Syn-Rift Sequence in the Kerpini Fault Block, Greece.

Espen Sigmundstad

The University of Stavanger

Supervisor: Chris Townsend

Roghi Mountain is a thick unit of alleged syn-rift deposits (Ford et al., 2013) located within the Kerpini Fault Block of the northern part of the Peloponnese Peninsula in Greece. The fault block bounding faults were formed in the early stages of the Corinth Rift which is presently active (Ford et al., 2013). Previous work in the region has not fully described the somewhat unusual features observed in the sedimentary succession of Roghi Mountain, nor the structural evolution of these sediments. These features include; the lack of evidence for growth strata, which is expected for a thick syn-rift sequence; a major change in the bed characteristics of the outcrops on the eastern side of Roghi Mountain compared to the beds on the western side; and distinct bed terminations within the sedimentary sequence which has been interpreted as evidence for faulting (Dahman, 2015; Syahrul, 2014).

With the use of advanced field mapping methods such as Light Detection and Ranging (LiDAR) scanning as well as traditional field mapping, the objectives of this project was to interpret, correlate and model the various units of Roghi Mountain. A workflow was generated in Petrel E&P (geological interpretation software from Schlumberger) to interpret LiDAR data and a 3D structural model of Roghi Mountain was generated.

With the field observations and the Petrel E&P workflow, five depositional sequences have been identified in the sedimentary succession of Roghi Mountain, the beds of the eastern and western profiles have been correlated and a six stage structural evolution has been described for Roghi Mountain. With these results, an increased understanding of the Kerpini Fault Block has been achieved along with improved knowledge of syn-rift structure and development in general. In addition, a workflow of interpretation and modelling based on LiDAR data in Petrel E&P has been described trough this project.

Table of Contents

List of Figures

List of Tables

Chapter 1: Introduction

In the early Pliocene the active rift of the Gulf of Corinth (Figure 1) initiated and eventually divided central Greece into its current position (Ford et al., 2013). Typical extensional rift system features, such as, rotated fault blocks and half-graben structures are evident in the landscape of the northern part of the Peloponnese peninsula with deep valleys cutting the fault blocks, perpendicular to the axis of the Corinth Rift. Although there are many well-preserved outcrops in the region, there are still areas that are not completely understood both structurally and stratigraphically, especially with regards to the chronological evolution between faulting and sedimentary infill. This project focuses on a thick sequence of supposedly syn-rift deposits (Collier and Jones, 2003; Ford et al., 2013) that make up Roghi Mountain located within the Kerpini Fault Block.

The Kerpini Fault Block (Figure 2) is one of four major fault blocks in close relation to the study area of Roghi Mountain which has formed in relation to the Corinth Rift. Pre-rift basement consist of pelagic carbonates that were deposited as a carbonate platform during the Upper Triassic-Jurassic period (Skourlis and Doutsos, 2003). During the Pliocene the main onset of the Corinth Rift initiated the development of the major east-west striking normal faults creating the four fault blocks visible in Figure 2 (Doutsos and Kokkalas, 2001; Ford et al., 2013; Leeder et al., 2008; Rohais et al., 2007; Taylor et al., 2011). The syn-rift sedimentary infill of these fault blocks vary somewhat from block to block, in general the fault blocks are mostly dominated by coarse conglomeratic alluvial/fluvial sequences.

The development of the Kerpini Fault Block is not fully understood due to the complex fault interactions of the area which in turn control its syn-rift sedimentary infill (Syahrul, 2014). Understanding the structure and development of syn-rift deposits in half graben systems is important as major hydrocarbon discoveries have been made in similar structures, for example the Edvard Grieg field in the Norwegian North Sea. This has served as the main incentive to conduct this study, and the project goals were set to contribute in increasing the geological understanding of the Kerpini Fault Block as well as syn-rift structure and evolution in half graben rift setting.

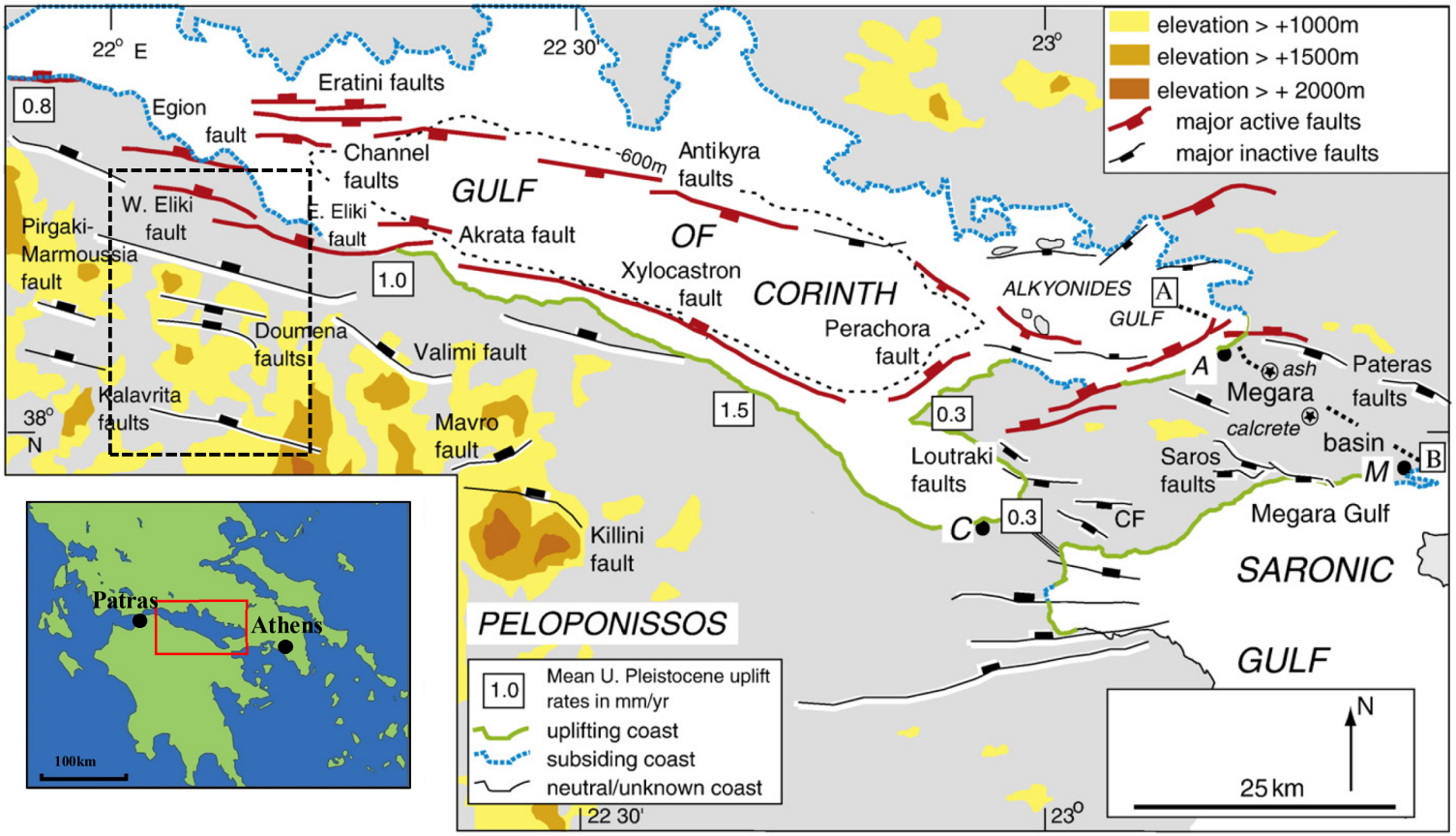

Figure 1 Overview of the Gulf of Corinth (red rectangle in small map) with active and inactive faults. Black rectangle represents map boundary in Figure 2. Fault map modified from Leeder et al. (2008), small overview map modified from Google Earth.

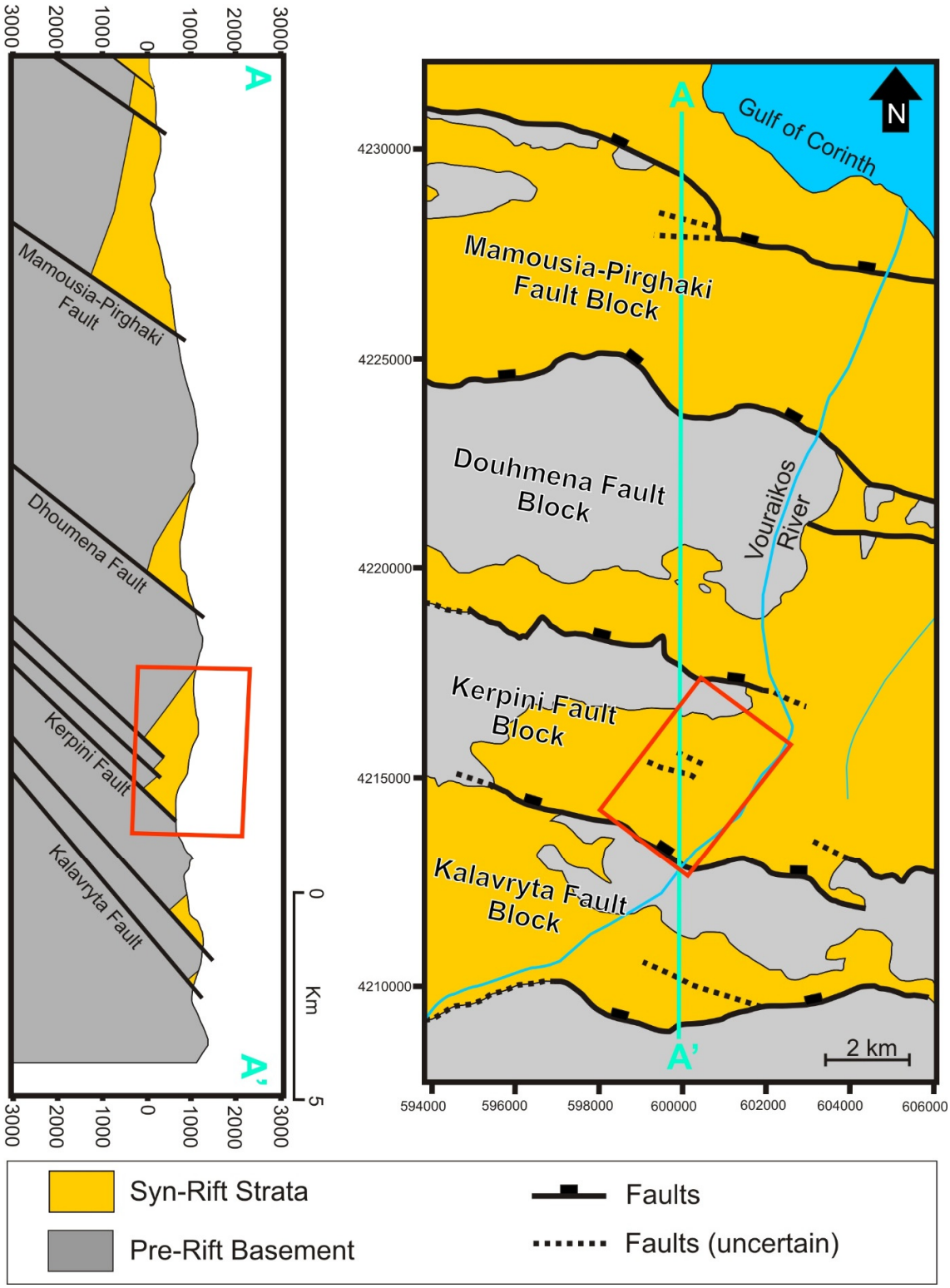

Figure 2 Map of the different fault blocks in close relation to the study area (red rectangle). Modified from (Collier and Jones, 2004).

1.1 Geological Problem and Project Challenges

Interpretation of the Roghi Mountain sedimentary outcrops, as well as the Kerpini Fault Block in general, has a number of both geological and practical issues:

1. The Roghi Mountain sedimentary outcrops have some discrepancies in relation to typical syn-rift sedimentary structure, in particular, a lack of increasing dip down the sedimentary succession.
2. There are distinct variations between the character of the outcropping beds on the eastern profile and the western profile of Roghi Mountain, which in previous work has not been explained.
3. There exists very little age constraining studies that can pinpoint either the age of faulting or deposition of different lithological units.
4. The character of the Roghi Mountain sedimentary outcrops complicates any correlations to be made over a larger area by the use of traditional mapping methods. This is due to the lack of any distinct bed that can be continuously traced, or recognized ,across the half graben infill.
5. The mountainsides of Roghi Mountain are very steep, this limits the accessibility to key outcrops. With limited access to outcrops many observations must be made from a distance, this can lead to severe misinterpretation and confusion as the view perspective can influence the observations severely.

In light of the recognition of these issues, The University of Stavanger and Heidelberg University collected a Light Detection and Ranging (LiDAR) dataset (explained in detail in chapter 1.6.1) of Roghi Mountain in an attempt to obtain a complete 3D image of the geology. This dataset was collected with the anticipation of achieving an improved structural/stratigraphic understanding of this thick sequences of syn-rift sedimentary rocks.

1.2 Project Objectives

The primary project objectives were:

1) Understand the present day structure and stratigraphy of the supposedly syn-rift sediments that make up Roghi Mountain in the Kerpini Fault Block by interpreting the 3D LiDAR dataset, carry out a detailed structural analysis, and identify indicators for facies changes.
2) Propose an evolutionary model of the Roghi Mountain sedimentary succession.

1.3 Tectonic Evolution of the Gulf of Corinth

The pre-rift carbonate basement was deposited as a carbonate platform during the Mesozoic. Paleogene collision and overthrusting emplaced these units from east to west as thrusts sheets striking perpendicular to the younger rift faults (Collier and Jones, 2004). How these thrust sheets has effected fault development related to the Corinth Rift is not fully understood.

The active rifting located in the Gulf of Corinth is argued to be influenced by the complex interaction of three regional geological events or processes (Armijo et al., 1996; Bell et al., 2008).

1. The northward movement of the African plate was significantly reduced at around 30Ma (Taylor et al., 2011). This resulted in increased retreat of the Thetyan slab as well as gravitational collapse of overthickened crust causing back-arc extension across the Aegean Sea (Jolivet et al., 2013).
2. The North Anatolian Fault propagated westward across Turkey and into the Aegean Sea at around 2-3 Ma (Armijo et al., 1996). This caused a re-structuring of the initial rift zones and as well as increased slab roll-back (Armijo et al., 1999; Taylor et al., 2011). The initiation of the main rift in the Gulf of Corinth is estimated to have started in the Pliocene, this is based on a combination of structural and sedimentological studies and micropaleontological dating (Doutsos and Kokkalas, 2001; Ford et al., 2013; Leeder et al., 2008; Rohais et al., 2007; Taylor et al., 2011).
3. Currently the interplay between the Aegean, Central Greece, South Marmara and Anatolia microplates controls the deformation of the Aegean region with the most active areas at the margins of these plates (Taylor et al., 2011).

The active rift in the Gulf of Corinth is located along on the southern margin of the Central Greece microplate (Figure 3). Present day rifting rates across the central part of the Gulf of Corinth has been measured to 16mm yr^{-1} (Avallone et al., 2004).

The central Gulf of Corinth is currently subsiding as opposed to the southern gulf margin which is currently uplifting (Palyvos et al., 2008; Palyvos et al., 2010; Palyvos et al., 2007). Some of the earliest syn-rift sediments and normal faults have been uplifted to the excess of 1000 meters (Flotté et al., 2005; Ford et al., 2013; Sorel, 2000). All of the faults located south of the coastline within the northern Peloponnese peninsula are considered inactive (Figure 1) (Leeder et al., 2008).

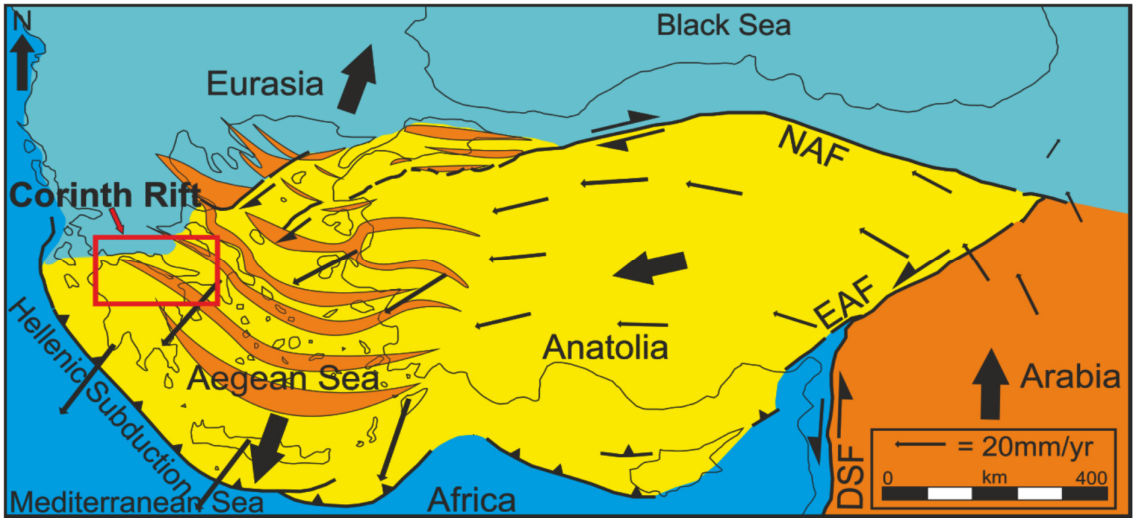

Figure 3 Map of regional faults and plateboundaries related to the Aeagan Sea from Armijo et al. (1996).

1.4 Regional Structural Setting

The high topographic relief observed inland on the northern part of the Peloponnese Peninsula is directly related to the only phase of extensional tectonic activity. From the town of Kalavryta and northwards towards coastline to the Gulf of Corinth there are at least four major fault blocks that range in width from 4 to 7 km (Bell et al., 2009; Ford et al., 2013). The major fault blocks are bounded by normal faults that strike parallel to the rift axis of the Gulf of Corinth rift. Ford et al. (2013) interpreted the trend of the major bounding faults to be between N086° and N112°, the same study includes kinematic data that indicates dip-slip displacement on most of the faults in the region.

In the Kerpini Fault Block, most of the exposed sedimentary layers dip at an angle of around 20-25° southwards towards the Kerpini Fault. These sediments unconformably overlie the pre-rift carbonate basement, and a widespread unconformity contact is visible towards the uplifted northern part of the block, i.e. in the immediate footwall of the Dhoumena Fault. This is typical for half-graben structural settings and similar geometries can be observed in surrounding fault blocks, although the unconformity and fault dips vary from block to block. This sort of setting can conceptually be visualized as a "domino" structural style (Figure 4) where each of the fault blocks has been rotated causing the footwall to be uplifted and the hanging wall to subside. Syn-rift sedimentation fills the accommodation space created when blocks rotate crating a maximum package thickness in the immediate faults hanging wall, and thinning (or being absent/eroded) towards the uplifted footwall. The dip angle of the syn-rift strata is expected to increase down section as is expected for syn-rift packages (Fossen, 2010).

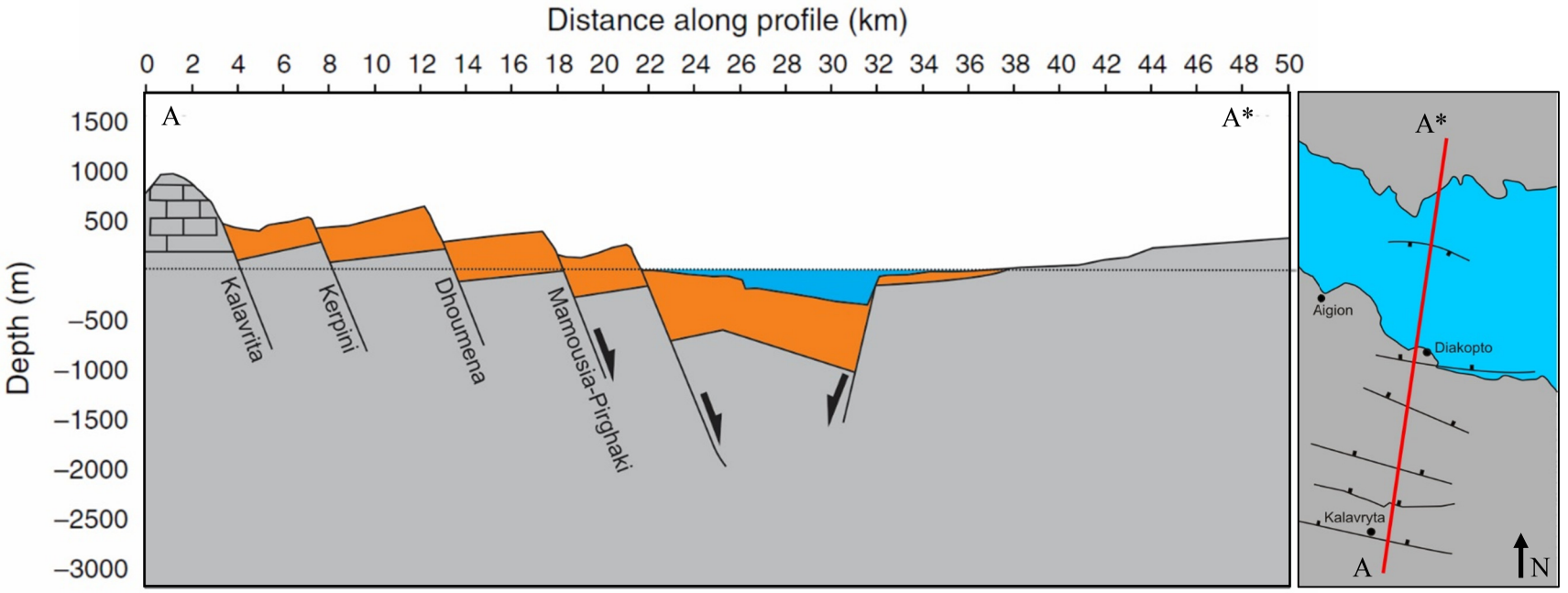

Figure 4 Display of major faults from Kalavryta and across the Gulf of Corinth, basement in grey colour and syn-rift strata marked in orange. Active faults are marked with black arrows indicating direction of displacement. Modified from (Bell et al., 2009)

Several faults are clearly exposed in the terrain from Kalavryta and northwards to the coast, yet there is a ongoing debate in regards to how these faults terminate at depth in the subsurface. Flotté et al. (2005); Jolivet et al. (2010); Sorel (2000) suggested the existence of a deep, low angle (less than 30 degrees) regional detachment fault striking more or less parallel to the Gulf of Corinth (Figure 5). Sorel (2000) named this fault the Northern Peloponnese Major Fault (NPMF) and suggested that it connected with a major fault right off the coastline to the Gulf of Corinth. The NPMF fault is estimated to have a throw of roughly 16 km (Sorel, 2000) and is argued to explain the somewhat anomalous extensional rates that have been modelled for the Corinth Rift. Bell et al. (2008) believed that these rates could be explained by the combined displacement of the offshore and onshore faults, and found no evidence for the existence of NPMF.

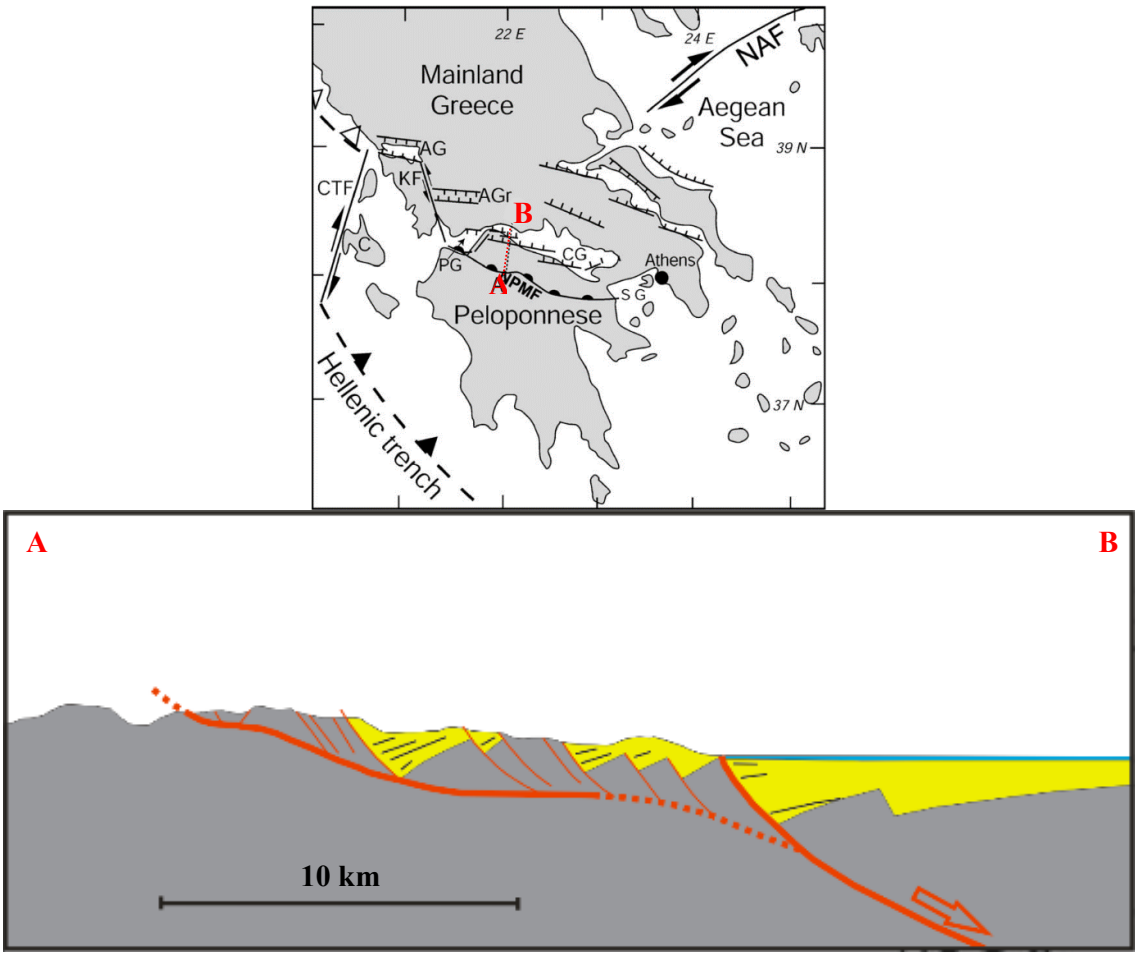

Figure 5 Cross section displaying the deep low angle fault underlying the normal fault blocks dominating the region. This cross section is slightly east of study area. Modified from Flotté et al. (2005).

1.4.1 Fault Network and Geometries

The Kalavryta, Kerpini, Dhoumena and Mamousia-Pirghaki Faults bound the four major fault blocks of the region from south to north, respectively. The Kalavryta Fault is poorly exposed, this creates uncertainties in interpreting the fault geometries. Several steps have been interpreted to occur along the fault (Finnesand, 2013). Ford et al. (2013) estimated fault displacement to roughly 1200 m while Finnesand (2013) estimated displacement of 800-900 m.

The Kerpini Fault has better exposure than the Kalavryta Fault, yet the displacement of the fault has not been concluded in previous work. Collier and Jones (2004) estimated maximum displacement of 2.5 km while Ford et al. (2013) assessed the maximum displacement to 1.5 km. Ford et al. (2013) estimation was further supported by Dahman (2015) and Syahrul (2014).

The Dhoumena Fault is well exposed in the topography, yet large differences occur in the interpretation of displacement along this fault. Ford et al. (2013) estimated the maximum displacement to 800 m, Collier and Jones (2004) suggested 2 km and Dahman (2015) calculated 1200 m. Syahrul (2014) proposed a similar displacement pattern as the Kerpini Fault.

For the Mamousia-Pirghaki Fault minimum displacement was suggested to 1500 m by Ford et al. (2013), this is supported by Dahman (2015).

The termination of these major faults is still under debate, one suggestion is the presence of transverse or transfer faults segmenting the various fault blocks (Dahman, 2015; Mrlina, 2014; Syahrul, 2014). While the interpretations of Ford et al. (2013) do not recognize these north-south structures, with their maps indicating near continuous east-west trending structures.

1.4.1.1 Transverse and Transfer Faults

Faults that strike more or less perpendicular to the majority of faults in an area can often be identified as transverse or transfer faults (Figure 6). These faults often occur as block terminations as described by Morley (1995).

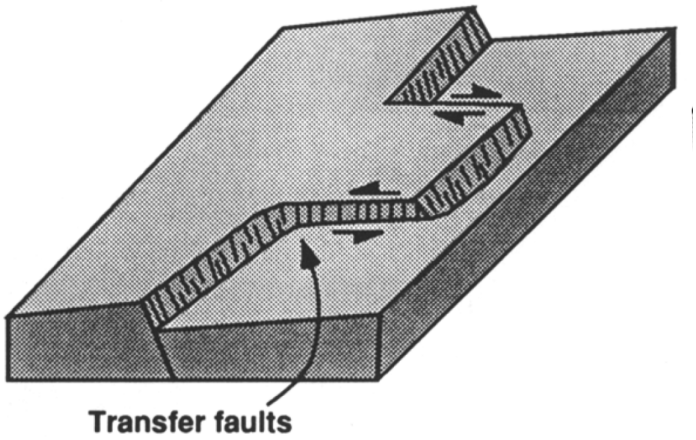

Figure 6 Conceptual diagram of transfer fault. These faults are very high angle faults often occurring at block terminations. From (Morley, 1995)

Geological maps of the Northern Peloponnese show that many faults cannot be traced across the many deep river valleys cross cutting the many fault blocks near the Kerpini Fault Block. In addition, there are often large variations in the thickness of the syn-rift sedimentary units on either side of these valleys. Mrlina (2014) investigated the possibility of the existence of transverse faults to explain these observations. Mrlina (2014) study area was focused on the coastal region of the northern Peloponnese where a gravitational dataset strongly argues for the presence of several transverse faults. However, Mrlina (2014) did not conclude how far south these transverse faults stretch.

Dahman (2015) proposed three transfer faults stretching from the Kalavryta area and northwards towards the coast (Figure 7). These transfer faults were introduced to explain why there are fault steps, sudden fault terminations, thickness variations of the syn-rift sequences as well as lithological variations across the many river valleys of the area.

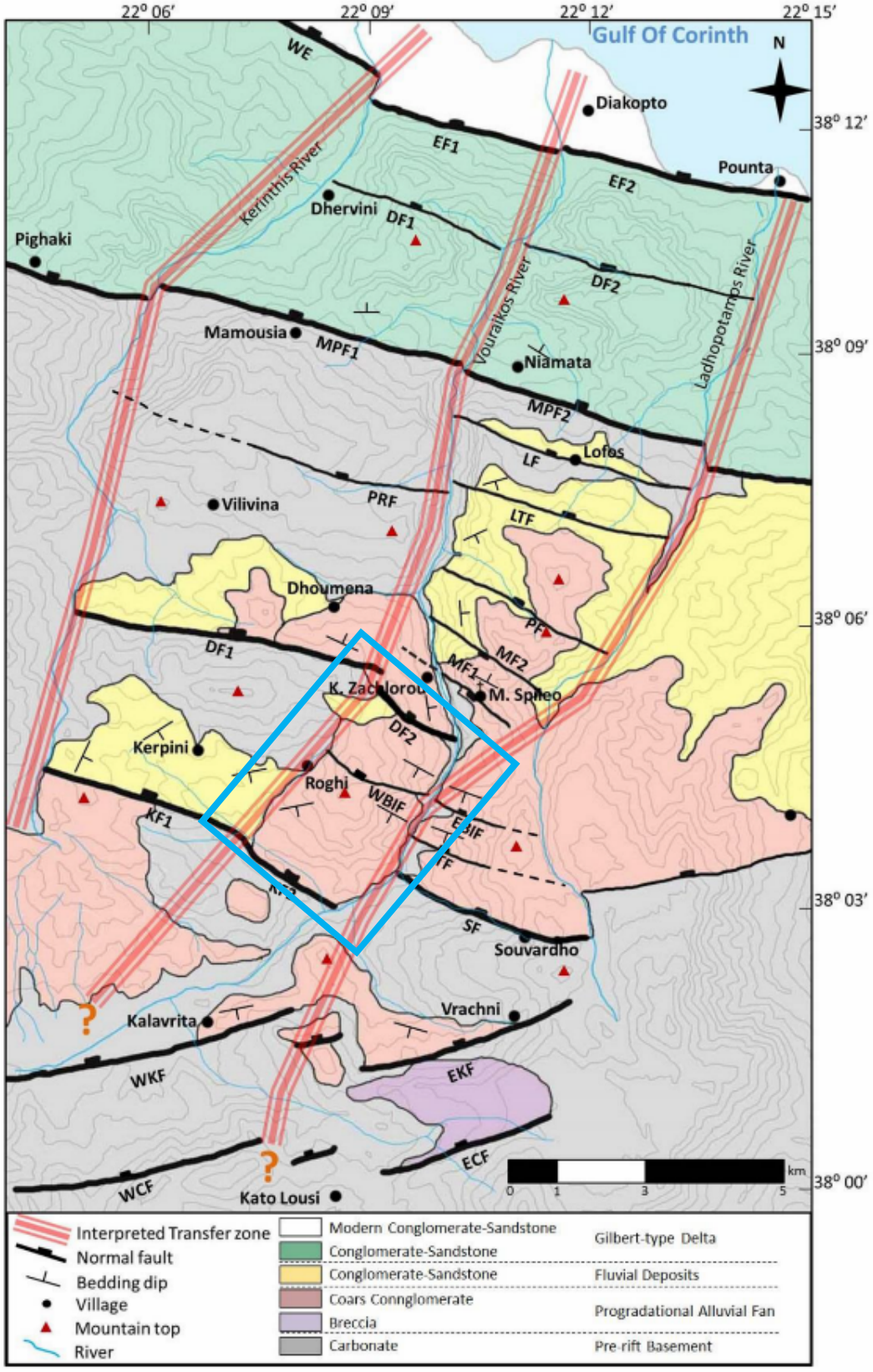

Figure 7 Map showing the north-south transfer faults that roughly follows the deep river valleys cross cutting the major fault blocks from Kalavryta and northwards towards the coast. Study area located within blue rectangle. Modified from Dahman (2015).

1.5 Previous Work Related to Study Area

Studies of the Kerpini Fault and block has mostly appeared in research with a more regional focus. Collier and Jones (2003); Ford et al. (2013) made geological maps (Figure 8) and cross sections to explain the structure and evolution of the fault blocks related to the central Corinth Rift system. Recent magnetostratigraphy studies (Hemelsdaël et al., 2015) made in the different fault blocks related to the study area has provided some age constraint for the depositional age of the sediments found there. Offshore studies of the Gulf of Corinth can be related to onshore areas like the Kalavryta, Kerpini and Dhoumena fault blocks. These studies are often focused on fault architectures, basin structure and how the Corinth rift evolved (Bell et al., 2008; Bell et al., 2009; Ghisetti and Vezzani, 2005; Hemelsdaël and Ford, 2014; Moretti et al., 2003; Ori, 1989; Skourtsos and Kranis, 2009; Taylor et al., 2011).

Over the last three years, a series of UiS supervised MSc theses have been written in the area from the town of Kalavryta and northwards to the coastline of the Gulf of Corinth. Finnesand (2013) interpretations suggested that the Chelmos and Kalavryta faults have a more complex structure and geometry than previously mapped with multiple steps in the fault displacement. Syahrul (2014) studied the relationships between different sedimentary units within the Kerpini Fault Block and proposed a sedimentary infill chronology for the Kerpini Fault Block. A detailed study of the complex fault networks observed on either side of the Vouraikos valley was carried out by Dahman (2015) who also studied fault relations with sedimentary infill. Rognmo (2015) suggested, after lithological study of sediments in the Kalavryta and Kerpini fault blocks, that there existed a single alluvial fan that spread across the these two fault blocks prior to the displacement of the Kerpini Fault was initiated.

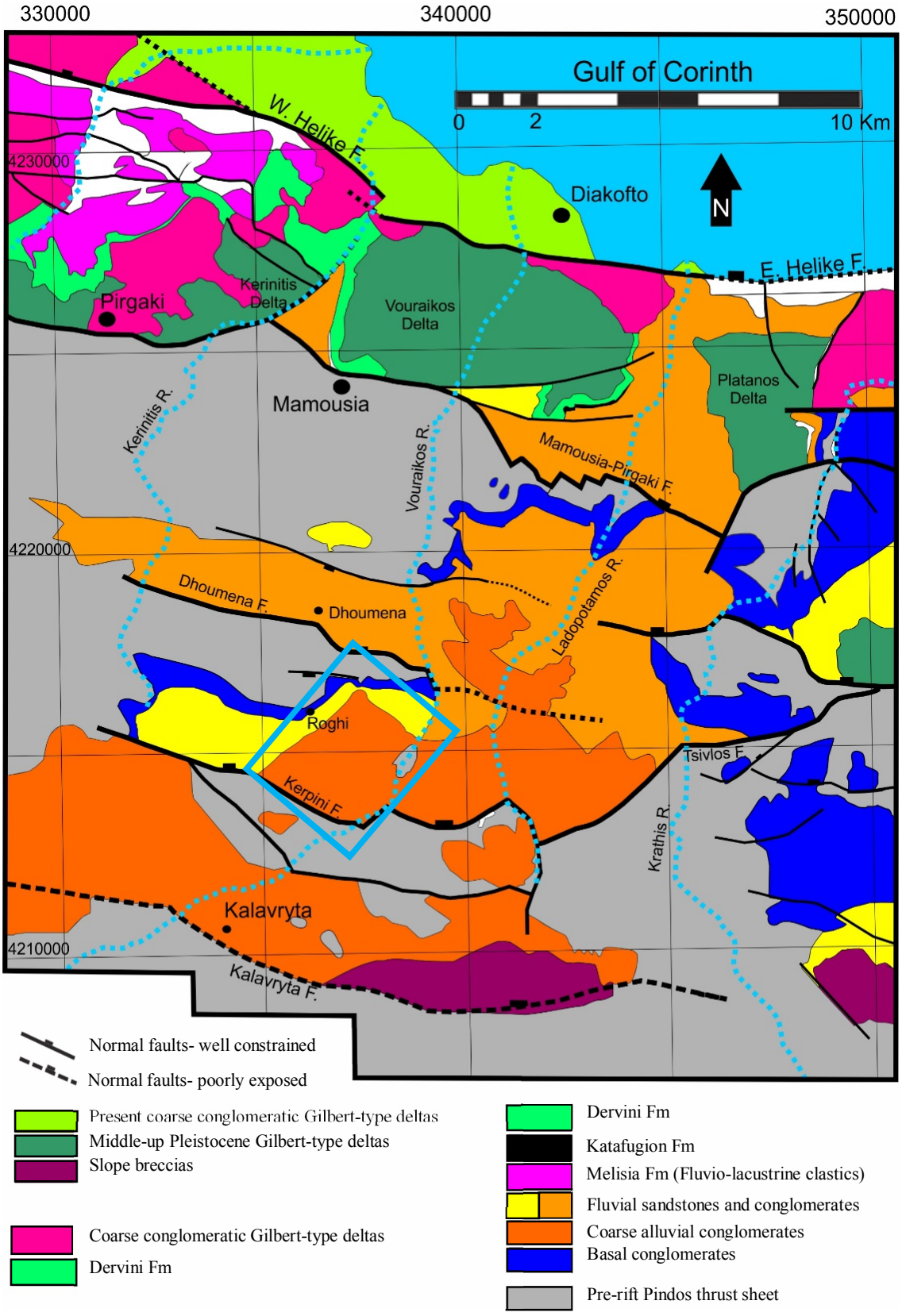

Figure 8 Lithological map modified from Ford et al. (2013) Blue rectangle indicating study area for this project.

1.5.1 Proposed Evolutionary Models Of The Kerpini Fault Block

The interpretation of the different depositional patterns observed in the syn-rift strata of the Kerpini Fault Block and in adjacent areas are still under debate. This debate is also closely related to the interpretation of the chronological development of the faults in the region as very little age constraining studies have been conducted in the area.

Gawthorpe and Leeder (2000) presented the classical model for normal fault system evolution that suggests that the syn-rift sedimentary infill is directly related to the growth of the fault system. In other words, the syn-rift sediments are sourced from the erosion occurring as the footwall of the normal fault is uplifted (Gawthorpe and Leeder, 2000). Ford et al. (2013) argued that this model is conditioned on the assumption that the pre-rift topography is relatively flat, and therefore does not apply for the Corinth Rift that formed on top of a series of thrust sheets related to the Hellenide Orogeny. It is further argued by Ford et al. (2013) that syn-rift deposition is controlled both by a growing normal fault system alongside the pre-existing topography. The pre-rift river drainage system is then thought to have been "inherited" into the extensional rift phase of the Corinth Rift, as described by Jackson et al. (2006) in the similar setting of the Suez Rift in Egypt.

Hemelsdaël et al. (2015) conducted a magnetostratigraphic correlation across multiple fault blocks, including the Kalavryta, Kerpini and Dhoumena Fault Block. These manetostratigraphic measurements were then used as the basis for a chronostratigraphic model indicating that the Dhoumena Fault Block formed roughly 1 Ma earlier than the Kerpini and Kalavryta Fault Blocks. Previous work done by Collier and Jones (2004) argued that the Kalavryta, Kerpini and Dhoumena Faults were active roughly at the same time, and that major fault propagation occurred in the northward direction. This evolution is illustrated by Bell et al. (2008) in Figure 10.

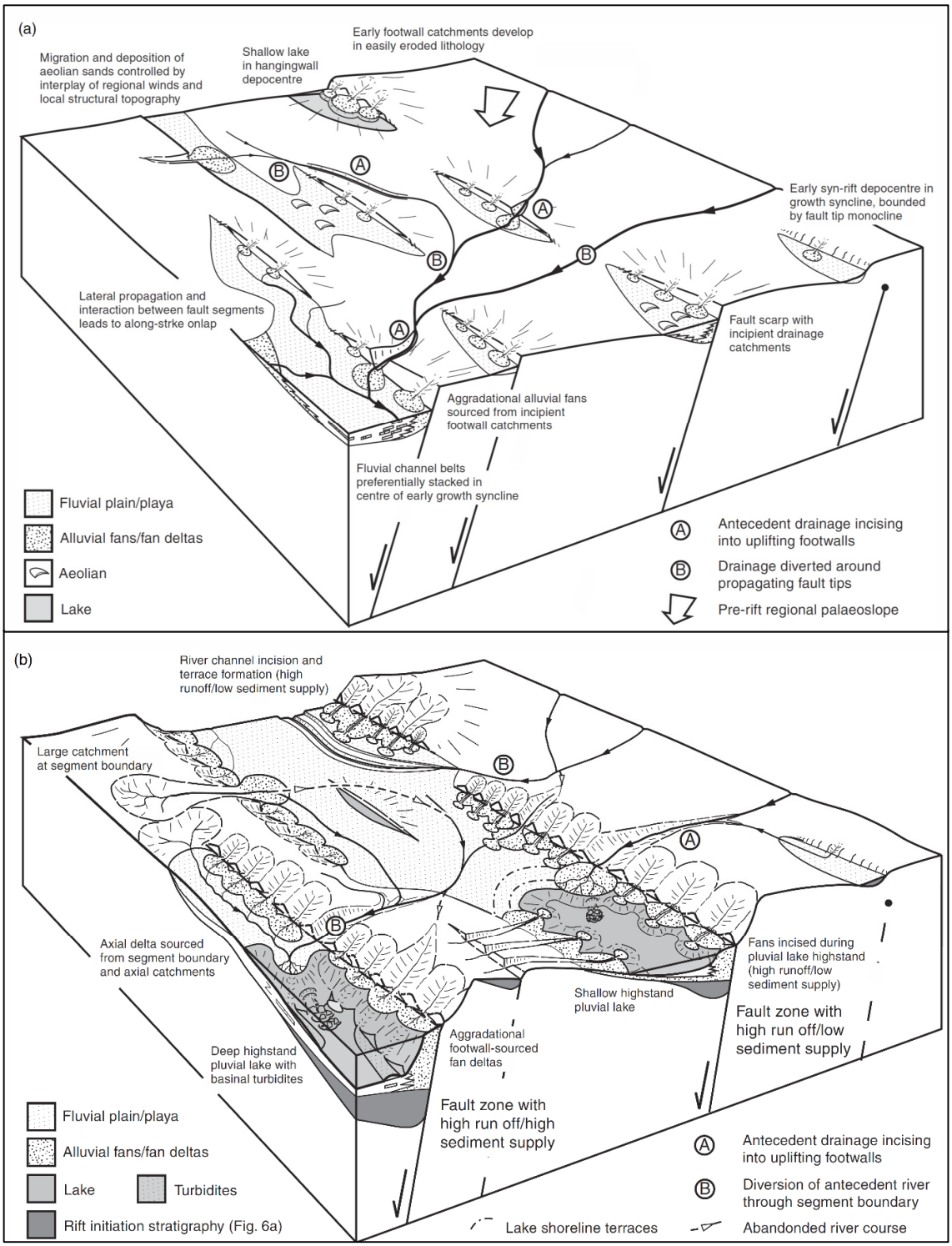

Figure 9 Model of syn-rift sedimentary infill with fault growth in an extensional tectonic setting dominated by normal faults. From Gawthorpe and Leeder (2000).

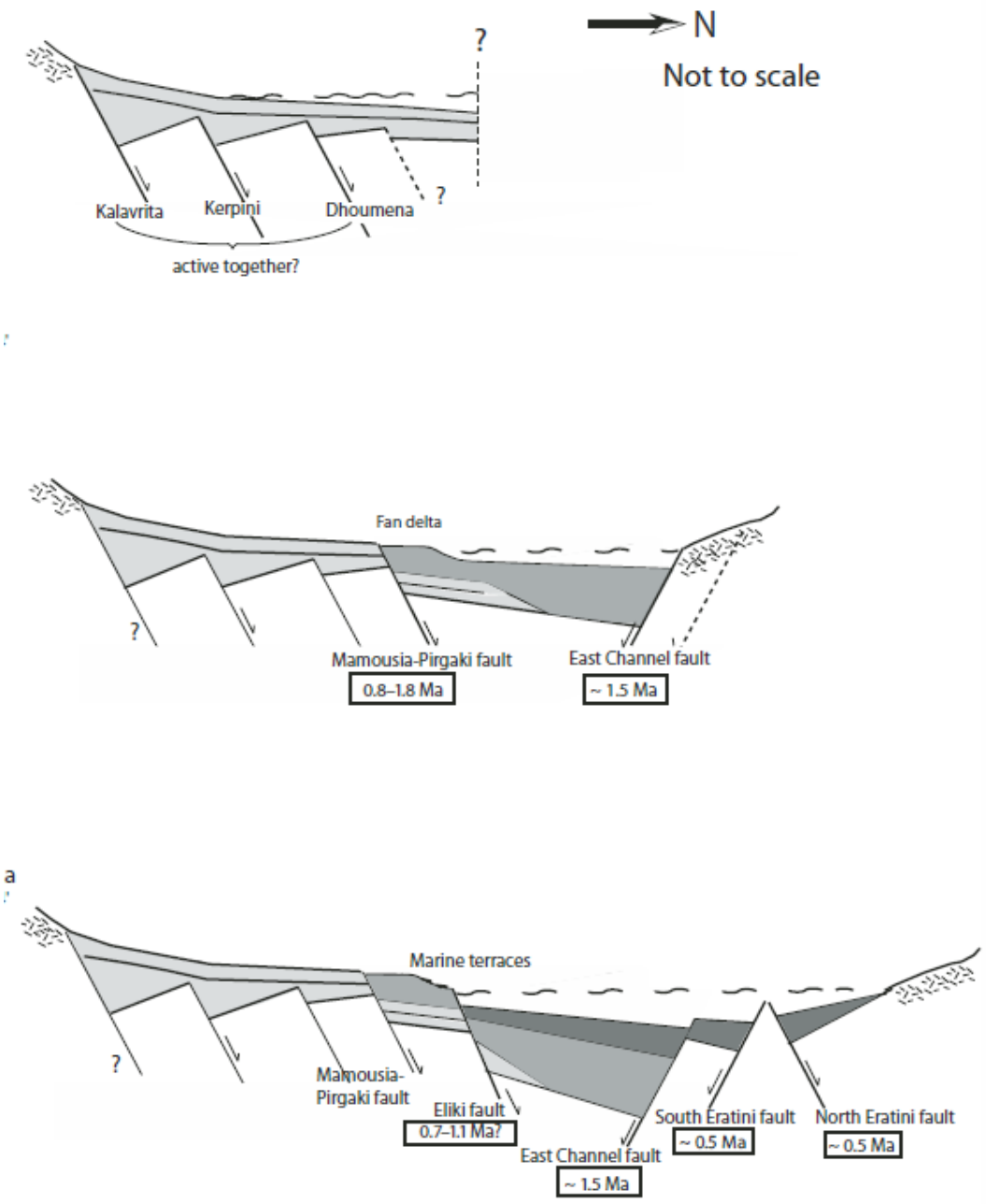

Figure 10 Illustration of the chronology of fault growth/activation A) represents initial phase, B) intermediate and C) the present day structural setting. From Bell et al. (2008).

1.6 Dataset

The dataset for this thesis can be divided in two classes, field data collected fieldwork in the study area and LiDAR data collected prior to the initiation of this thesis project.

1.6.1 LiDAR Data

LiDAR scanners emit a powerful light pulse, which travels through the air, hits an object, and is reflected back to the scanner. The LiDAR scanner can then calculate the range from the scanner to this object based on the light pulse travel time (Laux and Henk, 2015). By using this technique, the LiDAR scanner can scan a large area and combine each measurement of the scan into a point cloud where each measurement is represented as a point in 3D space. Connected to the LiDAR scanner is an accurate GPS station, this allows the point cloud to be geometrically referenced in any coordinate system. Multiple scans from different locations can be combined together to provide coverage from all angles of the desired object. Attached to the LiDAR scanner is a specially calibrated camera which takes photographs of the same areas as the LiDAR scanner has scanned. These photographs can then be used to colour each point in the point cloud. By using LiDAR scanners it is possible to generate detailed 3D scans of any object, building or outcrop with resolution down to millimetre scale between each point in the point cloud.

The LiDAR data is the most important part of the dataset for this thesis and represents the skeleton of which the structural model of Roghi Mountain is based on. The LiDAR dataset used in this theses was collect by the Heidelberg University (of Germany) in April 2015. The dataset covers an area of roughly 11 square kilometers (Figure 11). However, this dataset does not cover the entire area of Roghi Mountain. Therefore, another dataset was collected by the UiS to infill the missing area and to improve coverage of a an area of the Heidelberg dataset which had very limited resolution (Figure 11). But due to inexperience in acquisition of this second dataset was unusable. The point cloud consist of over 270 million individual points. The resolution of the dataset depends on the point spacing, on average the points are 10 cm apart which is a high resolution for the purposes of this project. However, there are a few locations where the scanners could not get a clear line of sight, this has created some patches where areas of roughly 2 to 5 m^2 are without any points. All geo referencing, multiple station alignment (aligning/combining scans from different scan positions) and point cloud colouring (the process of colour coding the individual points) was undertaken by the Heidelberg University. The Heidelberg University dataset covers the whole of Roghi Mountain, except a

small area in the north close to the contact between syn-rift sediments and basement (Figure 11).

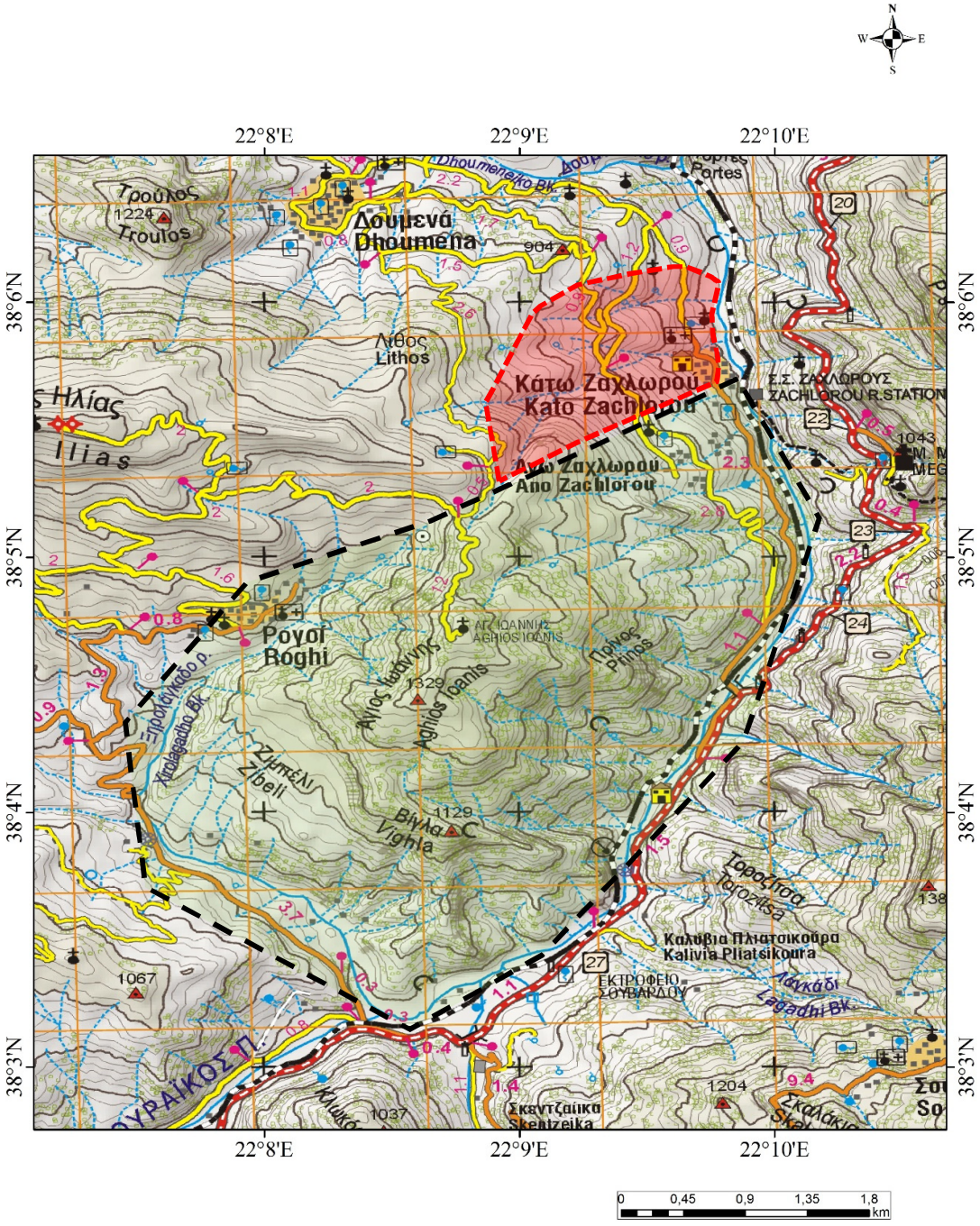

Figure 11 Map over study area, LiDAR data coverage indicated by black dashed polygon. Area of Roghi Mountain not covered by LiDAR data indicated with red dashed polygon. The area of the red dashed polygon was the focus area of the failed UiS dataset.

Although the LiDAR dataset gave a "complete" 3D picture of the geometry of Roghi Mountain it could not always replace the experience of viewing the geological features in person. Geological features could be observed under different light conditions and from different view points to obtain a more complete opinion prior to making an interpretation.

1.6.2 Field Data

All field data was collected during a three-week field trip in August of 2015. Fieldwork was focused on creating geological maps, outcrop descriptions and collecting dip and dip direction measurements. In addition, approximately 5500 photographs were taken to be used for reference. A GPS device was used to record the location of geological contacts, field measurements and photo locations. The purpose of collecting field data was to compliment the LiDAR dataset such that some "hard" data points could be used for reference. For example, the resolution of the LiDAR dataset was not high enough to identify the lithology, grain size and sorting in the outcrops, therefore the field data could be used together with the dataset in the interpretation of the LiDAR data.

Chapter 2: Methodology

The workflow for this project can be divided in three main parts; pre-fieldwork, fieldwork and post-fieldwork.

2.1 Pre-Fieldwork

The pre-fieldwork was focused on reviewing existing work of the area and surrounding areas, preparing maps to be used for geological mapping and produce some initial interpretations of the study area based on photographs and previous work. Several locations in the study area were designated for viewpoints, possible geological contacts and investigation of specific outcrops.

2.2 Fieldwork

The focus of the fieldwork was to make geological maps and outcrop descriptions as well as collect photographs for reference to use alongside the LiDAR data. Mapping and description efforts were aimed at searching for evidence for faulting, layer continuity, unconformities and lithological variations. Dip-measurements where collected at different locations in the study area. Many different viewpoints in the study area were also visited to get different perspectives of the structures of Roghi Mountain.

2.3 Post-Fieldwork

The post-fieldwork was focused on five main points:

1) Processing of UiS LiDAR data.
2) Preparation of LiDAR data for interpretation by;
    i) Identifying a software to use for interpretation and modelling.
    ii) Import LiDAR data to Petrel E&P.
    iii) Develop a workflow for interpreting LiDAR data in Petrel E&P.
3) Integration of field data with LiDAR data in Petrel E&P.
4) Structural analysis of LiDAR data.
5) 3D Structural modelling.

2.3.1 Processing of LiDAR data

To get the raw LiDAR data in the format which was desired for this project, a number of processing steps were required. The LiDAR dataset supplied by the Heidelberg University was already processed, however at the same time as the fieldwork for this thesis was carried out

UiS personnel collected another LiDAR dataset to compliment the Heidelberg University dataset. The UiS dataset was composed of raw data only, with no post-field processing.

To utilize the dataset collected by UiS a number of processing steps were applied with the use of RiScanPro (computer software from RIEGL Laser Measurement Systems). The dataset consisted of three separate scanning positions, the individual scans had to be geo-referenced and then aligned. Aligning the three scanning positions was carried out in two main steps. Firstly, the GPS location of the scanner positions aligns the pointclouds to a certain extent with a error in overlap between the different scans by some tens of meters. Then a second alignment was then done by identifying "anchor points" in the overlap zones between the different scans, this process generates a very good alignment with an error below 1 mm of mismatch between the different scans.

After aligning the three scan positions Red-Green-Blue (RGB) colour coding could be assigned to the point cloud. When the LiDAR scanner was used in the field a specially calibrated camera was mounted on top of the scanner which took pictures of the exact same areas as the scanner. These pictures could then be used to assign colour to the point cloud. However, there were significant issues with the quality of the photographic images related to the three scans. The poor quality of the images were caused by a combination of foggy weather conditions and the camera was inaccurately adjusted. These two factors caused the images to be overexposed and appear extremely bright, the LiDAR software does not allow for any colour adjustment of the photographs to correct this effect. This left the UiS LiDAR dataset unusable, as the quality of photographs was too poor.

2.3.2 Preparation of LiDAR data for interpretation

The process of preparing the LiDAR data for interpretation and further analysis can be divided in three parts:

i) Identifying a software to use for interpretation and modelling.
ii) Import LiDAR data to Petrel E&P.
iii) Develop a workflow for interpreting LiDAR data in Petrel E&P.

2.3.2.1 Identifying a software to use for interpretation and modelling.

One of the objectives of this project was to create a structural model of Roghi Mountain, one issue was then to determine which software would be suitable for interpretation and for the modelling process. Heidelberg University advised the use of CloudCompare (open-source software) for visualization of the LiDAR data, however no interpretation could be done on this

software. The standard LiDAR data processing software RIGEL is not suited for any advanced interpretation or geological mapping, and certainly not for structural modelling. Petrel E&P was chosen for interpretation and modelling as this software is frequently used at UiS for geological interpretation and reservoir modelling and is very versatile, however this software has never been used with LiDAR data before at UiS.

2.3.2.2 Import LiDAR data to Petrel E&P.

The standard version of Petrel E&P (2014 version) could not visualize the LiDAR data as CloudCompare and the RiScanPro software for two reasons;

1) Petrel E&P 2014 needed to convert the LiDAR data points to its own program specific point data. Petrel E&P is not capable of displaying very large point-sets (in this case over 270 million points). However, the point data could be downscaled, i.e. decreasing the point spacing to for example 1 m spacing. This drastically reduced the number of points in the dataset, but also decreased the resolution of the dataset.
2) Once the low resolution point set could be displayed in Petrel E&P it was evident that the program specific points of Petrel E&P could not visualize the RGB data stored in the LiDAR data similar to that of CloudCompare or the RiScanPro software.

Therefore, an attempt was made to find a plugin (add on software) to Petrel E&P that could be used to import the LiDAR data in a format that allowed proper visualization. The plugin PointCloudViz by Mirage Technologies was identified as a program that could resolve this issue, UiS was then persuaded to invest in an educational license of the PointCloudViz plugin.

The PointCloudViz software could import the LiDAR data into Petrel E&P by generating a "multi-layer pyramid" of the LiDAR data. In practical terms, this means that only areas of the dataset that is zoomed in on will be displayed in full resolution. This drastically decreases the amount of computer power required for data visualization.

However, there still was an issue in importing the LiDAR data, this was caused by a mismatch between de coordinate reference system of the LiDAR data and the coordinate reference system defined in the Petrel E&P project. This mismatch generated an error when creating the "multi-layer pyramid" of the LiDAR dataset. After consulting with the Mirage Technologies help center, a workaround was presented where a third-party software was used to create the "multi-layer pyramid" manually.

The “multi-layer pyramid” was created using LasTools. The user defines a series of tiles from the LiDAR point data. The dimensions of these tiles decides how many points (of the LiDAR data) would be contained in each tile. In Petrel E&P the number of tiles that should be kept in the cache memory of the computer also needs to be defined. These two settings vastly effected the computer performance during visualization, therefore multiple trails with different settings were carried out to optimize visualization of the dataset. When importing the tiled data with the PointCloudViz software a “multi-layer pyramid” was then generated from the tiled data. In addition, several versions of the LiDAR point cloud were generated with different resolutions by downscaling the dataset by the use of CloudCompare. Low-resolution point clouds could then be quickly visualized, and if detailed views were required the higher resolution point cloud could be used. This workflow then allowed for a proper visualization of the LiDAR data in Petrel E&P. However, a high performance computer was necessary to be able to display and to work efficiently with such a dataset.

2.3.2.3 Develop a workflow for interpreting LiDAR data in Petrel E&P.

No established workflow was available for how to interpret LiDAR data in Petrel E&P as this software is based on using seismic and well data as the main data when carrying out interpretations and modelling. The classic toolbox used for seismic interpretation (for seismic reflectors and faults) could not be used for on the LiDAR point cloud, so a different set of tools had to be applied. The interpretive workflow utilized two main features of Petrel E&P;

1) Points were used to trace top and base of layers, lithological contacts, fault traces and unconformities.
2) Surfaces were generated either from the interpreted points (described in chapter 2.3.4), or they were generated by best fit as planar surfaces defining the dip and dip azimuth of the plane.

2.3.3 Integration of Field Data with Lidar Data in Petrel E&P

The GPS registered field data were imported into the Petrel E&P project and incorporated with the LiDAR data. These GPS points were then visible in the Petrel E&P project as markers displaying lithological contacts, faults, unconformities and dip/dip direction measurements.

2.3.4 Structural Interpretation of LiDAR Data.

Much like the workflow of interpreting seismic reflectors, individual layers were traced directly on the LiDAR point cloud by digitizing points along the top and base of outcropping layers. Surfaces could then be generated by using the digitized points as input, or by generating a plane

and adjusting the dip and dip direction manually until it intersected the digitized points of the traced layer with a minimum misfit (Figure 13).

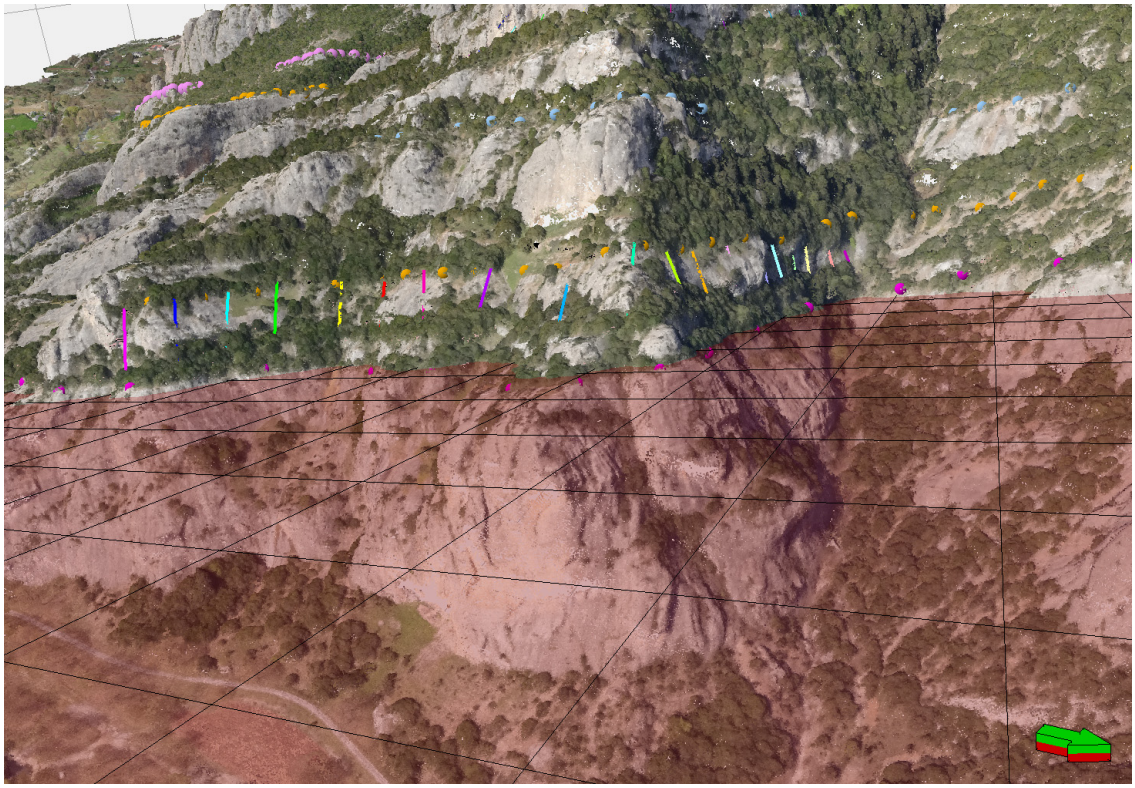

Figure 12 Display of layer tracing on the LiDAR data, a series of points are picked along the layer (pink points), then a surfaces is attempted to be fitted through all of the points (red surface with black grid).

2.3.5 Structural Analysis of LiDAR data

Besides the direct interpretation done on the LiDAR dataset (tracing layers, faults and unconformities), two analytical workflows were generated for the LiDAR dataset.

2.3.5.1 Dip and Dip Direction Analysis

Surfaces were generated for most of the traced layers. The dip and dip direction for each of the generated surfaces were recorded and plotted as planes in stereonet plots. These stereonet plots were then used to compare and correlate layers at different parts of the outcrops.

2.3.5.2 Thickness Analysis

Thickness variations on individual layers were also carried out on the LiDAR data. The aim of this thickness analysis was to identify trends in the thinning and thickening of layers in specific directions (east-west, south-north). This was done by tracing point-pairs, one point at the top of the layer and one at the base. The elevation difference between these two points was treated

as the true vertical thickness (TVT) of the layer (Figure 13). These point-pairs were then loaded into Microsoft Excel where the TVT was converted to true stratigraphic thickness (TST) using the dip of the each layer.

With this workflow, the positioning of the point-pairs when measuring has potentially significant effect on the layer thickness value. The most reliable measurements were taken directly towards the strike of the layer (which would give the TVT). However, this was not a trivial task, which lead to uncertainty in the measured thickness values. The output of the thickness variation plots can therefore only indicate significant trends in the thickness variation of the traced layer.

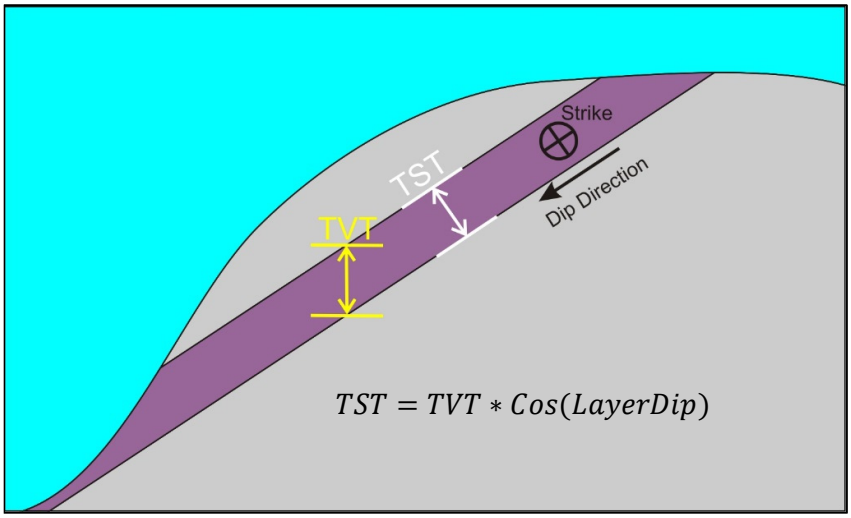

Figure 13 Illustration of a sedimentary layer in an outcrop. White arrow representing the true stratigraphic thickness of the layer, yellow arrow indicating the true vertical thickness of the layer which was measured on the LiDAR data.

Plots were generated in Microsoft Excel between thickness and the position of the point-pair in the east-west and north-south directions. These plots were then used as a tool for identifying trends in the changing thickness of layers in specific directions. Figure 14 shows an example plot. However, thickness analysis was only applied to beds that had a significant exposure in the outcrops in both the south to north, and east to west directions.

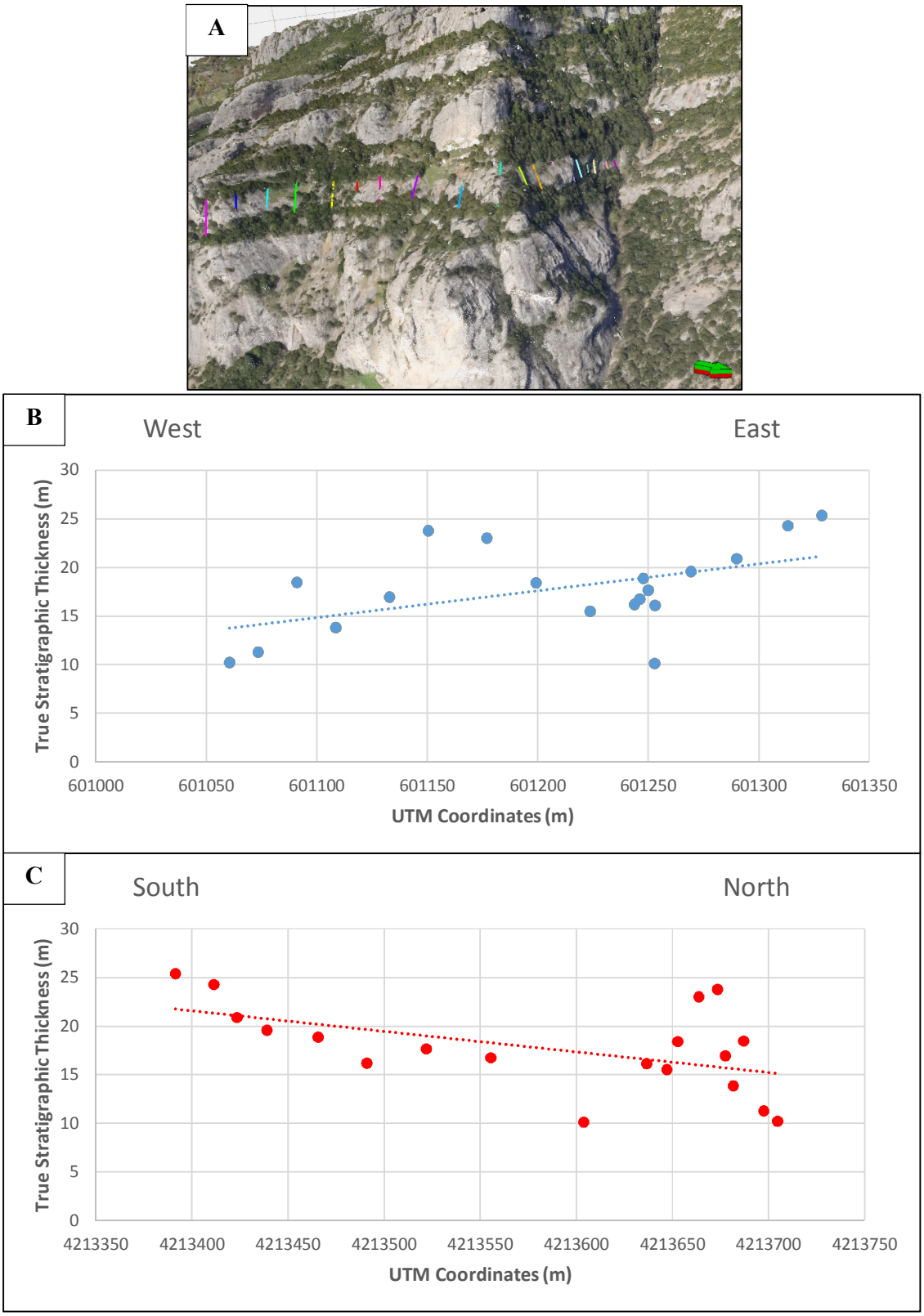

Figure 14 A) Coloured lines represent point-pair measurements made directly on the LiDAR data. B) and C) are graphical representations of the thickness variations calculated from the point-pair measurements. B) represents the thickness variations in the west to east direction, while C) represents the thickness variations in the south to north direction. The dashed line are the trend line for the points.

2.3.6 3D Structural Modelling

For the structural modelling a standard model building workflow for Petrel E&P was utilized. The generated surfaces representing unconformities, faults and layers made up the model input data. Prior to model generation layer relationships were determined, this is related to the relative depositional age of correlated units to determine truncation rules.

A resolution of 10X10 grid cells were used in model construction. In practical terms, this means that the model is visualized by blocks with an average size of $10m * 10m$ (height of blocks vary). This is the same technique used to build the structural framework for reservoir simulation models. By utilizing this workflow, a complete 3D model of study area was generated and the internal structure of the Roghi Mountain sediments could be visualized. Colour coding could then be applied to differentiate individual layers or correlated units.

Chapter 3: Geology of the Kerpini Fault Block and Surrounding Areas

The Kerpini and Dhoumena Faults bound the half-graben infill that makes up Roghi Mountain. The sedimentary infill of the Kerpini Fault Block can be divided into three distinct units, which are referred to here as Group 1,2 and 3 as well as one addition in Figure 16.Group 1 and 3 make up most of the visible outcrops of Roghi Mountain and represents the main focus of this project. Group 2 and the Kalavryta Fault Block sediments (Kalavryta Group in Figure 16) are quite similar lithologically (Ford et al., 2013), however these have been separated in two different groups since they are located in two different fault blocks.

The green sediments marked as Undifferentiated Group in Figure 16 have not been studied in detail in this study. These could be a defined as a part of the Kerpini Fault Block, yet the basement exposures between the eastern side and western of the Vourikos River indicates the presence of a fault in the Vourikos Valley (Dahman, 2015). The lithological character of the sedimentary outcrops across the Vourikos has been interpreted to be the same as the Roghi Mountain sediments by Collier and Jones (2004); Dahman (2015); Ford et al. (2013). For the objectives of this project these sedimentary outcrops have been separated from the Roghi Mountain sediments.

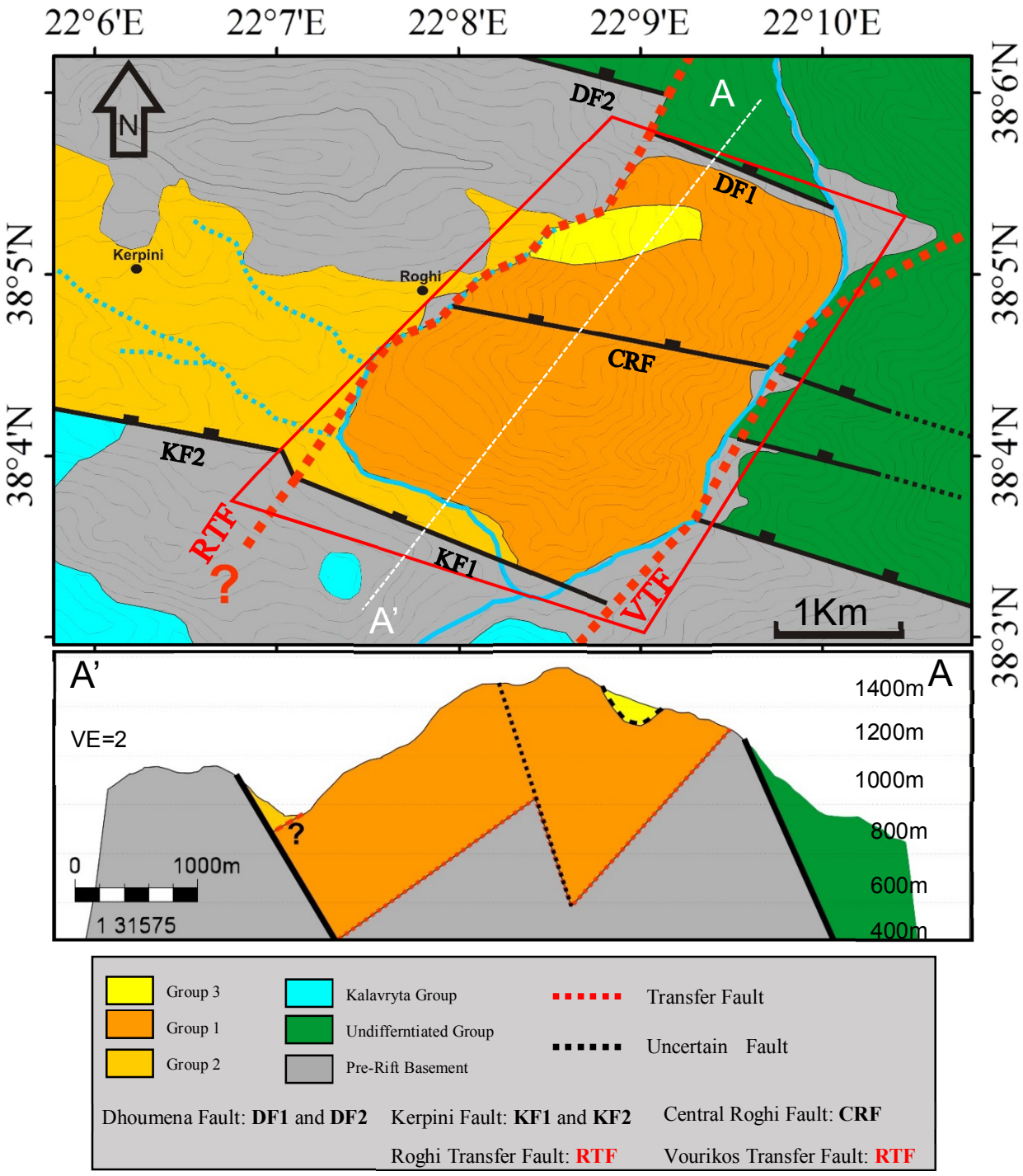

Figure 16 Lithological map of study area (red box) with cross section from A to A'. Dashed white line represents cross section location from A to A'. Red dashed lines in cross section represents unconformities.

3.1.1 Surrounding Units of the Kerpini Fault Block

Several stratigraphic units can be identified in and around the Kerpini Fault Block. The units surrounding the Kerpini Fault Block can be summarized as the Kalavryta Group and an Undifferentiated Group. Both within and surrounding the Kerpini Fault Block the pre-rift carbonate basement outcrops.

3.1.1.1 Basement

3.1.1.2 The exposed pre-rift strata (Figure 16 and Figure 17) in the study area consists of Upper Triassic-Jurassic pelagic carbonates which form part of the Pindos thrust sheets (Skourlis and Doutsos, 2003). The Pindos nappe is a part of the Hellenide thrust sheets that were stacking westward from Cretaceous to Miocene times (Ford et al., 2013; Taylor et al., 2011). Because of this collisional regime, the pre-rift strata his highly folded, faulted, fractured and generally deformed within the study area.

Figure 17 Outcrop phot of pre-rift strata composed of carbonates of the Pindos Nappe

3.1.1.3 Kalavryta Group

Described as coarse grained conglomerates by Stuveland (2015), with less influence of finer grained layers such as sandstone and shale, this group is quite similar to conglomeratic units of the Kerpini Fault Block (Group 1 and 2). Roughly 150 meters of this sedimentary group is

exposed in the footwall of the Kerpini Fault overlying the pre-rift basement (Hadland et al., 2016).

3.1.1.4 Undifferentiated Group

Marked as Undifferentiated Group in Figure 16, this unit consist of conglomeratic/fluvial sedimentary layers. North of the Dhoumena Fault, these units are a part of the half-graben infill of the Dhoumena Fault Block where finer grained sedimentary rocks have been found (Kolbeinsen, 2013). The fault block relationship on the eastern side of the Vourikos river is bit more complicated, as the outcropping units here could be a part of the Kerpini Fault Block, or they could be located in another fault block according to the interpretations of Dahman (2015).

3.1.2 Intra Keripini Fault Block Units

Within the Kerpini Fault Block itself, and besides the basement, three distinct units can be defined.

Group 1: consists of a thick sequence of south dipping conglomerate beds which make up the main part of Roghi Mountain.

Group 2: is made up of the alluvial fan deposits west of Roghi village. This group has been deposited as a series of fans (Hadland et al., 2016; Syahrul, 2014). The relative ages between Group 1 and Group 2 is difficult to determine.

Group 3: is comprised of layered conglomerates and sandstones with a shallow eastward dip. This group outcrops on the northern side of Roghi Mountain and appears to unconformably overlie Group 1. They are distinguished as a separate group due to the low dip angle and deviant dip direction compared to Group 1 (Stuveland, 2015; Syahrul, 2014).

3.1.2.1 Group 1

Composed of alluvial conglomeratic sediments with grain and clast sizes varying greatly from sandstone to boulders when looking at different areas of the mountain. In addition, the clast and grain sizes vary laterally and vertically within discrete beds, as well as between layers. Individual layer thicknesses vary greatly as there are thin centimeter scale shale layers (in one distinct part of the outcrop) to over 50 m thick, massive conglomerates.

Group 1 consists of the most massive conglomerate outcrops of the Kerpini Fault Block, individual layers can exceed 50 meters in thickness with boulder size clasts. These clast consist

mostly of limestone and are light grey in colour (Figure 18). Sandstones can also be found in within this group, often as channel features and not as continuous as the more massive conglomeratic units. Sandstone units and channels are coarse grained and usually have a darker brown colour compared to the conglomerate units. Shale layers are also visible in some distinct areas of Roghi Mountain, these are dark brown to reddish in colour.

Figure 18 Typical outcrop of massive conglomeratic beds defined as group 1.

3.1.2.2 Group 2

Sedimentary outcrops marked as Group 2 in Figure 16 have not been studied in detail for this study but consist mostly of conglomerates and sandstones (Hadland et al., 2016; Stuveland, 2015; Syahrul, 2014). Syahrul (2014) described this unit to have channelized sandstone units within more massive conglomeratic units. In addition, Syahrul (2014) suggested an average layer dip direction of 165° and dip angle of 20°. A more recent study by Stuveland (2015) indicated an average dip direction of 170-180° and a dip angle of 21°. Stuveland (2015) also mapped out several sub-horizontal units within what has been defined as Group 2. The previous work of Stuveland (2015) indicates that there is a complex relationship of many different units within Group 2, and the nature of the outcrops within Group 2 makes reliable measurements and correlations challenging.

3.1.2.3 Group 3

Group 3 (Figure 19) has much thinner layers compared to Group 1 with no individual layer exceeding 10 meters in thickness. Layers are still conglomeratic but much finer clast compared to Group 1. Sandstone layers are more continuous, and the general colour is much more brown compared to the grey colour observable in most of the massive layers of Group 1.

Figure 19 Outcrop of sedimentary rocks defined as Group 1 here interchanging layers of sandstone and conglomerate are visible.

3.1.3 Alluvial Fan Deposits

The conglomeratic units found within the study area of the Kerpini Fault Block are deposited by alluvial fan complexes (Ford et al., 2013). An alluvial fan is a conical, lobate or arcuate build up of sediments that has a focused source of sediment supply, for example from a canyon or channel from a mountain front (Galloway and Hobday, 1996). The coarsest grained alluvial fan systems are most often related to debris-flow fans in areas with a steep topographic gradient. These fans can cover areas up to $100km^2$ and are often characterized by poorly stratified matrix- to clast-supported conglomerates and breccias (Galloway and Hobday, 1996).

Chapter 4: Observations

This chapter is aimed at dividing Roghi Mountain into distinct units which may be separate geological entities, i.e. to break down the geology into its smallest units. Each unit and its boundaries will be described in detail.

Chapter 5 will discuss the interpretation of the different units and how the various segments correlate. Where there is poor evidence for correlation, different structural/stratigraphic options will be presented. This approach is especially important to try and explain the differences between the eastern and western Roghi Mountain profiles.

4.1 Segments

To discuss the various features observable in Roghi Mountain in relation to the objectives of this project eight different segments have been defined (Figure 20). The boundaries between these different segments are not necessarily related to any geological contact, i.e. these segments have primarily been defined for descriptive purposes. In Chapter 5 the relationship between these different segments, and especially the layers within the different segments will be discussed in detail.

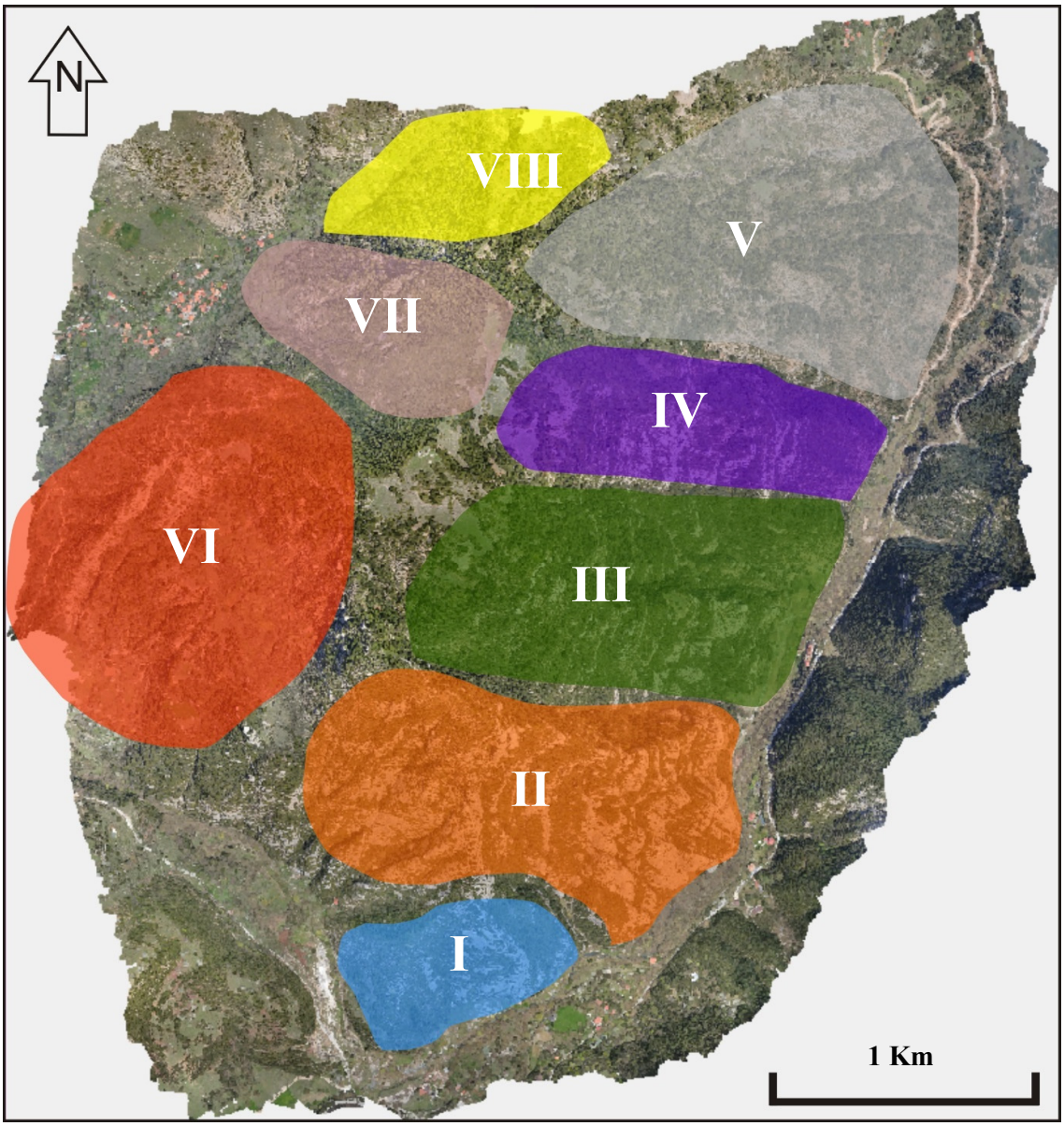

Figure 20 Defined segments of Roghi Mountain marked in a map view of the LiDAR data.

4.2 Eastern Profile

The eastern side stretches across roughly three km in the north-south direction and exposes some massive conglomeratic beds parallel to the Vourikos River. Height difference from the bottom of the river valley to the top of Roghi Mountain exceeds 700 m. There are a number of distinct "spurs", or small valleys that cut into Roghi Mountain on both the eastern and western profiles. These spurs often appear as segment boundaries (Figure 21 and Figure 22), this does not mean that some layers cannot be correlated across different segments, this is fully discussed in Chapter 5. The eastern profile of Roghi Mountain was divided in five segments.

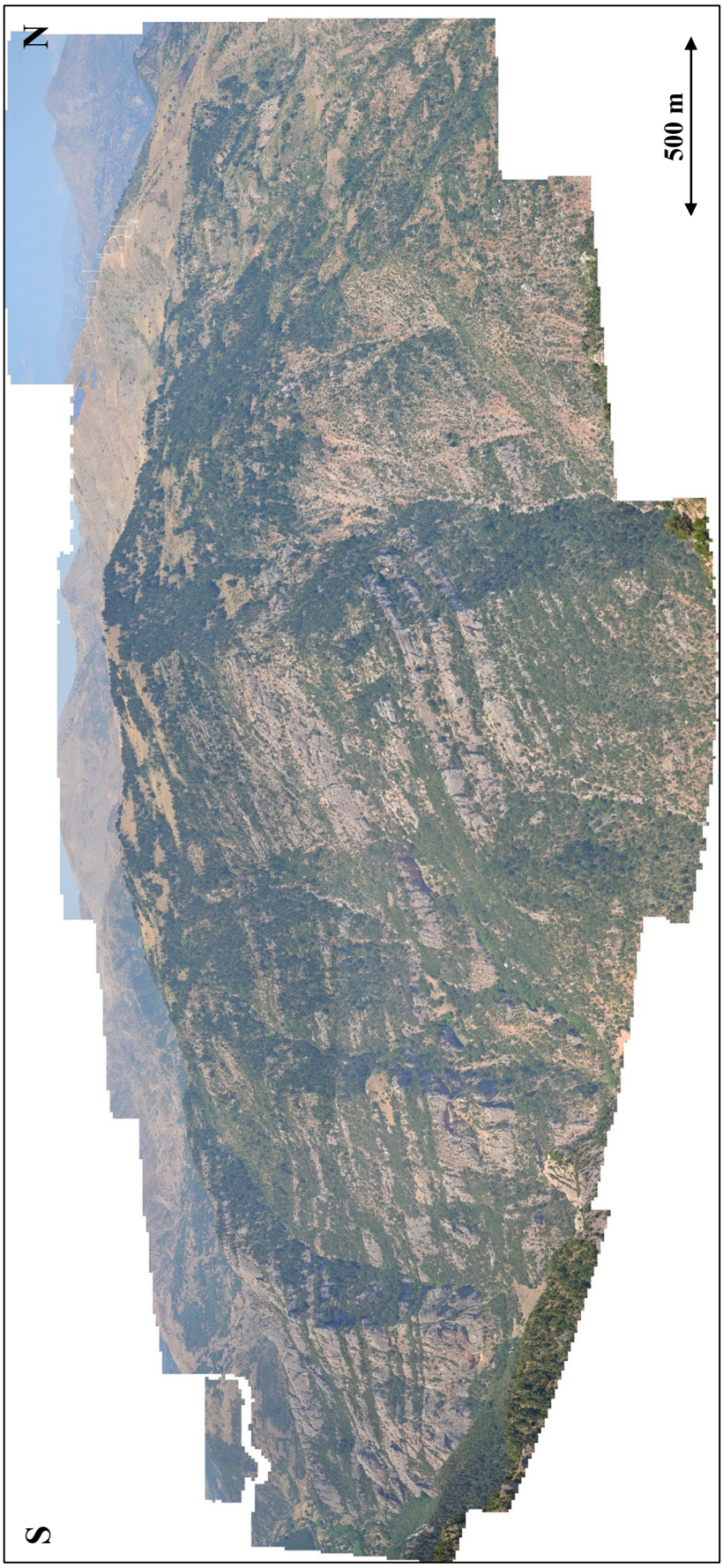

Figure 21 Overview of eastern profile of Roghi Mountain.

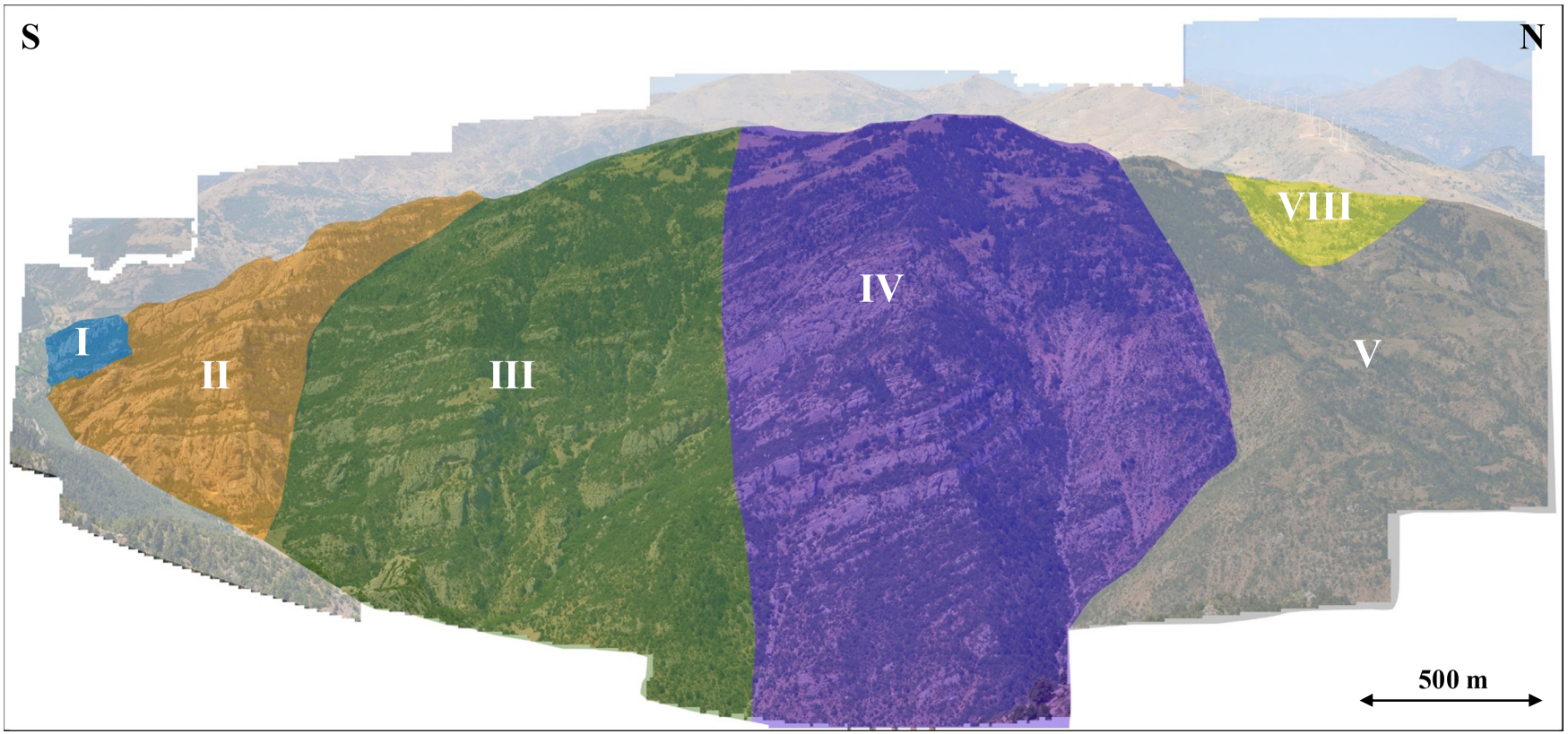

Figure 22 Eastern profile of Roghi Mountain with segments.

4.2.1 Segment I

This southernmost segment of Roghi Mountain includes two lithological units, pre-rift basement and the Group 1 of the Roghi Mountain sedimentary rocks. The Kerpini Fault cuts through this segment with basement visible in the footwall of the Kerpini Fault (Figure 23). Four individual layers have been defined for this segment that further are divided in two layer groups (Figure 23). The areas between each of these layers are heavily vegetated, other areas of Roghi Mountain indicate that finer grained layers underlie these areas with dense vegetation. The beds of this segment all have a light brown to white colour shading, with clast sizes (on average) varying between cobble to boulder size. The northernmost boundary of this segment is located along a small gully.

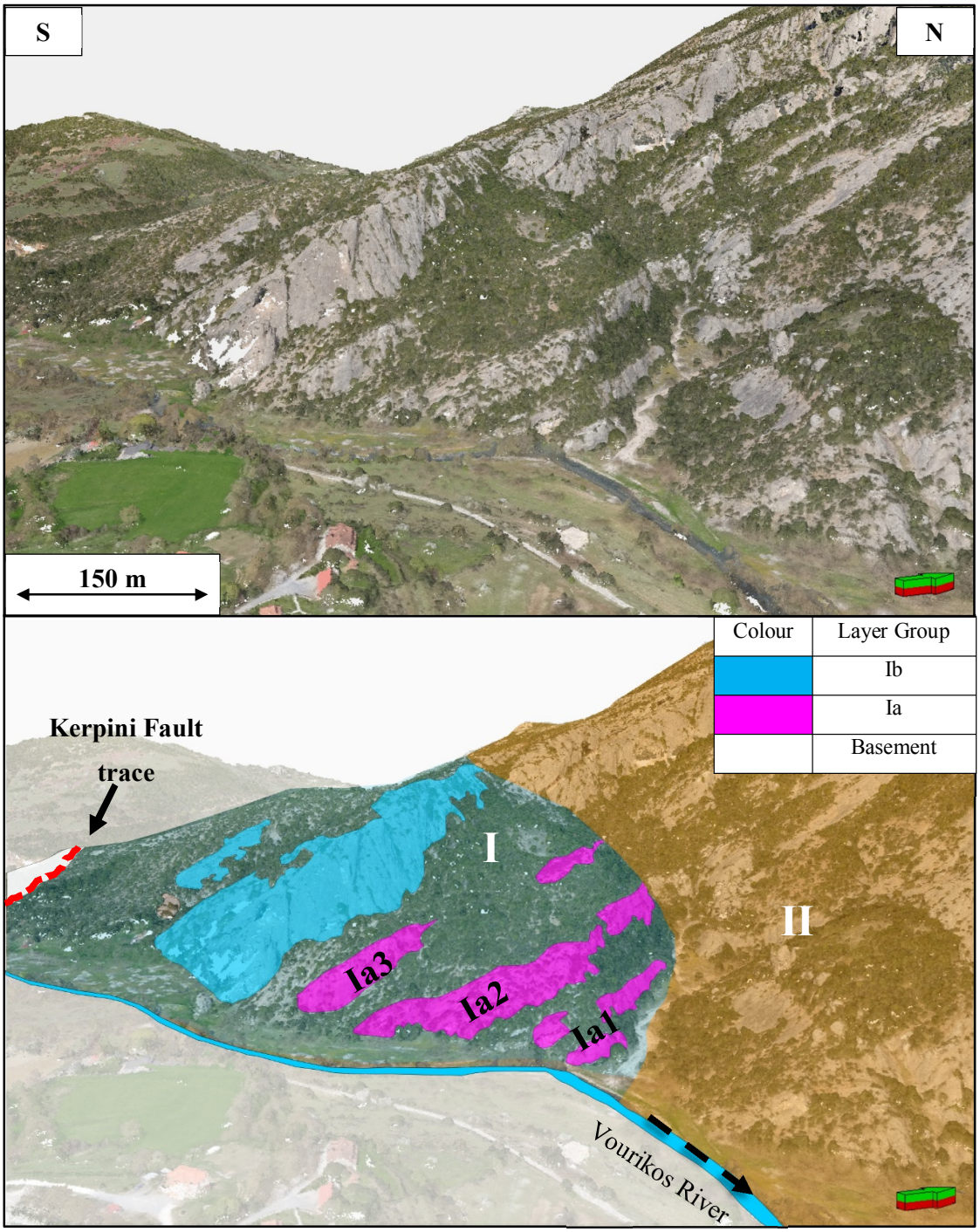

Figure 23 Display of the Segment I with distinguished layer groups, location of Segment I visible in Figure 20 and Figure 22.

Planes were constructed in Petrel E&P (2014) for layer group Ia, these planes represents the dip and strike of the layers and are plotted in Figure 24. Bed Ib was not included here because the layer tracing was very uncertain as the base of the bed appeared unclear. The planes suggest that the dip direction of the layers is shifting southward as one moves up in the vertical layer succession. The dip direction of the layers varies from 240° (Ia1) to 225° (Ia3).

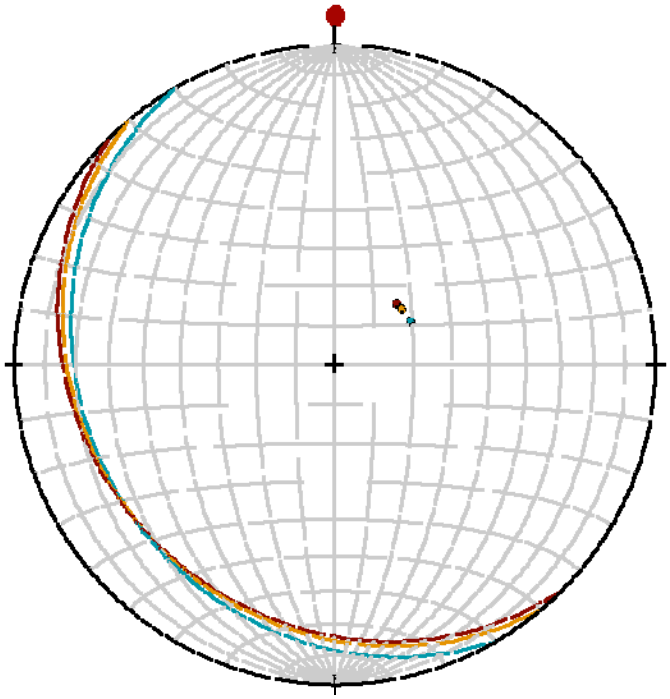

Layer	Dip Dir	Dip
Ia3	225	22
Ia2	230	22
Ia1	240	22

Figure 24 Stereonet with the planes constructed for three layers in Segment I. Poles and planes colour coded according to the small table.

Individual layer thickness of beds in layer group Ia in Segment I is ca 20 meters. The thicker bed Ib is roughly 35 m thick. Bed Ia2 had enough exposure and did not seem overly effected by erosion such that some thickness variations measurements could be made (Figure 25).

From Figure 25 an increase in thickness seems to occur in the north-west direction. However, the easternmost part of this layer seems quite weathered which could effect the quality of the measurements as they top and base of the layer is not clearly defined.

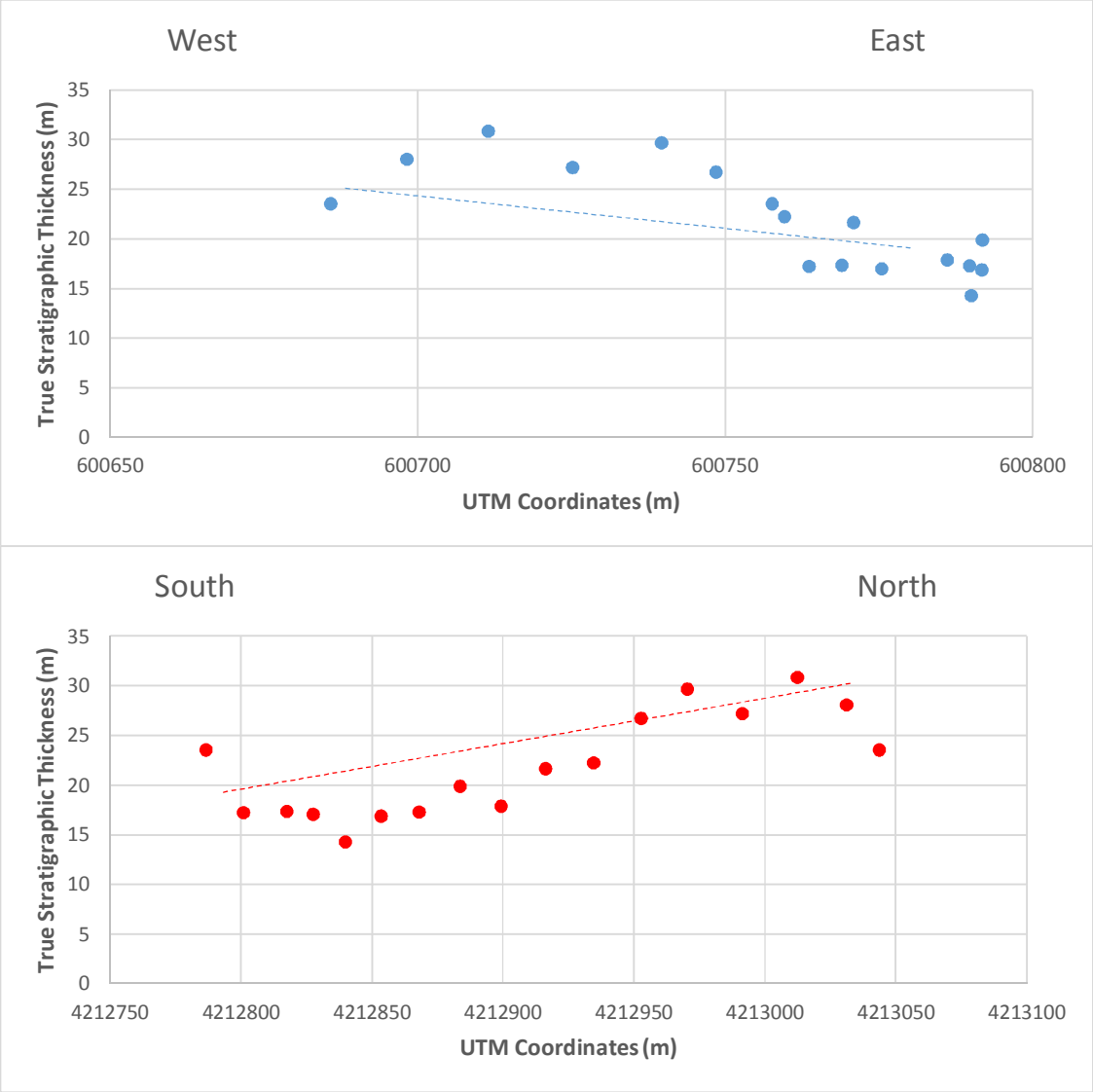

Figure 25 Graphical display of thickness variations along bed Ia2. There seems to be a slight decrease in thickness in the eastern direction, as well as a slight increase in thickness towards the north. Dashed lines indicate trend lines.

4.2.2 Segment II

Twelve separate layers have been identified within this segment (Figure 26). Distinct changes occur through different sections of the vertical layer succession, however some general trends are observable. Firstly, the layer thickness decreases up the section, and secondly the dip direction of the layers is directed more and more southwards as one moves up the vertical succession. Also, these massive conglomerate layers (Figure 27) have a very light brown, almost white, colour shading, with clast sizes (on average) varying from cobble to boulder size.

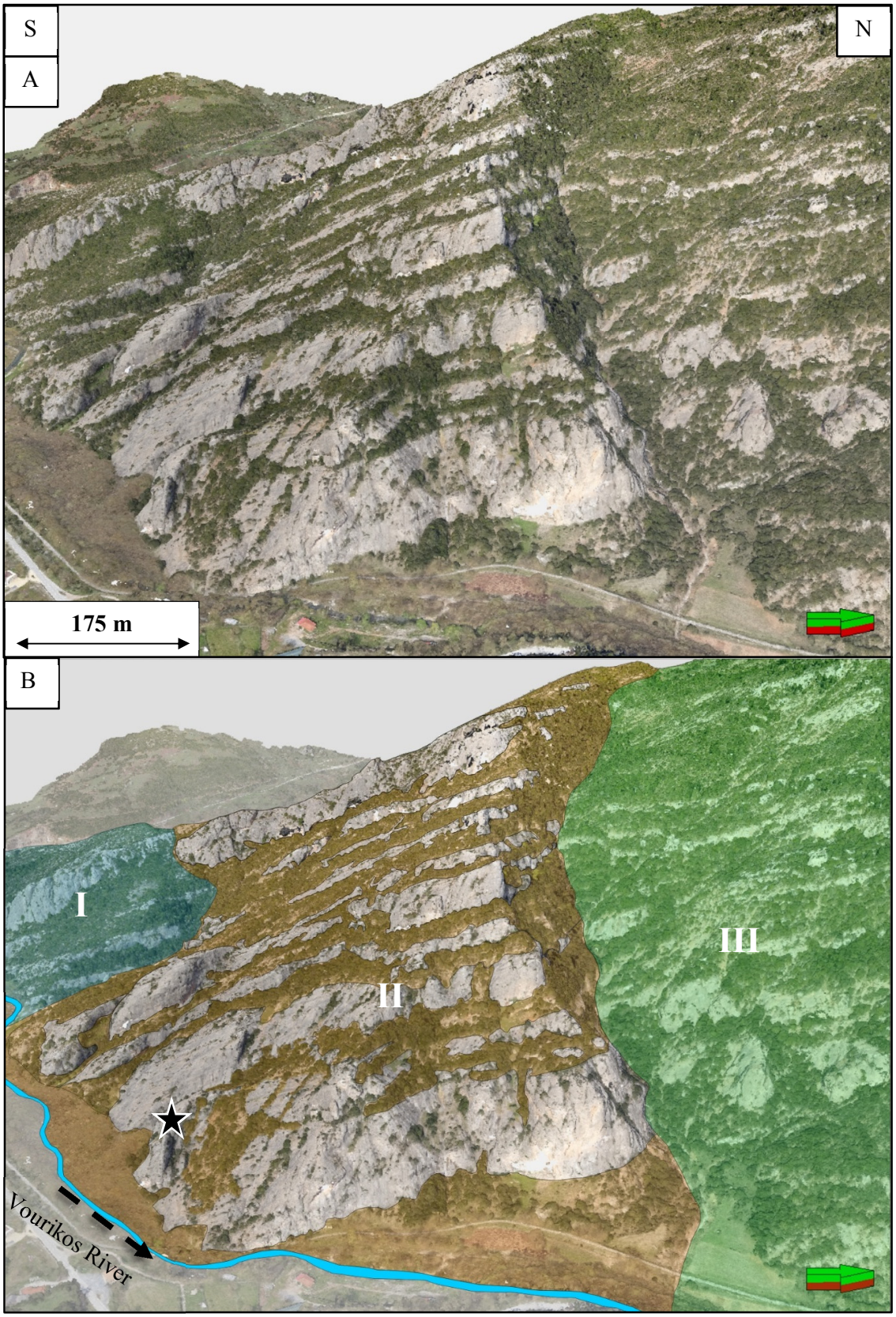

Figure 26 Image of LiDAR point cloud with focus on Segment II (A). Representation of Segment II (orange background colour), blue and green colour represents Segment I and III respectively. Locations of segments visible in Figure 20 and Figure 22. The black star indicates the location of the photograph in Figure 27.

Figure 27 Outcrop of one of the typical thick conglomerate beds found across many parts of the eastern profile of Roghi Mountain.

In Figure 28 colour codes and layer groups have been assigned to the different layers of Segment II.

Layer group IIa (Figure 28) all dip south-west (228°) with a dip angle of 20°. The beds are thick and massive compared to the thin vegetated layers separating them. Towards the southern part of these beds, the vegetated thinner layers seem to disappear and individual layers cannot be differentiated. This is especially prolific for two areas of layer group IIa, where it could appear as thinner layers stop against a massive conglomerate layer (marked in Figure 28).

Layer group IIb (Figure 28) appear to dip slightly further towards the south (218°) compared to the beds of layer group IIA, more surprisingly they seem to have a higher dip angle of ca 25°.

South of the layers IIb there appears to be a continuous layer (marked as IIc in Figure 28) seemingly onlapping layer group IIb. No plane could be generated for this layer that would follow the layer trace in a natural way. Overlying layer IIc, there is a thick unit (marked as IId in Figure 28) where the base of the layer is not well exposed. Whether this actually is one single massive layer or several bed converging, or eroding into each other is very difficult to determine. The upper layer group IIe is made up of two distinct layers which are quite thin compared to the most of the other beds of Segment II. These layers also have a significantly

lower dip angle of around 15°, but more or less the same orientation as the underlying layers (roughly 215°). Figure 29 is a stereonet representation of most of the layers of Segment II.

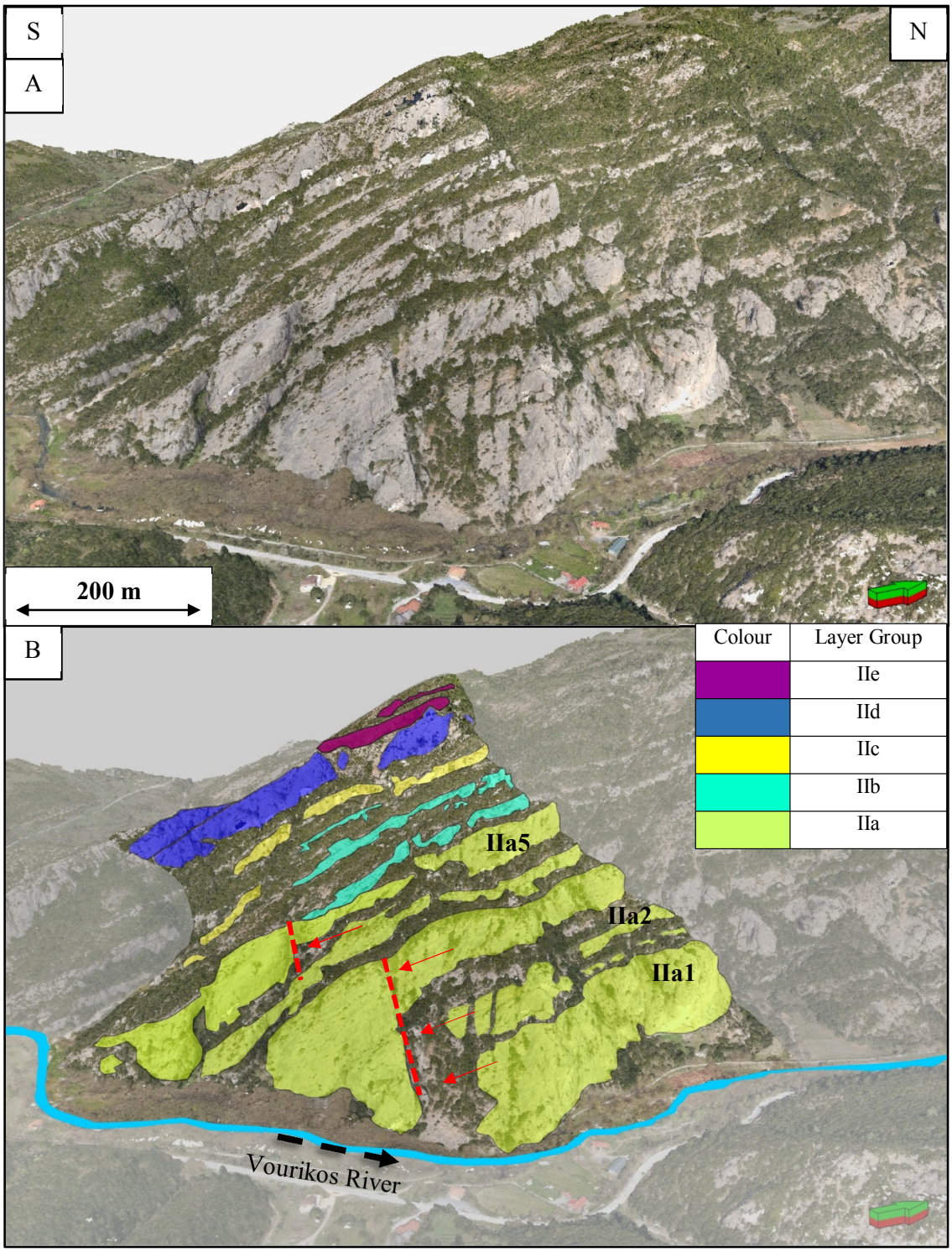

Figure 28 (A) LiDAR image with focus on the area of Segment II. (B) Layers of Segment II traced, grouped and colour coded. Segment locations visible in Figure 20 and Figure 22. Beds marked with letters IIa1, IIa2 and IIa5 were measured for thickness variations. Red arrows and dashed lines represent where thinner layers stop against a single massive conglomeratic layer.

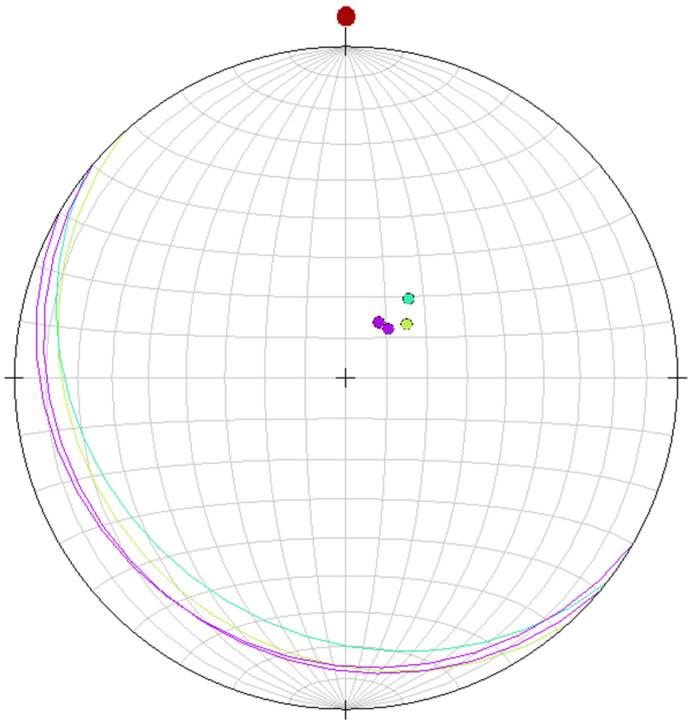

Layers	Dip Dir	Dip
IIe	220-210	16
IIb	218	25
IIa	228	20

Figure 29 Stereonet with the planes constructed for layer groups of Segment II. Planes and poles marked according to layer groups in the small table.

Thickness analysis of this segment is mostly applicable for layers in layer group IIa, this is due to the nature of the outcrop, as only this part of the segment has sufficient exposure in the outcrop for the measurements to make sense. The two lowermost layers, IIa1 and IIa2, are plotted in the thickness graphs in Figure 30. No clear trend can be derived from any of these two layers. Layer IIa5 (Figure 30) has a slight trend that indicates increased thickness towards the south-east, however this could be caused by two layers merging into one thicker layer (Figure 31) in this part. This merging of layers towards the south can also be observed in other parts of the mountain as well, where a vegetated area gradually disappears and two conglomerate layers form together one thick layer. Layer IIe (Figure 32) exhibits a quite distinct trend with layer thickness decreasing towards the north-west.

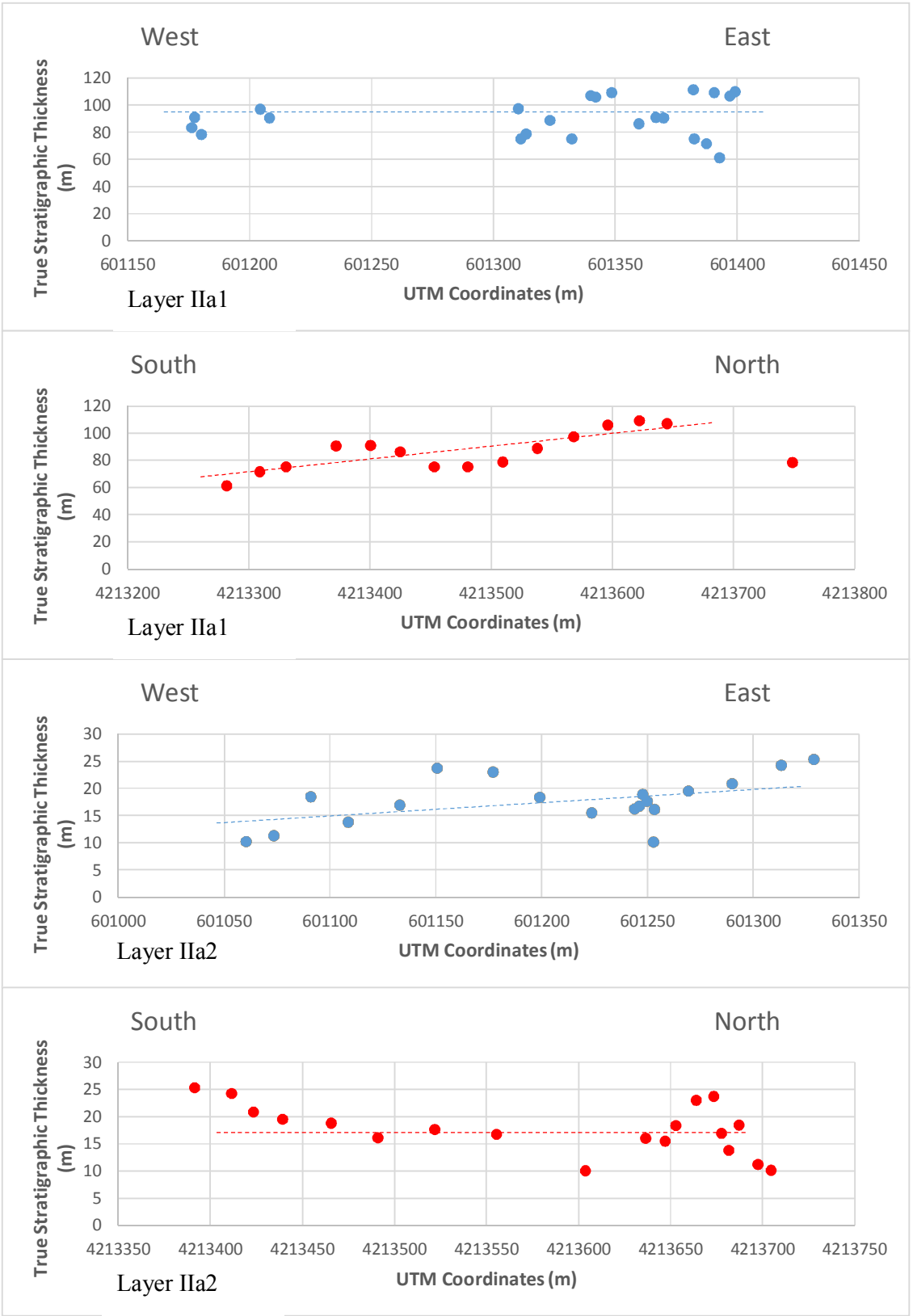

Figure 30 Thickness variation charts for layers IIa1 and IIa2. Only a increase in thickness towards the north for layer IIa1 can be assumed from these plots. For layer IIa2 the variation in thickness is only about 10 m, this is to small to be regarded as a strong trend in the layer thickness.

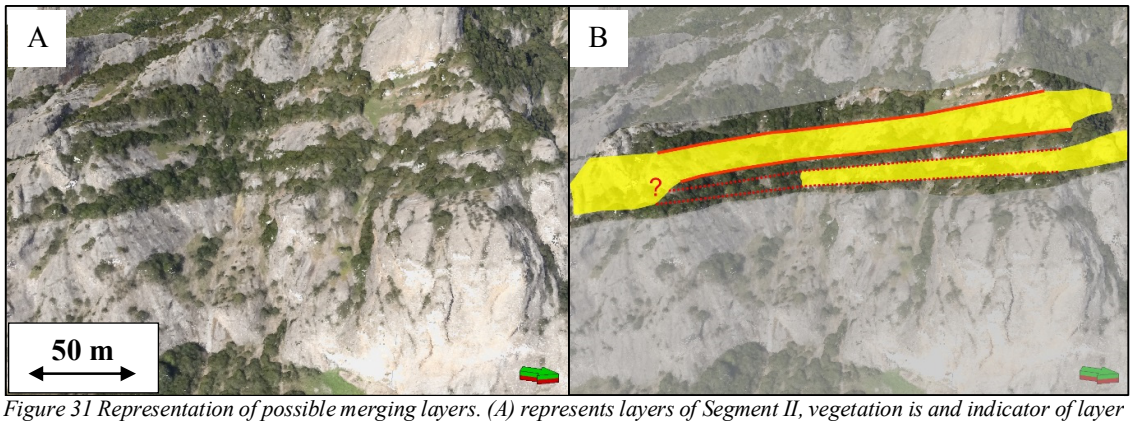

Figure 31 Representation of possible merging layers. (A) represents layers of Segment II, vegetation is and indicator of layer separation. (B) The upper layer marked in yellow seems to thicken towards the south, possibly caused by the merging of the thinner layer located below.

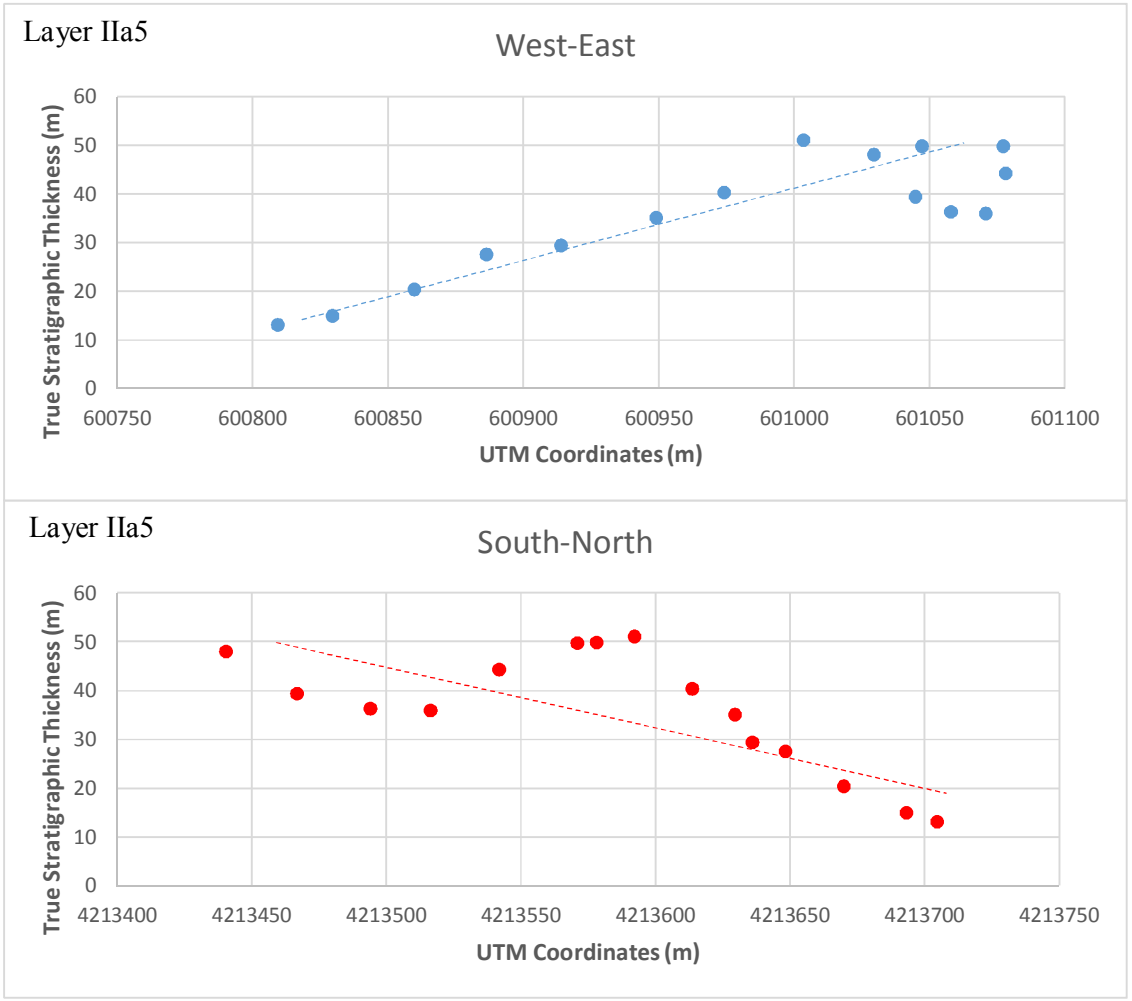

Figure 32 Thickness variation charts for layer IIa5. There is a clear increase in thickness towards the east and towards the south for this layer.

4.2.3 Segment III

Compared to Segment I and II where massive conglomeratic units dominate, Segment III displays a quite different character. Many of the layers of this segment are quite poorly exposed, this creates uncertainty when analysing the continuity of layers. Segment III also contains one of three basement exposures found in Roghi Mountain. All layers of this segment exhibit the same light brown to white colour shading, with clast sizes (on average) varying between cobble to boulder size.

In the northern part of Segment III there is an basement outcrop besides the Vourikos River (Figure 33). Roughly 90 m of basement exposure (Figure 34) is visible in the north-south direction, and ca 30 m up the vertical succession at its maximum. The contact drops in elevation moving southwards. Syahrul (2014) interpreted the northern part of the basement contact as a fault, and the southern as a unconformity. The initial field interpretations support the interpretation by Syahrul (2014), and this fault is further discussed in chapter 5.1.3.

The most massive beds of the syn-rift infill are the lower layers of layer group IIIa marked in Figure 33 as IIIa1 and IIIa2. These beds have a dip direction of 228° and a dip angle of 20°.

Layer group IIIb (marked in Figure 33) is quite poorly exposed, therefore dip and dip directions were not estimated for this unit. One possibility is that recent erosion from the upper parts of Roghi Mountain has covered parts of these layers. In the area below layer group IIIb and in the boundary between Segment III and IV there is an area where no continuous layers are observable, and a typical fan-shape (conical shape) is visible in the topography. Field observations indicate that there is a difference in colour and sorting of the conglomerates outcropping within the fan area Figure 35. One possibility is that beds from layer group IIIa have been moved out of their original place, i.e. slumping due to erosion and transportation of material from higher up in the topography. If this indeed is a fan, the fan apex appears to originate near the boundary between Segment III and IV.

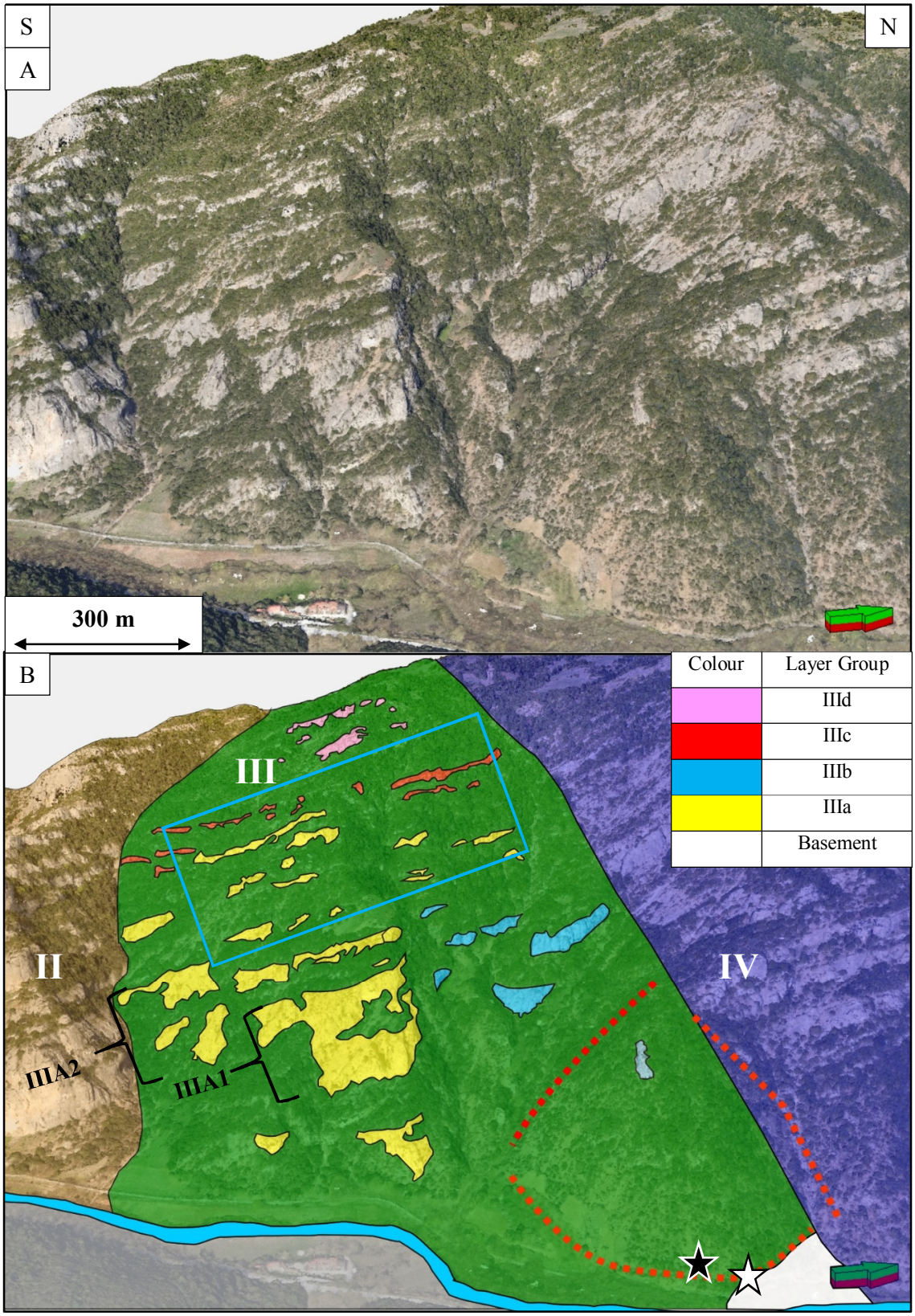

Figure 33 (A) represents LiDAR point cloud visualization of segment III. (B) displays division of Segment II, III and IV in orange, green and purple, respectively. Segment locations visible in Figure 20 and Figure 22. Layer groups marked in different colours and possible outline of recent fan marked with red dashed lines. White star represents location of photograph in Figure 34, black star represents location of Figure 35. Blue rectangle represents zoom in visible in Figure 37.

Figure 34 Basement outcrop located within Segment III, location of photograph marked in Figure 33.

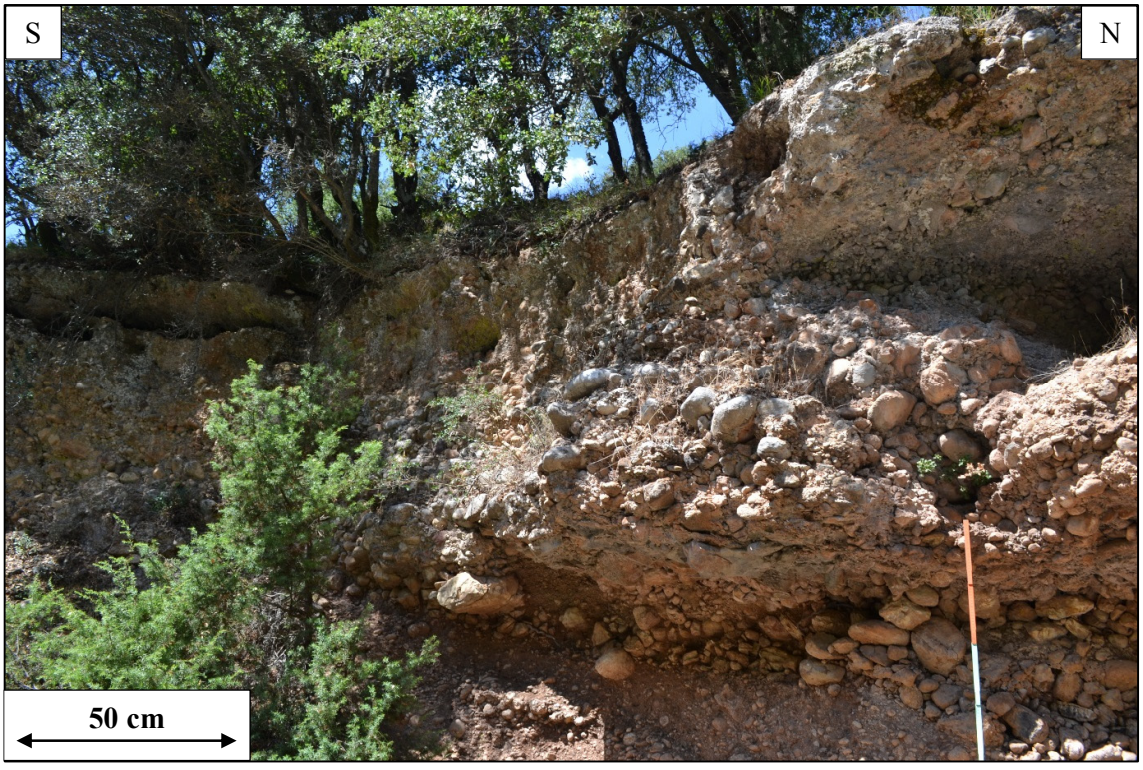

Figure 35 Outcrop of conglomerates within the conical-shape in the topography. Location marked in Figure 33.

Layer group IIIc in Figure 33 is estimated to be westward dipping (240°) and with a dip angle of around 18°. The beds of layer group IIIc are relatively thin with an average thickness of ca 3 to 4 m. Since these beds are so thin and the outcrop is quite limited, layer tracing proved challenging and uncertain. The quality of the dip and dip direction estimates were also effected by this. A summary of the planes crated for Segment III is visible in the stereonet in Figure 36.

From layer group IIIa to IIIc there appears to be a relatively substantial change in the layer geometries. A close up view of layer IIIa7 and IIIc2 (Figure 37) suggest that these two layers approach each other as one moves from the southern part of the segment and northwards. Layer IIIc2 could be interpreted to onlap the layer group IIIa.

Layer group IIId at the very top of the segment is quite poorly exposed, but the layers is estimated to have a dip direction of 220° and dip angle of 16°.

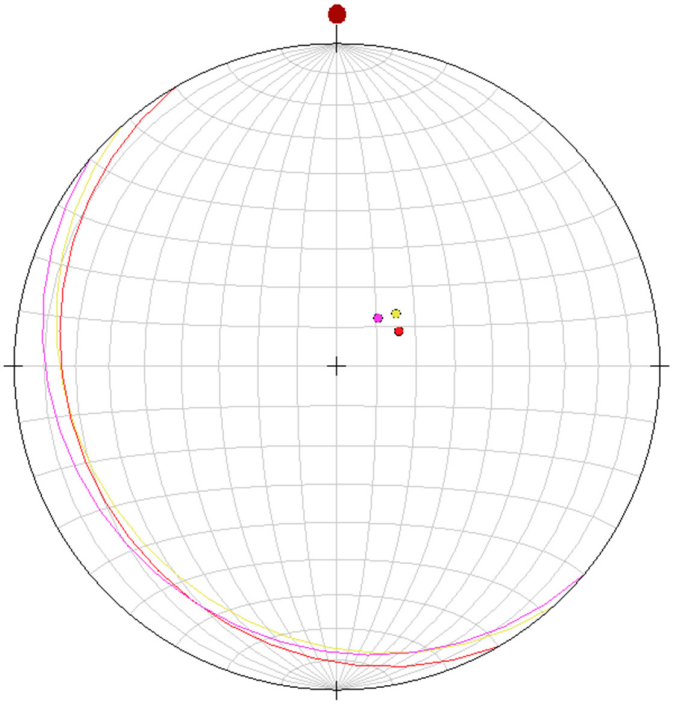

Layers	Dip Dir	Dip
IIId	220	16
IIIc	240	18
IIIa	228	20

Figure 36 Stereonet with the planes constructed for the layer groups of Segment III. Planes and poles marked according to layer groups in the small table.

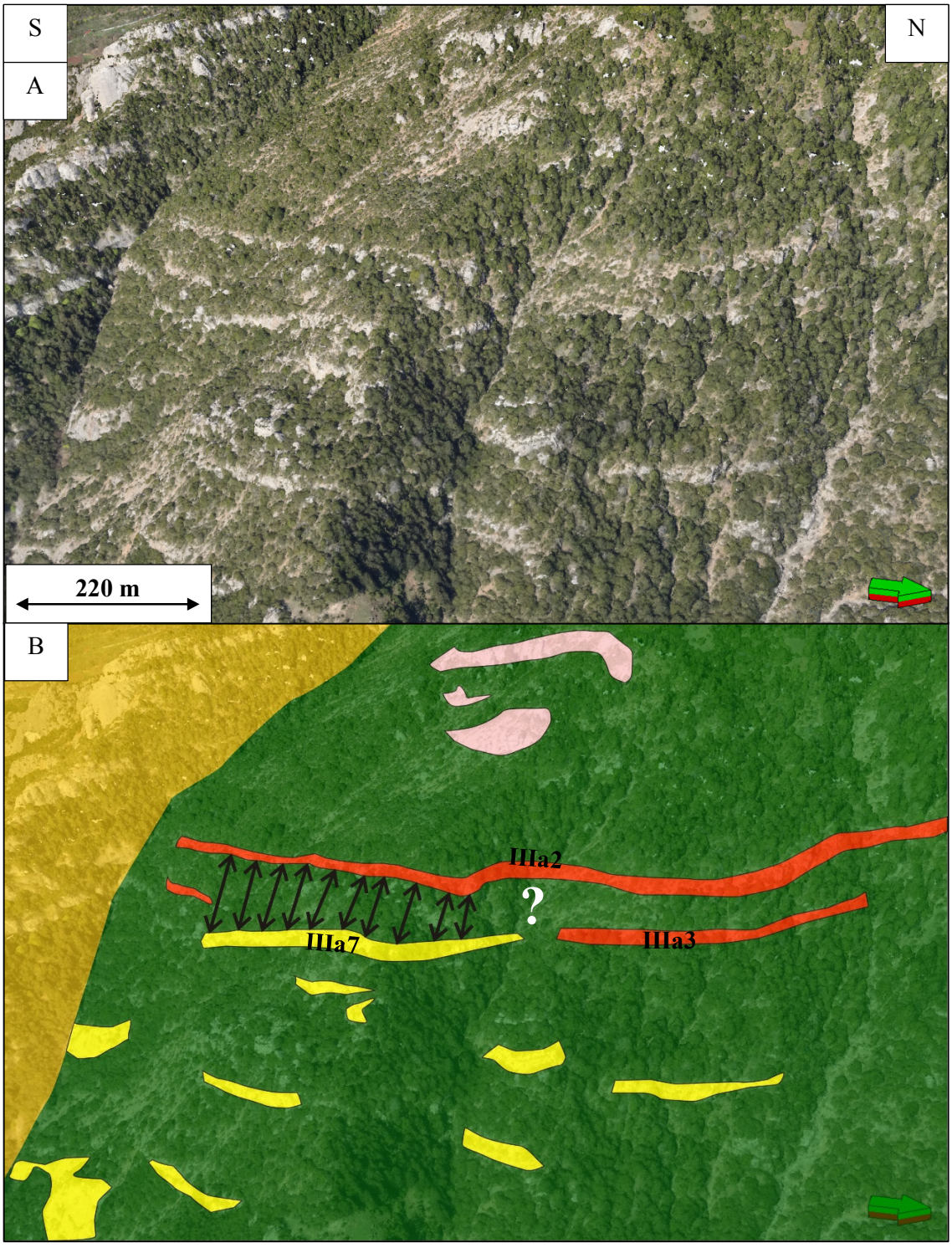

Figure 37 (A) represents a zoom in of the blue rectangle marked in Figure 33, only from a different prespective. (B) represents the traced section with segment I highlighted in orange and the green background colour representing Segment II. The arrows indicate the decrease of spacing between layers IIIa7 and IIIa2. The question mark indicates an uncertain layer trace, i.e it is uncertain if layer IIIa7 continues or if this yellow layer truncates against layer IIIa3.

4.2.4 Segment IV

At the boundary between Segment III and IV (Figure 38) there is a quite distinct change in the character of the outcrops between these two segments. Moving north from Segment III into Segment IV there is a distinct change from the thin beds with presumably fine sediments to massive beds (layer group IVc in Figure 38). This distinct change could be the result of a rapid facies change from Segment III to Segment IV, however this change appears as a linear feature highlighted by the termination of the layer groups IVb, IVc and IVd (Figure 38). The basement outcrop visible in Figure 33 and Figure 34 also appears to terminate along this same linear feature.

These two observations strongly argue for the presence of a fault between these two segments, as has been interpreted in previous work in this area (Dahman, 2015; Hemelsdaël et al., 2015; Syahrul, 2014).

Layer group IVa has been defined for the beds near the base of Segment IV (Figure 38) and have a dip of around 30° with a dip direction of 220°, these are the steepest layers recorded in Roghi Mountain. Clear outcrops of layer group Iva are scarce, therefor the quality and reliability of dip and dip direction estimates are effected by this. The colour of layer group IVa exhibits a darker brown shading compared to the typical light brown to white colour shading visible for the other layer groups of this segment. The clast sizes (on average) vary between cobble to boulder size for all layer groups of Segment IV.

Layer group IVb (Figure 38) have a 25° dip angle in the same direction as layer group IVa. The layers of IVb exhibit a sort of slumping, or bending behaviour at the southernmost part of the outcrops. This area is in close relation to where the interpreted fault plane mentioned earlier between Segments III and IV.

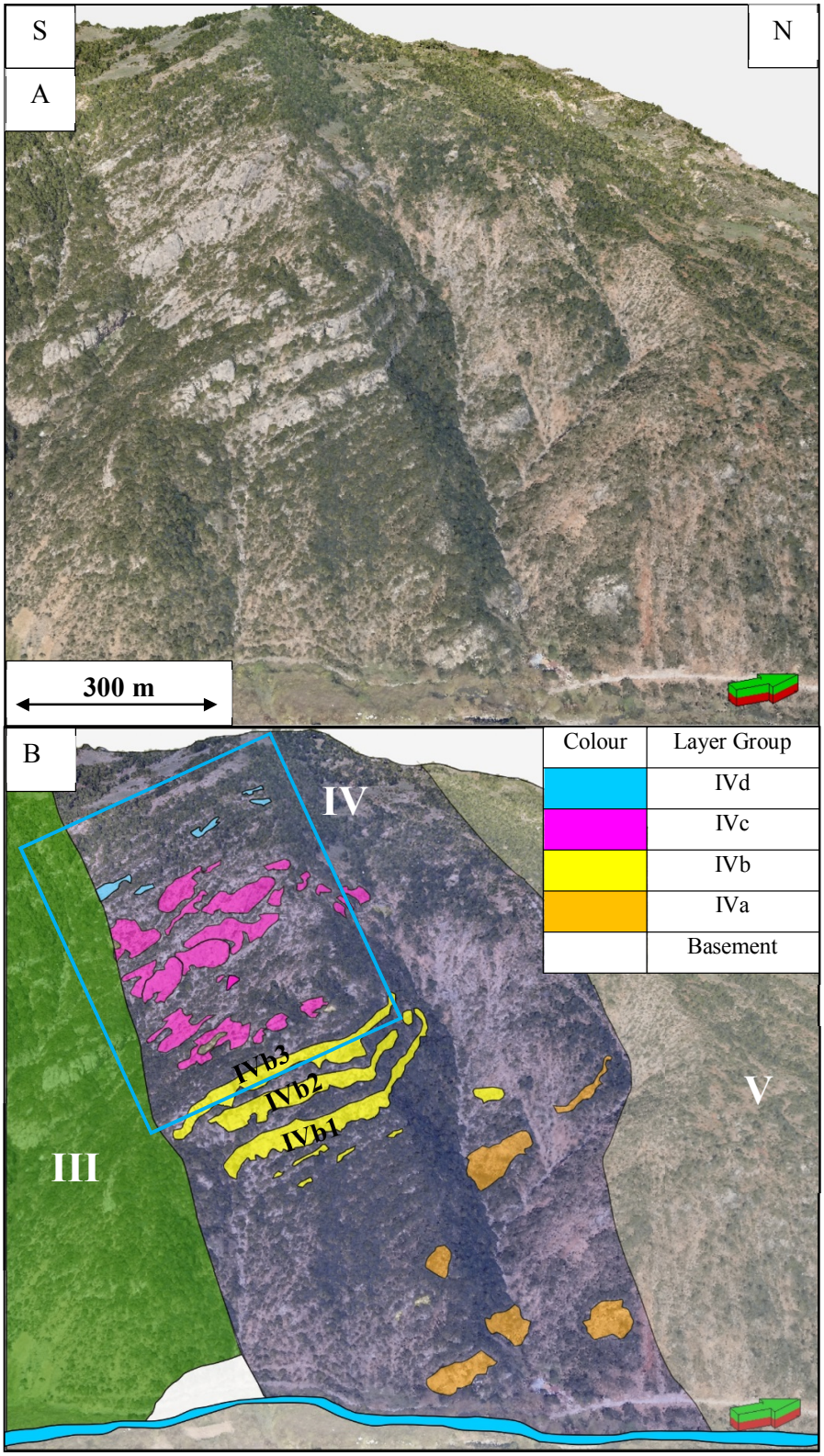

Figure 38 (A) LiDAR point cloud visualization with focus on Segment IV. (B) Display of segment boundaries and layer traces, segments marked with white letters. Legend indicating layer groups. Blue rectangle representing zoom in visible in Figure 39. Segment locations visible in Figure 20 and Figure 22.

Any clear layering is hard to differentiate in layer group IVc (Figure 38 and Figure 39). The beds of layer group IVC appear quite massive, but also chaotic. It is difficult to pick out any clear top or base of the layers within layer group IVc. Although it is hard to see from Figure 38 or Figure 39, the thickest part of layer group IVc forms a small shelf in the Roghi mountainside, this topographic feature suggest that erosion might have effected this area. One possibility is that this entire "shelf" area has slumped slightly causing the layer appearance to seem anomalous compared to the other units of Segment IV. Because of the characteristics described for the layer group IVc, any reliable measurements or approximations for dip and dip direction is difficult to determine.

Layer group IVd (visible in Figure 38 and Figure 39) are much thinner compared to any of the other layer groups of Segment IV. Layer thickness does not exceed 8 m and the average is ca 2 m. The beds of layer group IVd dip at an angle of 25° towards the south-southwest (195°). The dip direction shift southwards as one moves up the vertical succession through the different layer groups. Figure 40 is a stereonet summary of planes for Segment IV.

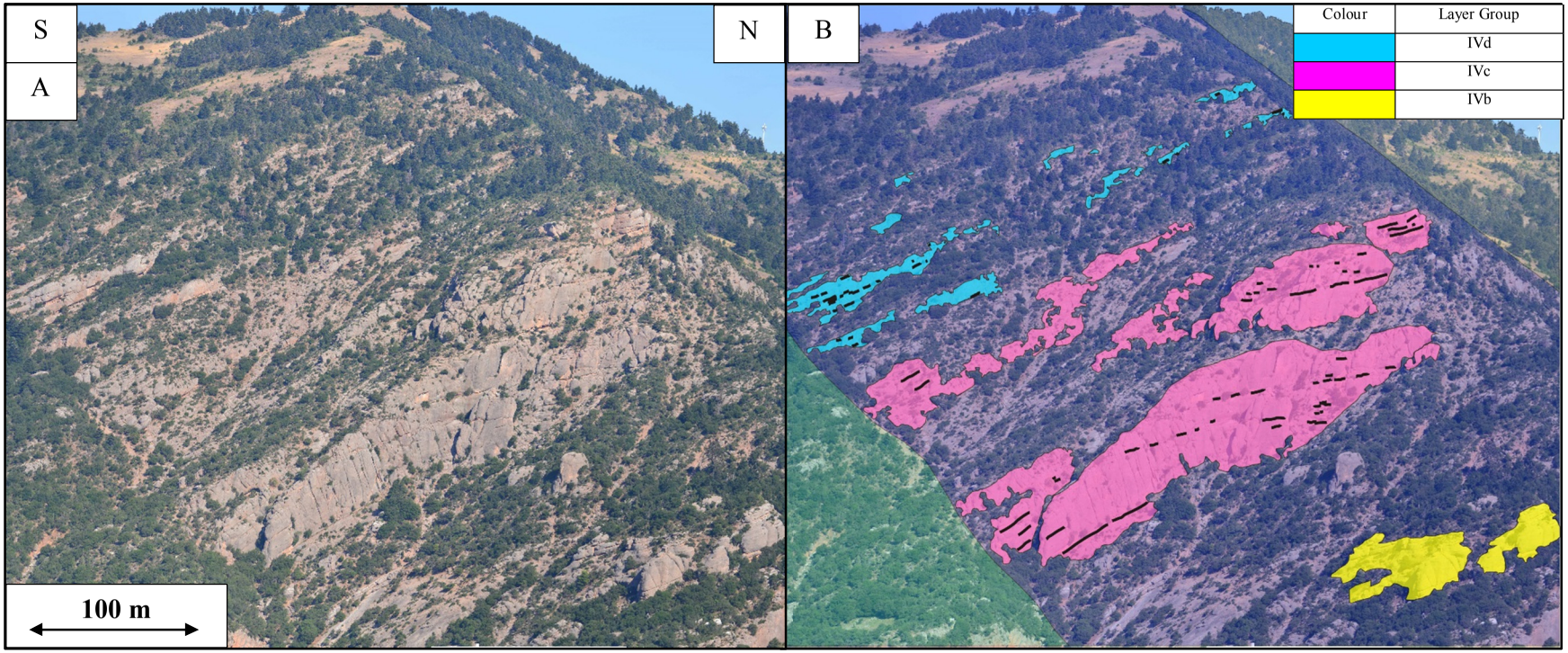

Figure 39 (A) photograph with focus on layer groups IVc and IVd of segment IV. (B) representation of layer traces..

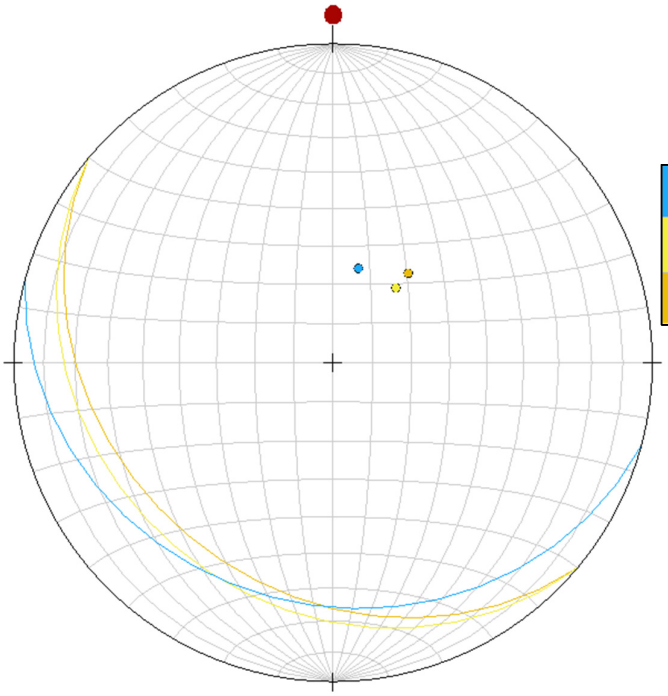

Layers	Dip Dir	Dip
IVd	195	25
IVb	220	25
IVa	220	30

Figure 40 Stereonet with the planes constructed for the layer groups of Segment IV. Planes and poles marked according to layer groups in the small table.

Thickness analysis was carried out on the three distinct layers of layer group IVb (marked as IVb1,IVb2 and IVb3 in Figure 38). These layers have enough exposure in the north-south and east-west directions to deduct thickness trends. However, the thickness of these three beds seem more or less constant as there are no clear trends in Figure 41 and Figure 42, except for layer IVB2 which has a relative small increase in thickness towards the south-east.

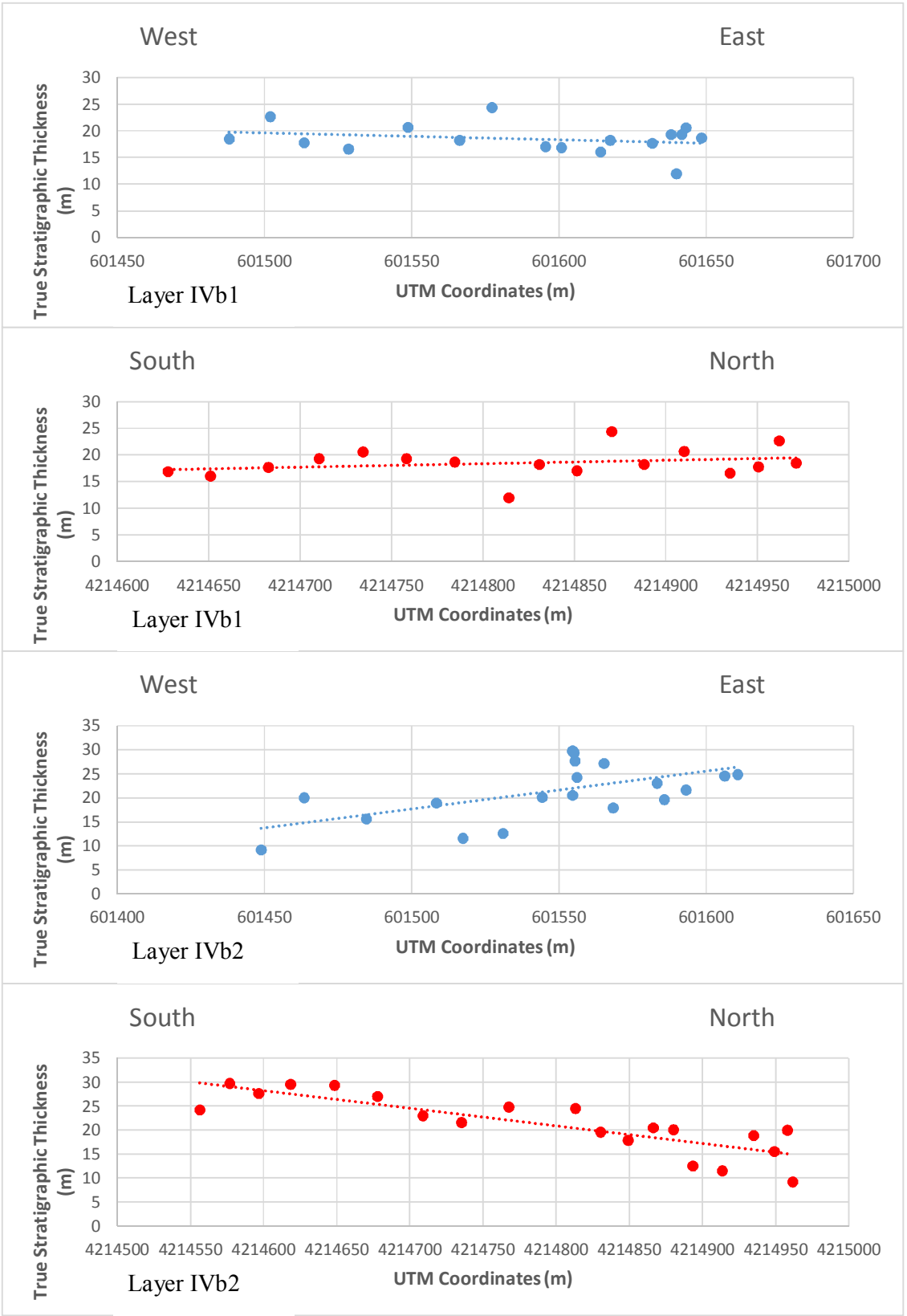

Figure 41 Thickness variation charts for layers IVb1 and IVb2. The thickness for layer IVb1 appears constant in all directions. An increase in thickness towards the east and towards the south for layer IVb2 can be assumed from these plots.

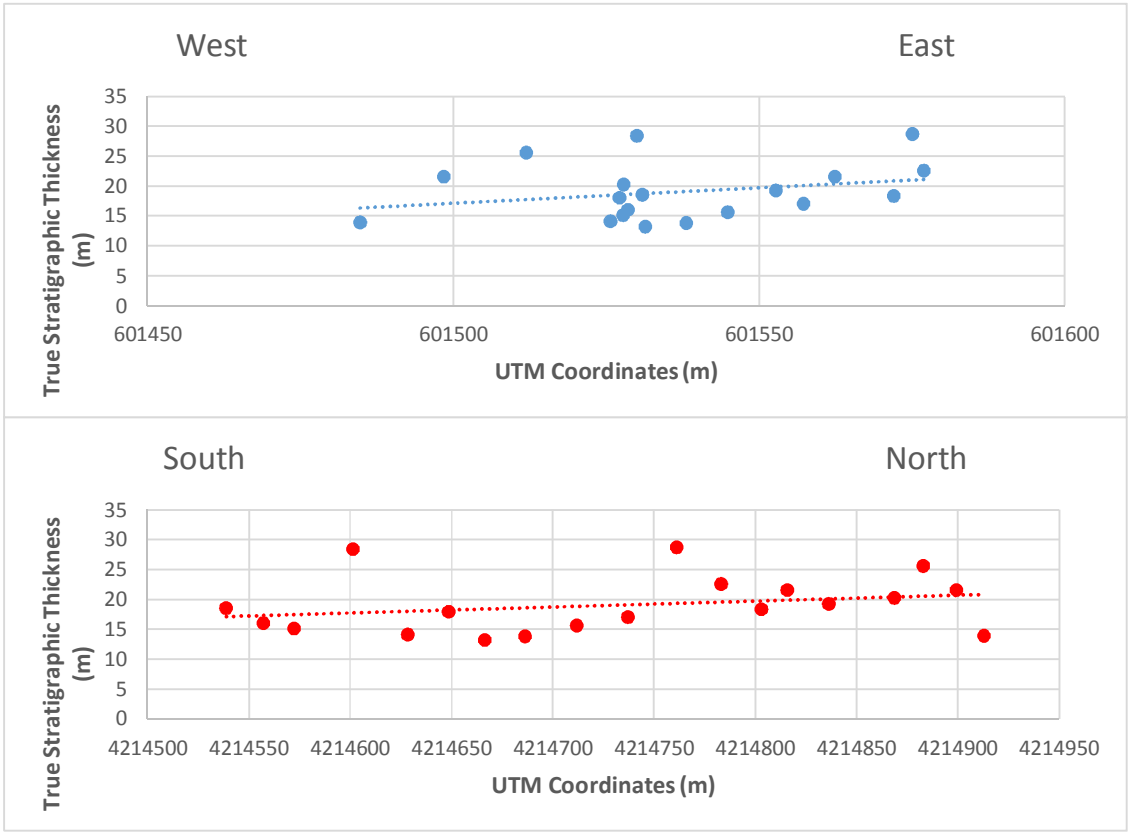

Figure 42 Thickness variation charts for layers IVb3. The measurements for this layer were ambiguous because of uncertain bed tracing, no clear trends are visible except for a small increase in thickness in the eastern direction.

4.2.5 Segment V

Segment V (Figure 43) differs from the other segments as there are generally very few visible layers throughout the entire segment. Only two outcrops of any continuous layers are visible (marked as layers Va1 and Va2 of layer group Va in Figure 43).

Within the segment (especially above the highlighted road in Figure 43) a conical shape in the topography is quite prolific. In Figure 44 this shape is especially distinct, and it appears to cover a large part of Segment V. Dahman (2015) interpreted this conical feature as a late syn-rift fan, not related to any of the other layer groups defined for any of the segments in this project.

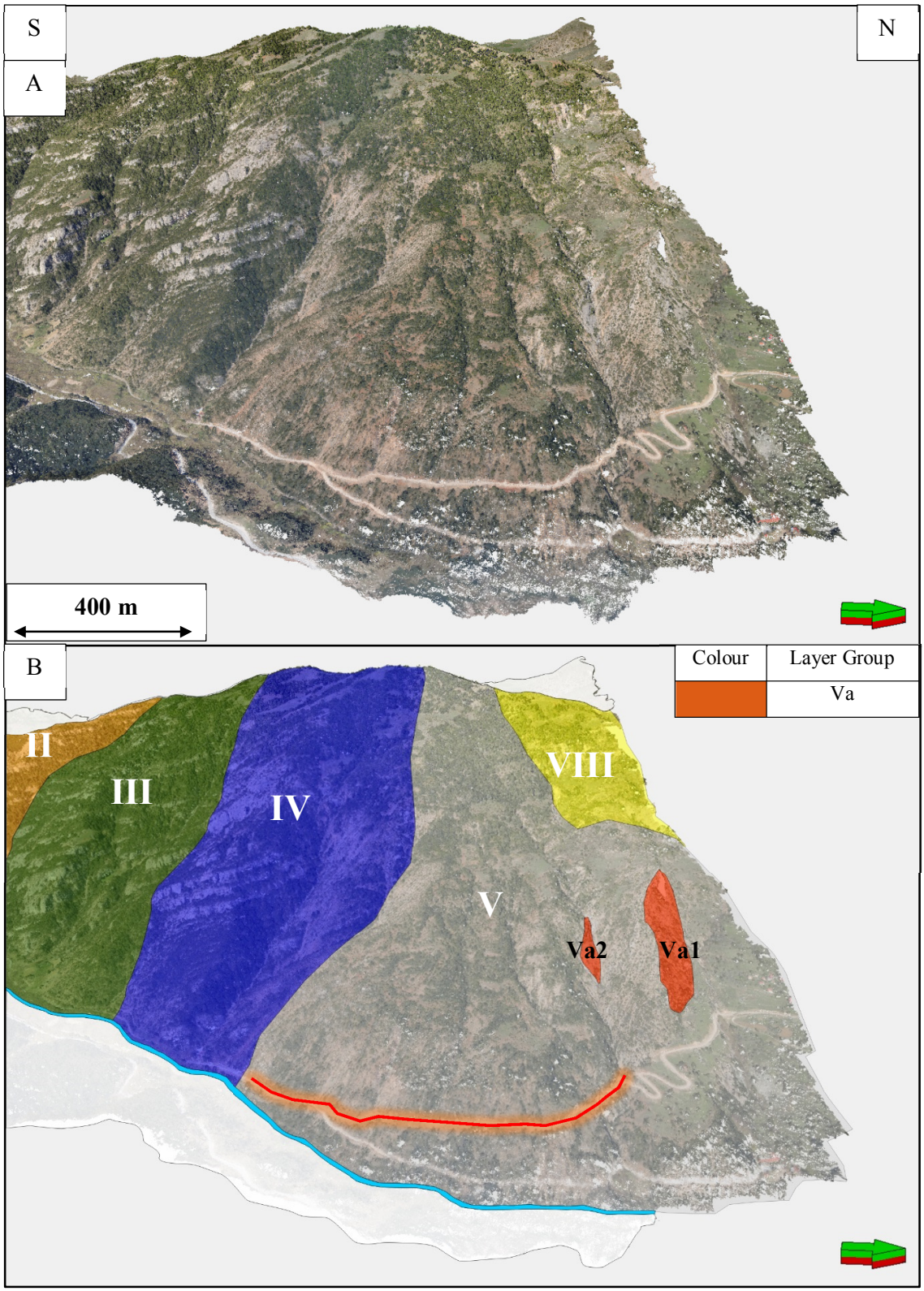

Figure 43 (A) LiDAR point cloud visualization focused on segment V. (B) Display of Segment V with boundaries. Segment locations visible in Figure 20 and Figure 22. Red line indicating road indicating the edge of a fan. Segments marked with white letters. Only one layer group was defined for this segment.

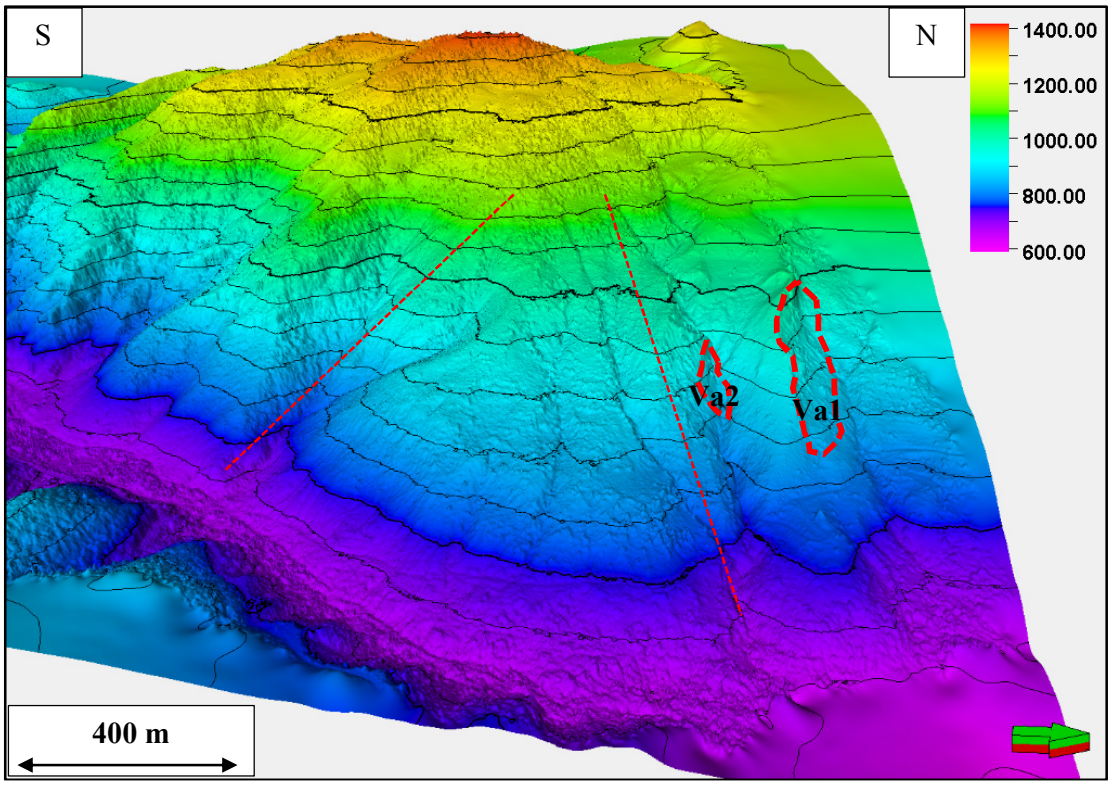

Figure 44 Surface representation of the LIDAR point cloud with elevation contours and colour scheme, legend in m. Red dashed lines representing the boundaries of the suggested recent fan, red circle represents location of outcrop visible in Figure 43.

The relatively large outcrops (marked as layer group VA in Figure 43) visible in the northern part of Segment V is not fully covered by the LiDAR data. An area of ca $1.5km^2$ of the northern part of Roghi Mountain is totally absent in the LiDAR dataset, this area is visible in Figure 45. The dataset collected by UiS (described in chapter 1.6.1) was intended to get a better coverage of Segment V, unfortunately this was not useable. During fieldwork there was not enough time to conduct a detailed study of layer group Va. However, these sediments are interpreted to be a part of the Kerpini Fault Block (part of Group 1 in Figure 16).

Some general observations could be made about layer group Va. The colour of the beds in layer group Va exhibits a darker brown shading compared to the typical light brown to white shading. Layers Va1, Va2, and Va3 (Figure 45) appear strongly effected by weathering, the top and base of any individual layer is hard to pick out both from photographs and the LiDAR point cloud, therefore dip angle, and dip direction estimates of layer group Va is highly uncertain but estimated to 35°, and ca 130° respectively. This is very different compared to most other locations of Roghi Mountain.

The northern boundary of Segment V is defined by a lithological contact between the conglomeratic layers of Segment V and the pre-rift basement. This unconformity (Figure 45) is only partly exposed in the terrain. It appears as a relatively linear feature in the upper part of Roghi Mountain, however the contact is not so clearly visible further down in the topography. Where the contact is no longer clear there seems to be another conical feature, the lithology here is much more fine grained and has a lighter brown colour compared to the beds of layer group Va. The rocks within this small conical feature also appears much less consolidated than the more massive beds of layer group Va. Therefore, this feature has been interpreted as a late fan covering the unconformity contact between the conglomeratic layers of Segment V and the pre-rift basement (Figure 45). This contact has been previously mapped by Ford et al. (2013).

4.3 Summary of Eastern Profile

The 16 different layer groups defined for the eastern profile of Roghi Mountain are all marked in Figure 46. Table 1 exhibits a summary of some key features observed for the layer groups on the eastern profile.

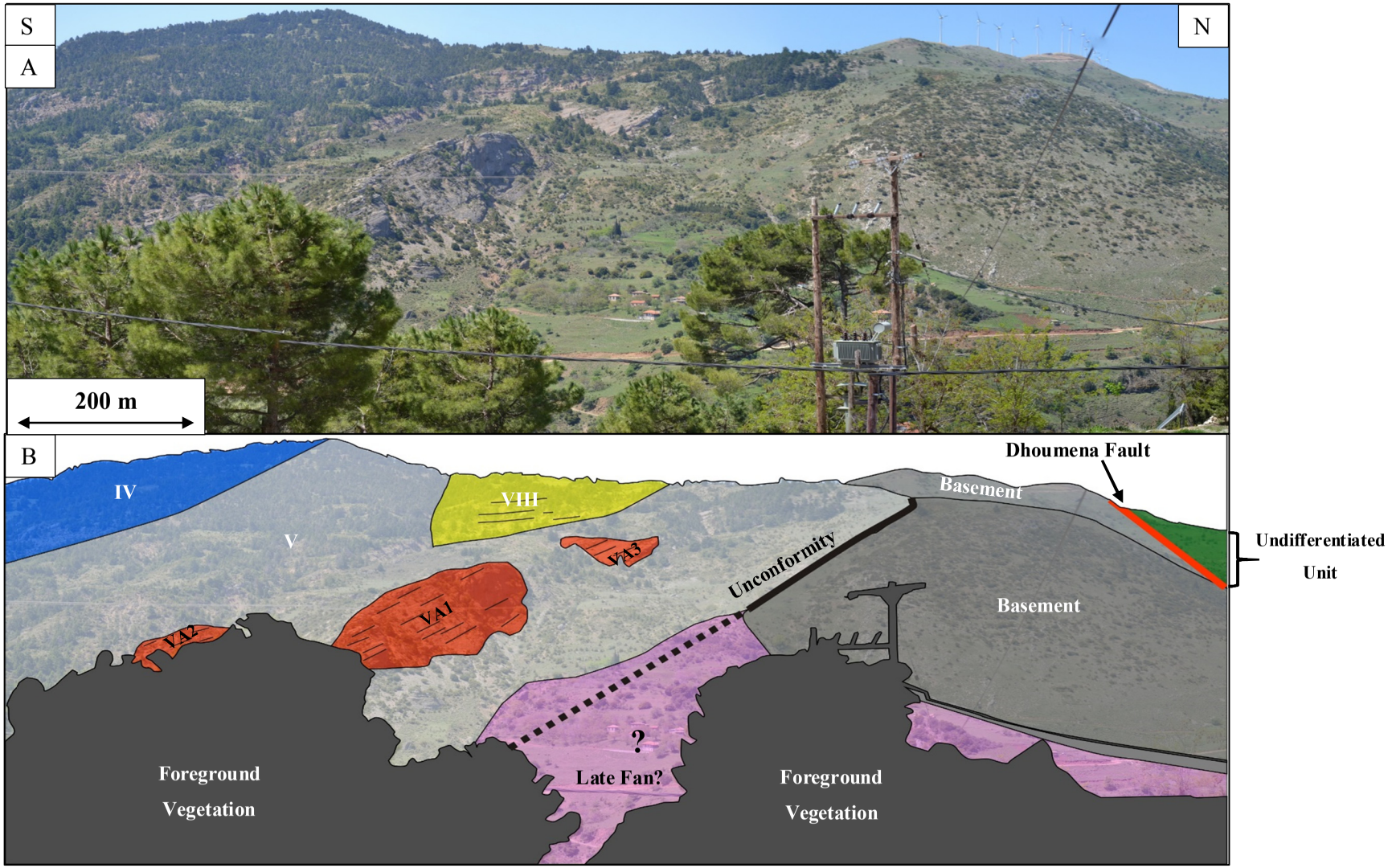

Figure 45 A) photograph of the noerthern part of Roghi Mountain and Segment V. B) Interpretation of Segment V with segment numbers in white roman numericals.. The photograph is taken more or less directly in the strike of the Dhoumena Fault. Scale appliacable near houses.

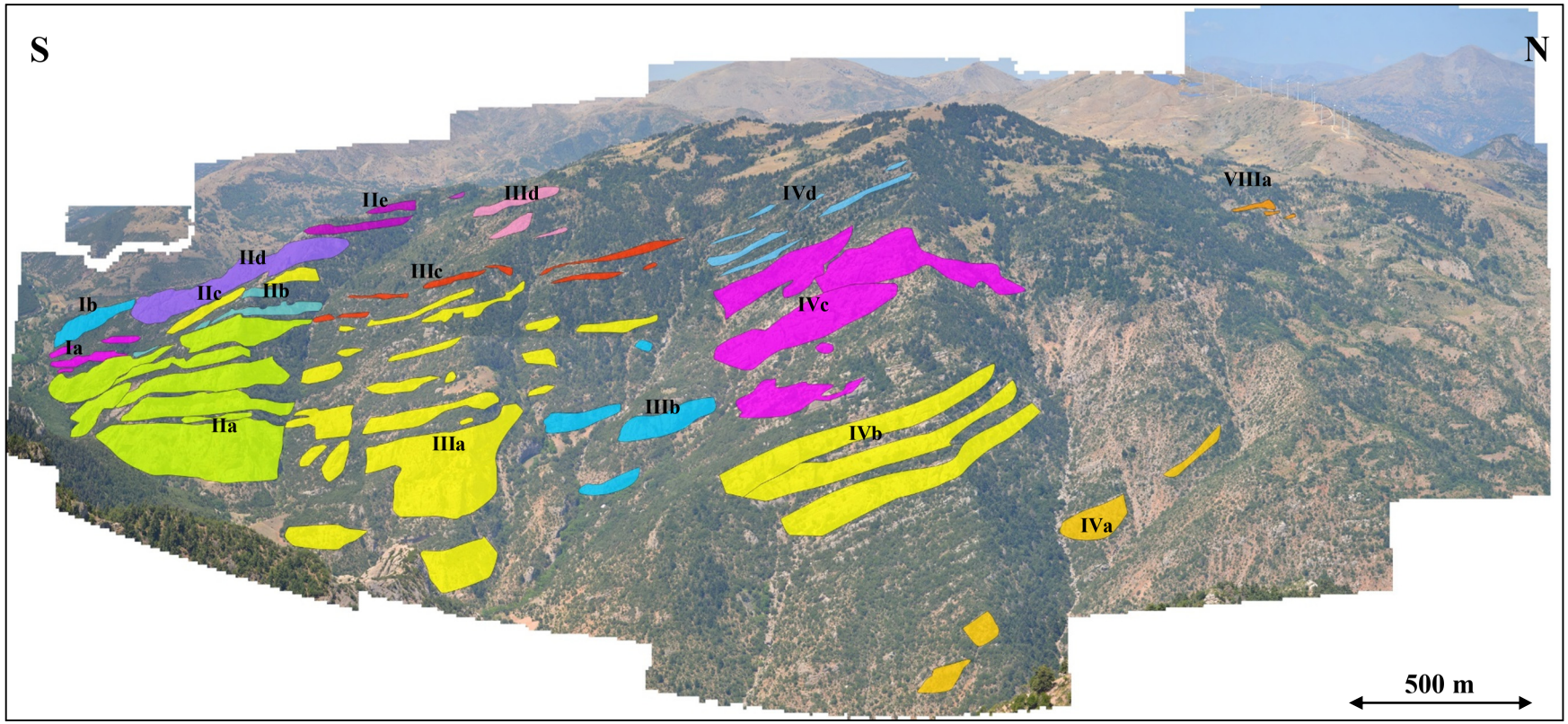

Figure 46 Overview of all of the different layer groups defined for the eastern profile of Roghi Mountain.

Layer Group	Dip and Dip Direction	Remarks	Thickness Analysis
Ia	22° / 240-225°	Poorly constrained top and base of beds.	Slight increase in thickness towards the north-west in layer Ia2.
Ib	N/A	Thick chaotic unit.	N/A
IIa	20° / 228°	Thickest conglomerate beds observed in Roghi Mountain.	IIa7 exhibits a significant increase in thickness towards the south-east.
IIb	25° / 218°	Anomalous dip angle.	N/A
IIc	N/A	Appears as a continuous bed with uncertain geometries.	N/A
IId	N/A	Thick chaotic unit	N/A
IIe	16° / 210-220°	Thinner beds than most others within Segment II.	N/A
IIIa	20° / 228°	Thick conglomeratic units in the southern part of Segment III.	N/A
IIIb	N/A	Poorly exposed beds, might not be in-situ.	N/A
IIIc	18° / 240°	Thin beds with limited exposure.	N/A
IIId	16° / 220°	Uppermost beds of Segment III.	N/A
IVa	30° / 220°	Slightly darker coloured beds than rest of Segment IV.	N/A
IVb	25° / 220°	Truncating suddenly towards the south.	Increased thickness towards the south-east for layer IVb2.
IVc	N/A	Chaotic beds.	N/A
IVd	25° / 195°	Relatively thin beds.	N/A
Va	35° / 130°	Very limited exposure, causing high uncertainty in bed geometries. Especially for dip direction.	N/A

Table 1 Summary of some key features described for the layer groups on the eastern profile of Roghi Mountain.

4.4 Western Profile

Roughly two kilometres west of the Vourikos River the western profile of Roghi Mountain is defined. This is much more vegetated than the eastern side of Roghi Mountain, and roughly 500 m shorter in the north-south direction, the topographic relief of the western profile exceeds 400 meters. This difference in length and relief causes the western profile to have less exposure compared to the eastern. Yet, this side can be divided in three segments with quite distinct individual features in each segment. Spurs separate these segments as well, yet these spurs are not as well defined as some of the spurs on the eastern profile.

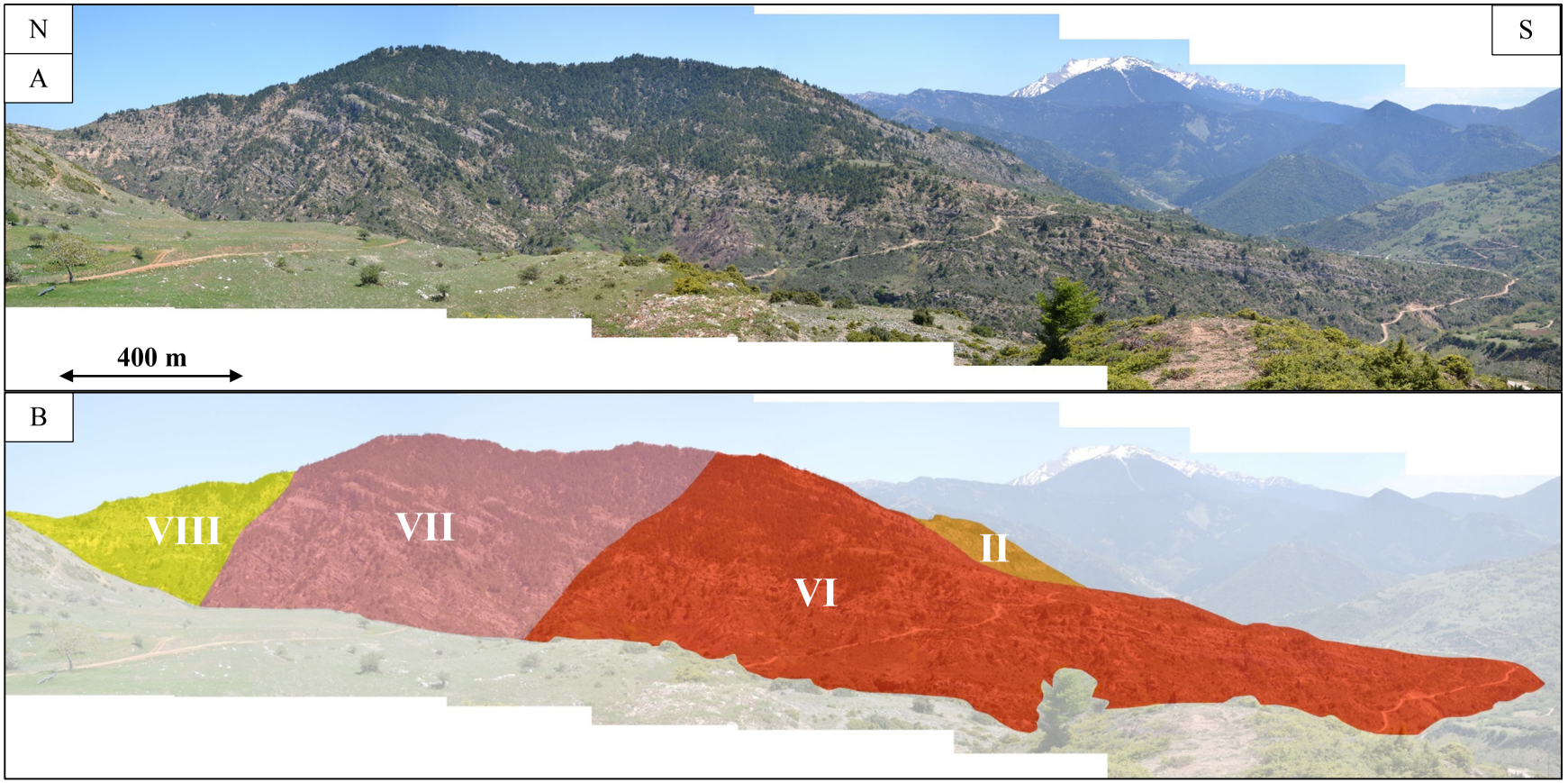

Figure 47 A) Photograph of the western profile of Roghi Mountain. B) Segment division of western profile of Roghi Mountain, map view of segments visible in Figure 20

4.4.1 Segment VI

The topography of Segment VI is different compared most of the other segments of Roghi Mountain. Typically, the segments have a quite extensive vertical succession of visible layers, this is not the case for Segment VI. This segment has layers that extend much further north-south than anywhere else, but the vertical succession of these layers is very limited. Two layer groups have been defined in Segment VI (Figure 48) which both exhibit quite similar features.

Layer group VIa (Figure 48) is composed of interchanging layers of conglomerate, sandstone and shales (Figure 49). The colour of these beds is generally a darker brown than the typical light brown to white colour shading. Clast sizes are on average pebble size. Maximum thickness of any individual bed within layer group VIa does not exceed 8 m. Layer group VIa is exposed for 1 km in the north-south direction, although the layer character does not allow for a single layer to be followed across this entire distance. The dip angle of layer group VIa was measured to 15° and the dip direction is almost directly southwards (185°) (Figure 50).

Beds of layer group VIb (Figure 48) are thicker compared to the layer group Iva beds, and the layers are more conglomeratic with a lesser frequency of shale and sandstone layers. Clast sizes (on average) vary between cobble to boulder size. This layer group has a lighter brown to white colour shading of the beds compared to IVa. The dip direction shift slightly south-eastward moving up the vertical succession of layer group VIB (at the top 215°), the dip angle remains more or less the same as for layer group VIa.

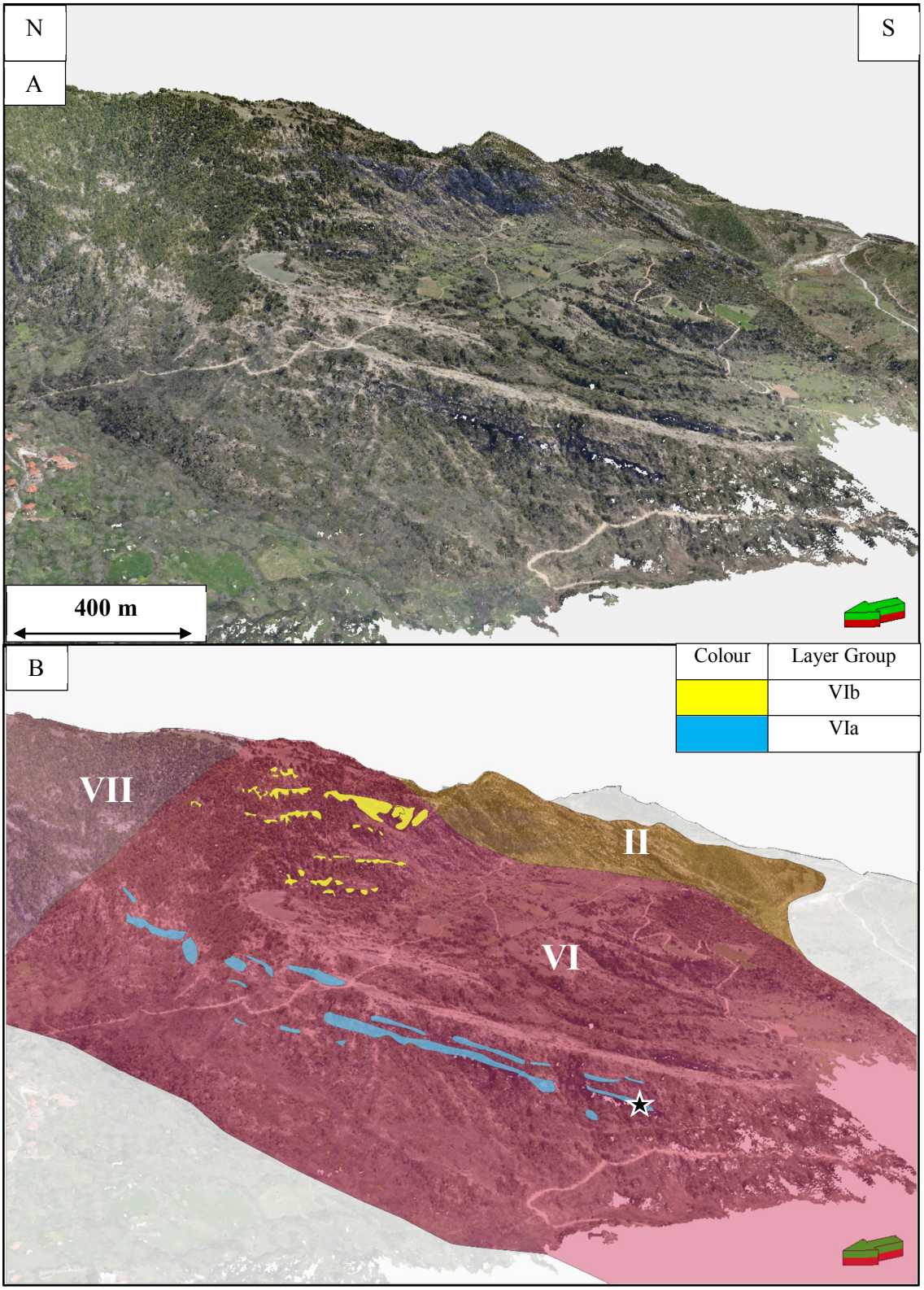

Figure 48 (A) LiDAR point cloud visualization of Segment VI. (B) Traced and grouped layers highlighted with bounding segments visible, segment number in white letters. Black star indicating location of outcrop in Figure 49. Location of segments visible in Figure 20 and Figure 47.

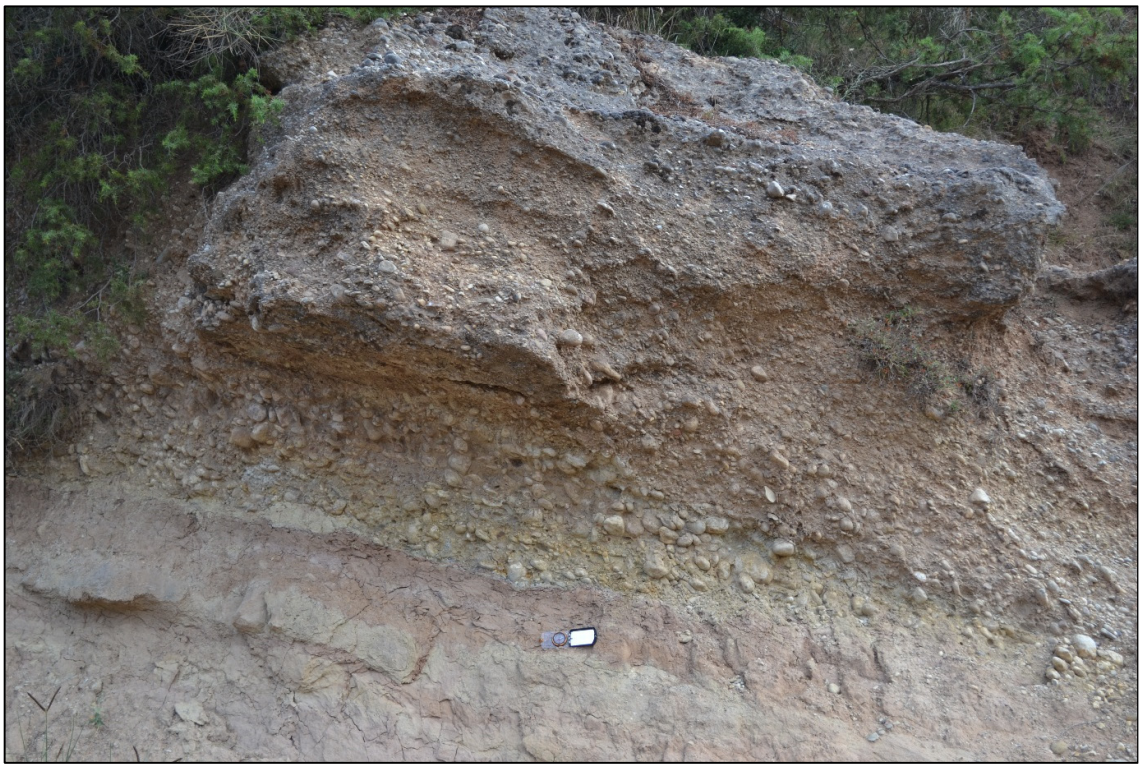

Figure 49 Photograph from outcrop marked in Figure 48. Outcrop exhibits rapid changes from relatively low energy environments such as sandstones an in some areas (not in photograph) shale, to high energy conglomerate deposits. This is very different from the typical conglomeratic beds found across Roghi Mountain (Figure 18 and Figure 27).

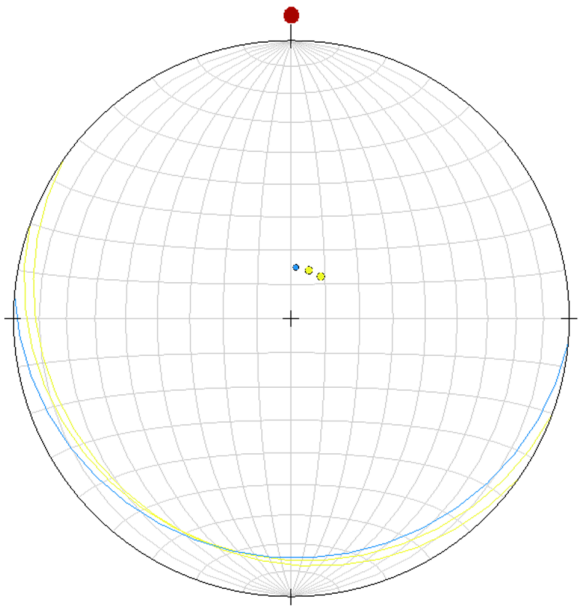

Layers	Dip Dir	Dip
VIb	200-215	15
VIa	185	15

Figure 50 Stereonet with the planes constructed for the of the layer groups of Segment VI. Planes and poles marked according to layer groups in the small table.

Between layer groups VIa and VIb in Figure 48 there is a quite extensive semi-flat area (highlighted in Figure 51). This semi-flat area is dipping towards a small river valley at the southern side of Roghi Mountain. Combined with the observation that very little of the vertical succession of layer unit VIa appears to be preserved, this semi-flat area could be an indication of substantial recent erosion.

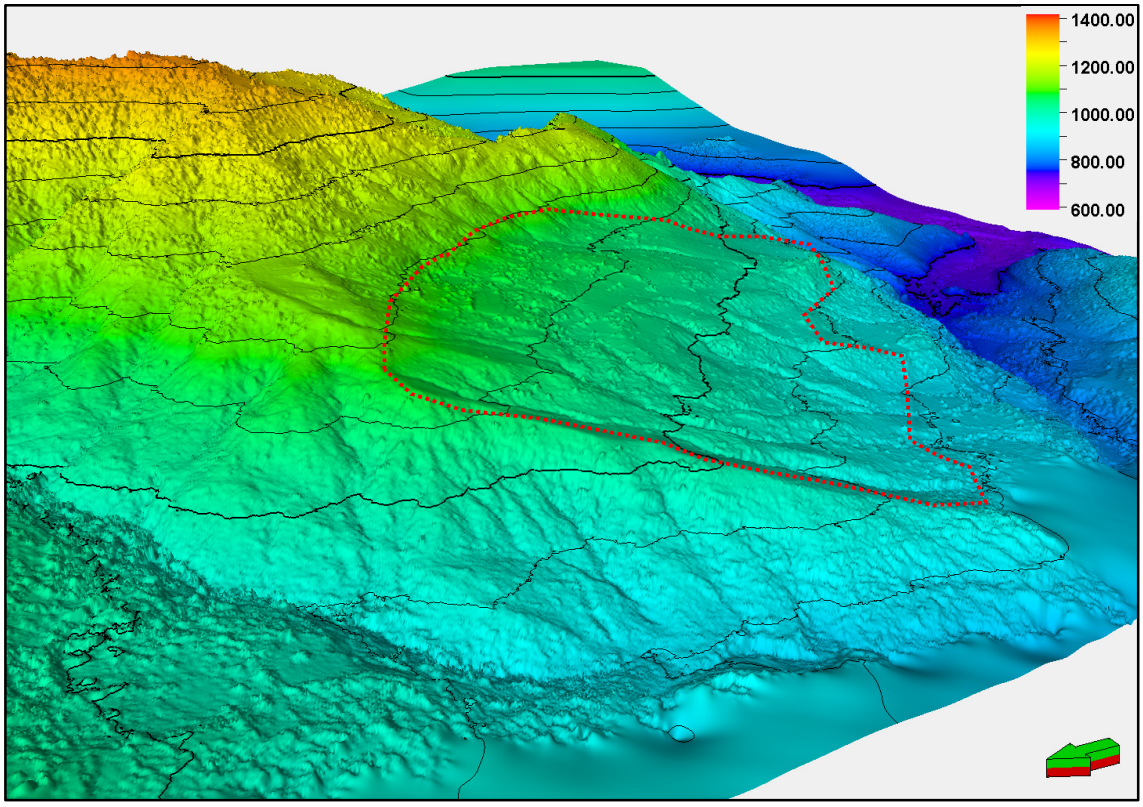

Figure 51 Display of surface generated from LiDAR point cloud with elevation contours and colour scheme (legend in m). This figure has the same view as in Figure 48.. Red dashed polygon represents semi-flat area of Segment VI.

4.4.2 Segment VII

The southern boundary of this segment is defined, as most of the other segments, by a distinct spur in Roghi Mountain and what appears to be a slight change in dip between beds of Segment VI and VII. Segment VII (Figure 52) is heavily vegetated and the layers are not as clear as in other segments on the eastern side of Roghi Mountain. The topographic relief of Segment VII is more than 400m, therefore an extensive vertical succession of layers is visible in this area. The colour of the layers of this segment display a light brown to white colour shading which is typical for most of the thick conglomeratic beds of Roghi Mountain. Clast sizes (on average) vary between cobble to boulder size.

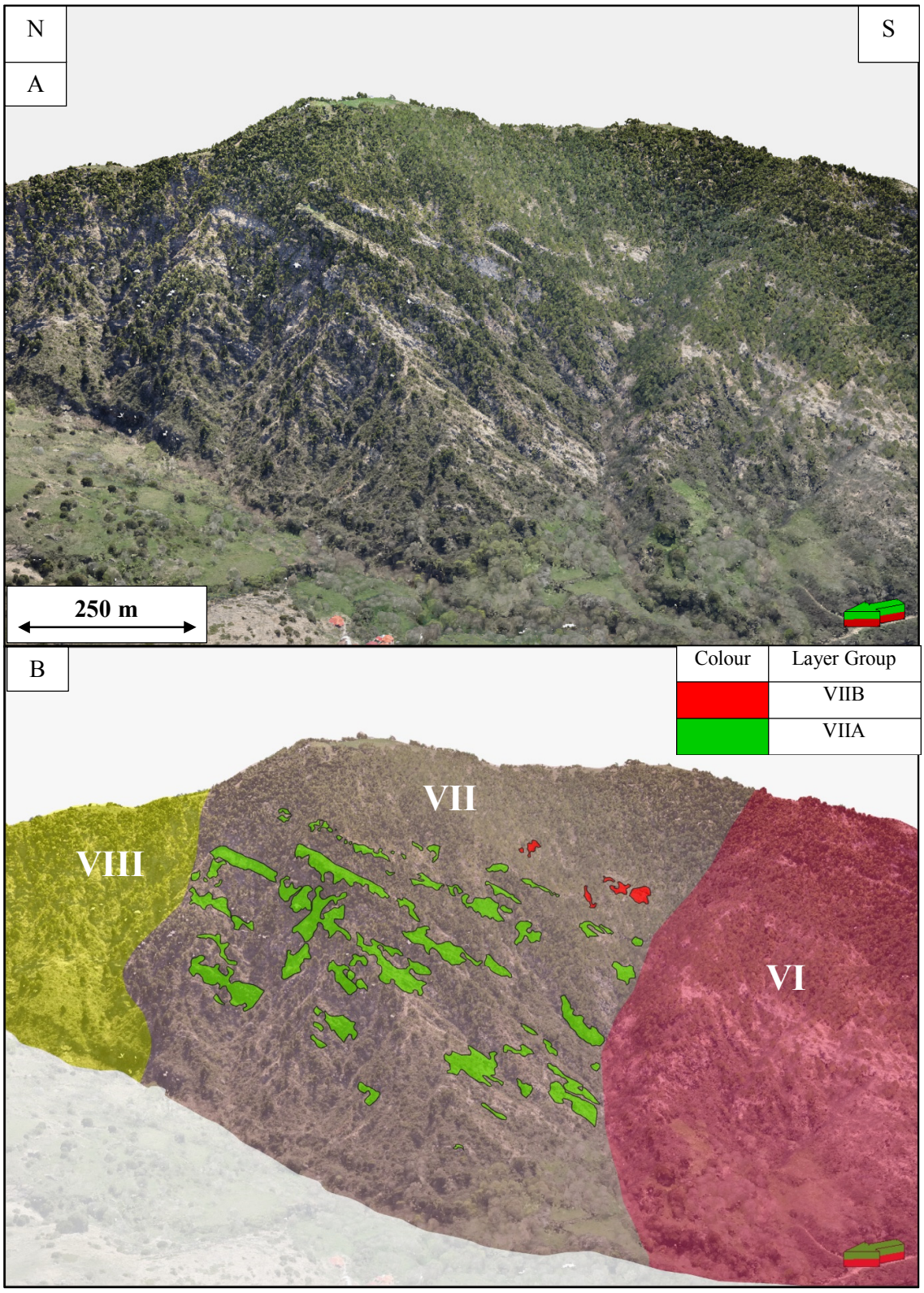

Figure 52 (A) LiDAR point cloud visualization with focus on Segment VII. (B) Traced layers coloured after their assigned groups, segments marked with white letters. Location of segments visible in Figure 20 and Figure 47.

In Figure 52 two layer groups have been defined, however the nature of the outcrops in segment VII in regards to the heavy vegetation make it difficult to study any single layer over any distance.

Layer group VIIa (Figure 52) is not very well exposed and appears quite weathered in some sections. The beds of layer group VIIa appear to have a constant dip angle of ca 23-25°, and a dip direction of 185-195°.

Field observations suggest that there is a lot of unconsolidated material, especially at the lower sections, across Segment VII. This is an indicator that there is a high frequency of finer grained layers in between thicker conglomeratic layers. The lithology of these layers could not be determined because of the resolution of the LiDAR and the inaccessibility to these areas during fieldwork (steep cliffs).

Layer group VIIb (Figure 52) could have the same bed geometries as layer group VIIa, however, these beds are so poorly exposed it is hard to describe these beds properly. Therefore, layer group VIIb is depicted separately from layer group VIIa as the dip and dip direction cannot be concluded with the adequate confidence to make it a solid observation.

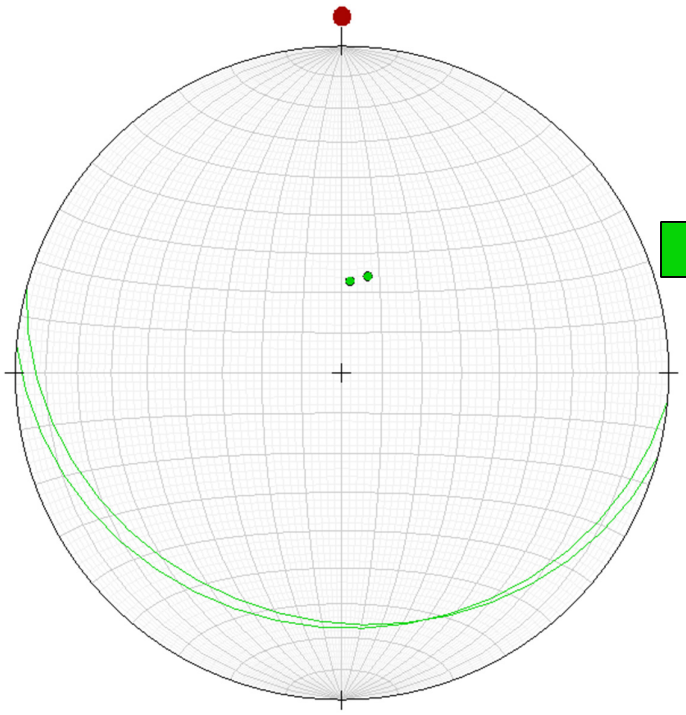

Layers	Dip Dir	Dip
VIIa	185-195	23-25

Figure 53 Stereonet with the planes constructed for the layer group of Segment VII. Planes and poles marked according to layer group in the small table.

4.4.3 Segment VIII

When viewing the western profile (Figure 47), this segment is limited to the south by yet another spur in the mountain side. Looking across from Segment VII to VIII there is a significant change in character of the outcropping layers. Segment VIII is also the only segment that has an outcrop visible both on the eastern and western sides. The reason that these layers have been correlated across the eastern and western profiles is because of the layer similarities, and anomalous low dip angle, dip direction as well as the close proximity between the two outcrops.

Only one layer group has been defined for this segment (VIIIa in Figure 54 and Figure 55) as there has not been observed significant variation in the beds of this segment to further sub-divide these beds. The beds of layer group VIIIa are relatively thin, with no individual layer exceeding 6 m in thickness. Beds of layer group VIIIa exhibits a brown to dark brown colour shading. Many of the beds of layer group VIIIa (Figure 54 and Figure 55) are sandstone layers, with some shale intervals (visible in Figure 19). The conglomeratic layers observed within layer group VIIIa contained no clasts over cobble size, most beds were pebble size or smaller. Because of this decrease in clast size, the lithological observations made within this segment define the area of Segment VIII as a separate unit in Figure 16 as Group 3. Between the beds of layer group VIIIa (Figure 54 and Figure 55) finer grained layers are expected, but these are very poorly exposed.

The outcrop of this segment that is visible on the eastern side (Figure 55) of Roghi Mountain have some features dissimilar from the outcrop on the western side (Figure 54). On the eastern side, three layers are quite distinct while on the western side the layers are a bit harder to separate from each other and there seems to be at least fifteen layers visible. This is most likely caused by the difference in vertical exposure between the two profiles. Another possibility is that here is a change in the depositional character of this unit from the western outcrop in relation to the eastern.

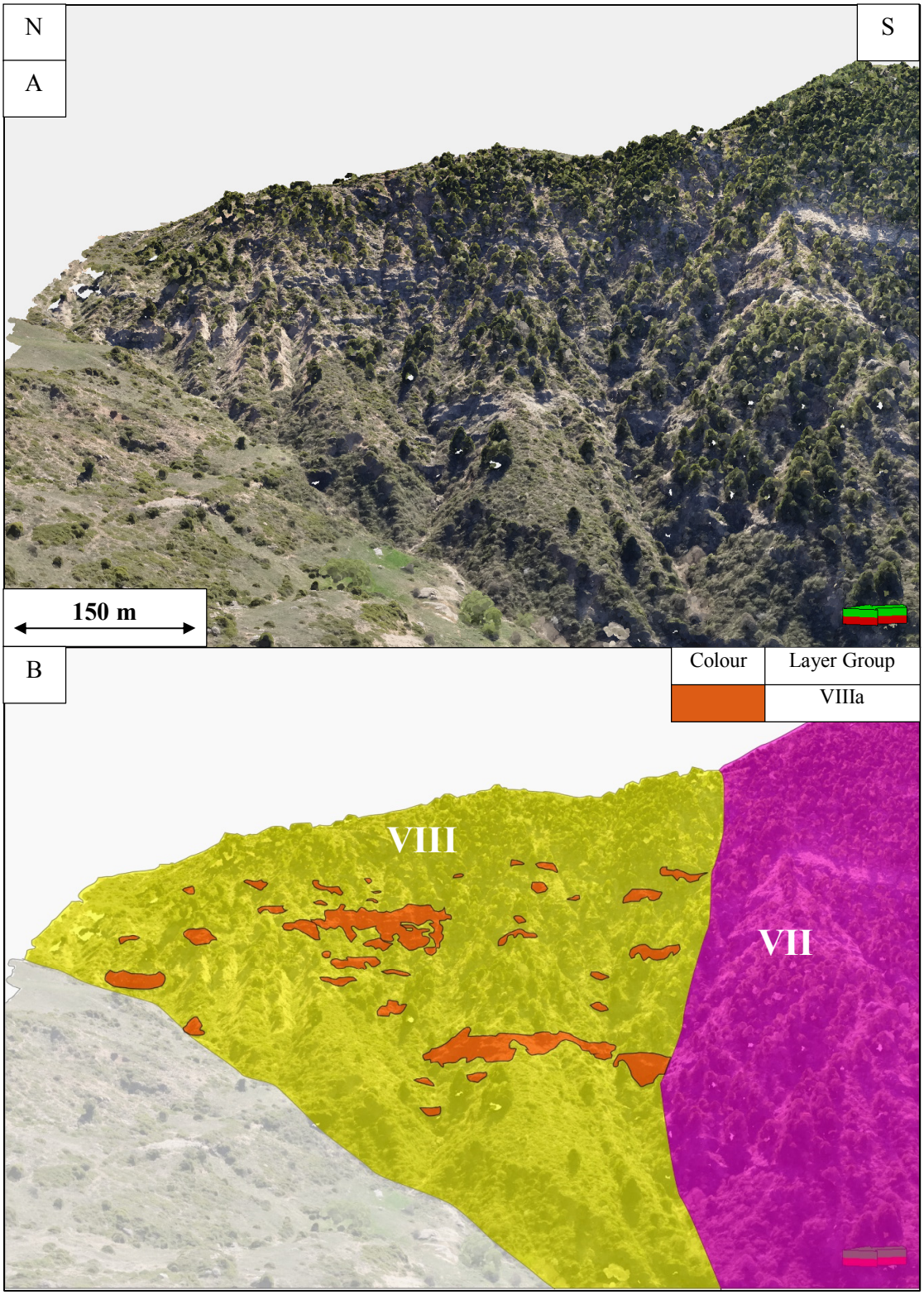

Figure 54 (A) LiDAR point cloud visualization of western part of Segment VIII. (B) Layer traces marked and segments marked with white letters. Location of segments visible in Figure 20 and Figure 47

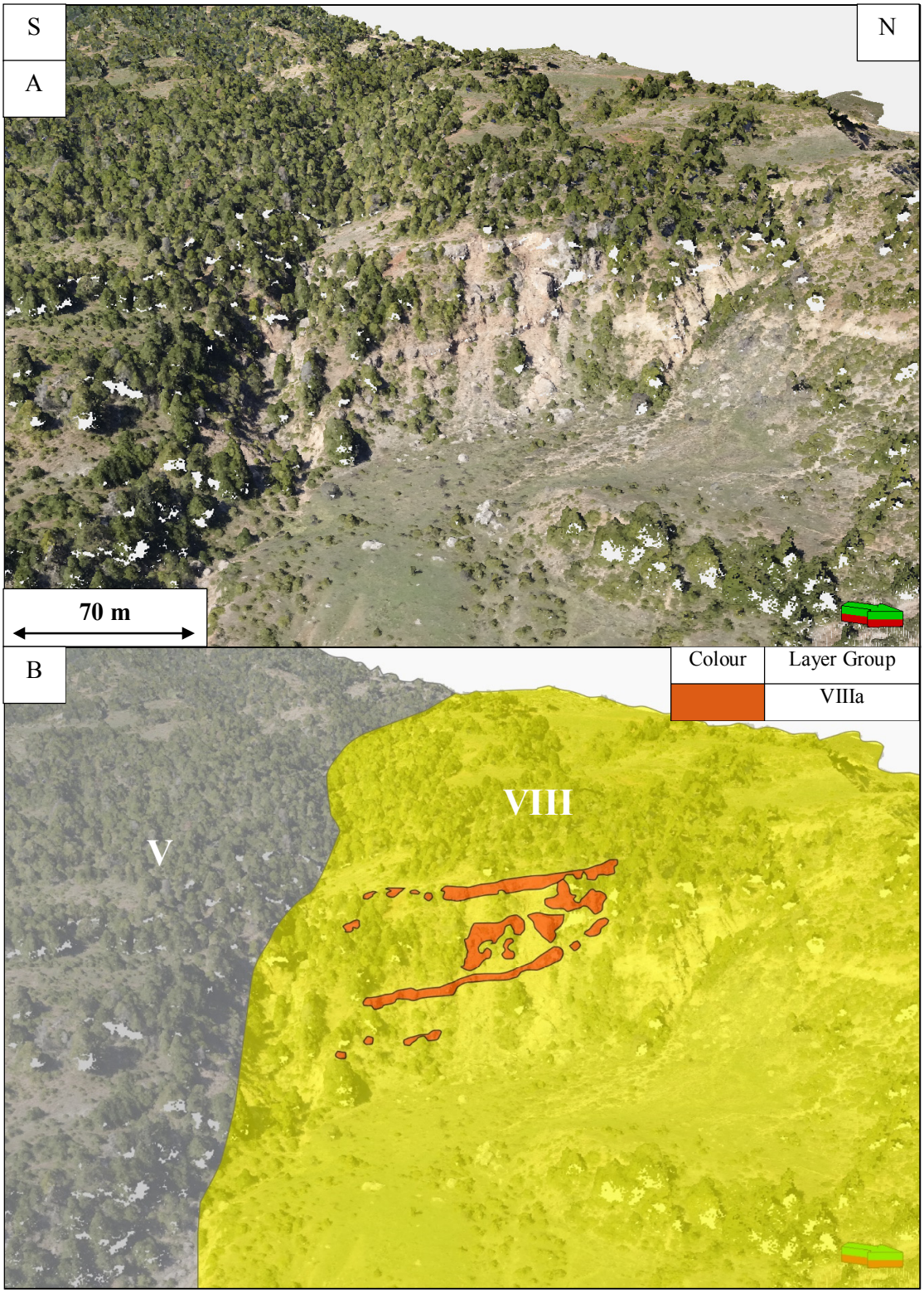

Figure 55 (A) LiDAR point cloud visualization of eastern part of Segment VIII. (B) Layer traces marked and segments marked with white letters. Location of segments visible in Figure 20 and Figure 47

What distinguishes this segment from the other segments of Roghi Mountain is the dip and dip direction of the layers. Measuring directly on the surfaces of the individual layers in the field proved very challenging, as the nature of these beds were very uneven. The minor thickness variations occurring along all layers are assumed to be related to depositional dips. Estimation of dip and dip direction of these layers in the field was roughly 10-15° and 130°, respectively. Planes generated from layer tracing of the LiDAR data suggest a dip direction of 105-110° and a dip angle of 10° (represented in Figure 56). This is a dramatic change in dip direction from most other layers in Roghi Mountain.

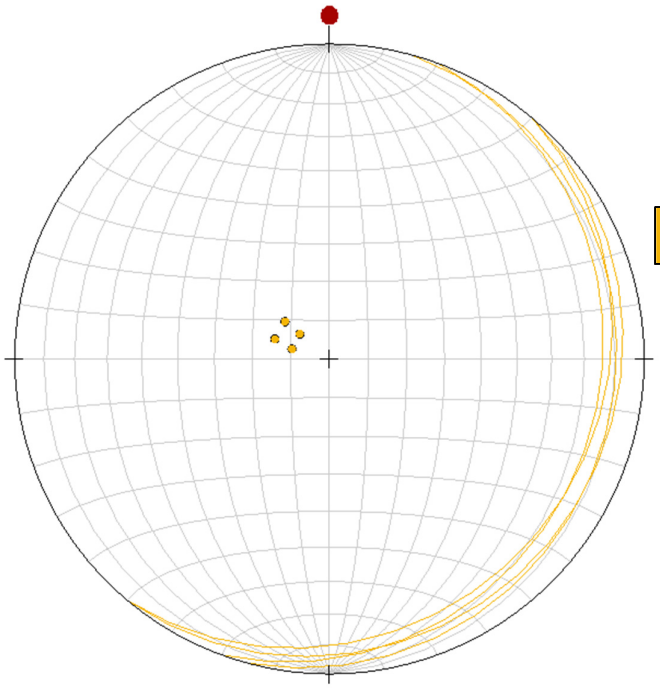

Layers	Dip Dir	Dip
VIIIa	105-130	10-15

Figure 56 Stereonet with the planes constructed the layer group of Segment VIII. Planes and poles marked according to layer group in the small table.

Summary of Western Profile

The five different layer groups defined for the western profile of Roghi Mountain are all marked in Figure 57. Table 2 exhibits a summary of some key features observed for the layer groups on the eastern profile.

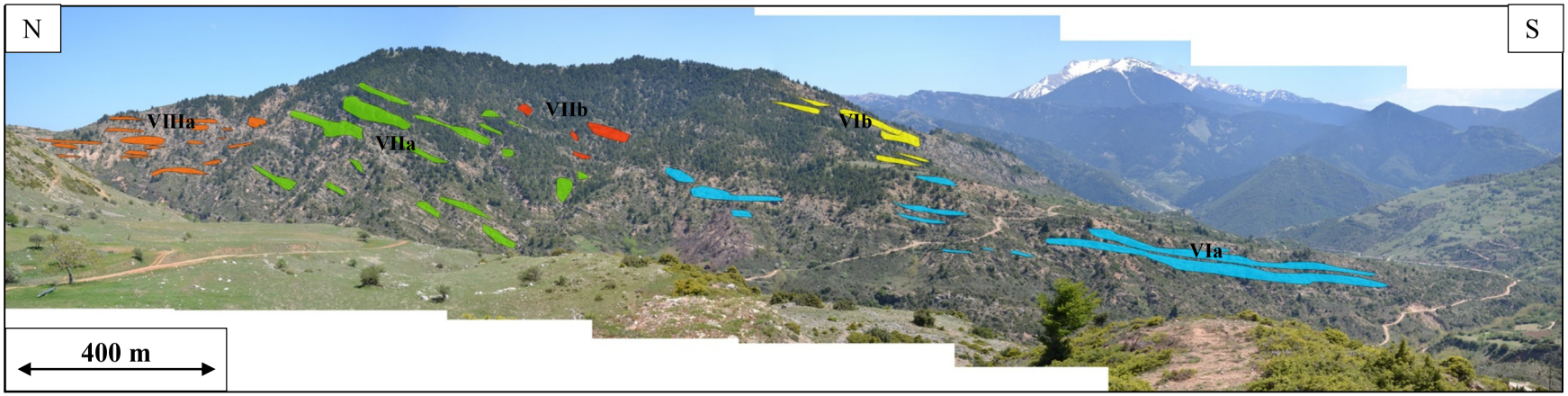

Figure 57 Overview of all of the different layer groups defined for the western profile of Roghi Mountain.

Layer Group	Dip and Dip Direction	Remarks
VIa	15° / 185°	Thin layers with interchanging beds of sandstone, shale and conglomerates. Different colour compared to other layers in Segment VI.
VIb	15° / 200-215°	Relatively poor exposure, no bed exceeding 8 m in thickness.
VIIa	23-25° / 185-195°	Extensive vertical outcrop exposure, no changes in dip direction upwards in the bed succession. .
VIIb	N/A	Very limited bed exposure.
VIIIa	10-15° / 105-130°	Defined as Group 3 in Chapter 3.

Table 2 Summary of key features described for the layer groups on the western profile of Roghi Mountain.

Chapter 5: Interpretations and Correlations

The purpose of this chapter is to "integrate" each of the geological units (within the segments described in Chapter 4) and determine what can be correlated across the mountain (between eastern and western profile), which stratigraphic sequences can be linked together, and what are the main structural elements within Roghi Mountain.

5.1 Faults

Most faults in the northern part of the Peloponnese peninsula are normal faults (Collier and Jones, 2004; Ford et al., 2013), which is expected for rift systems. Some of the faults of the area can be traced with near absolute certainty from lithological contacts, while others can be interpreted based on angular relationships between layers or they can be inferred based on geological consistency issues.

Internal faults in the Roghi Mountain outcrop is challenging to derive two main reasons.

A. As made apparent from Chapter 4, thickness variations along layers in both north-south and along east-west direction complicate layer tracing even over a relatively short distance.
B. There are no clear graben wide markers, such as distinct layers or sudden lithological variations other than what could be expected for alluvial/fluvial deposits.

Figure 59 displays the faults incorporated in this study.

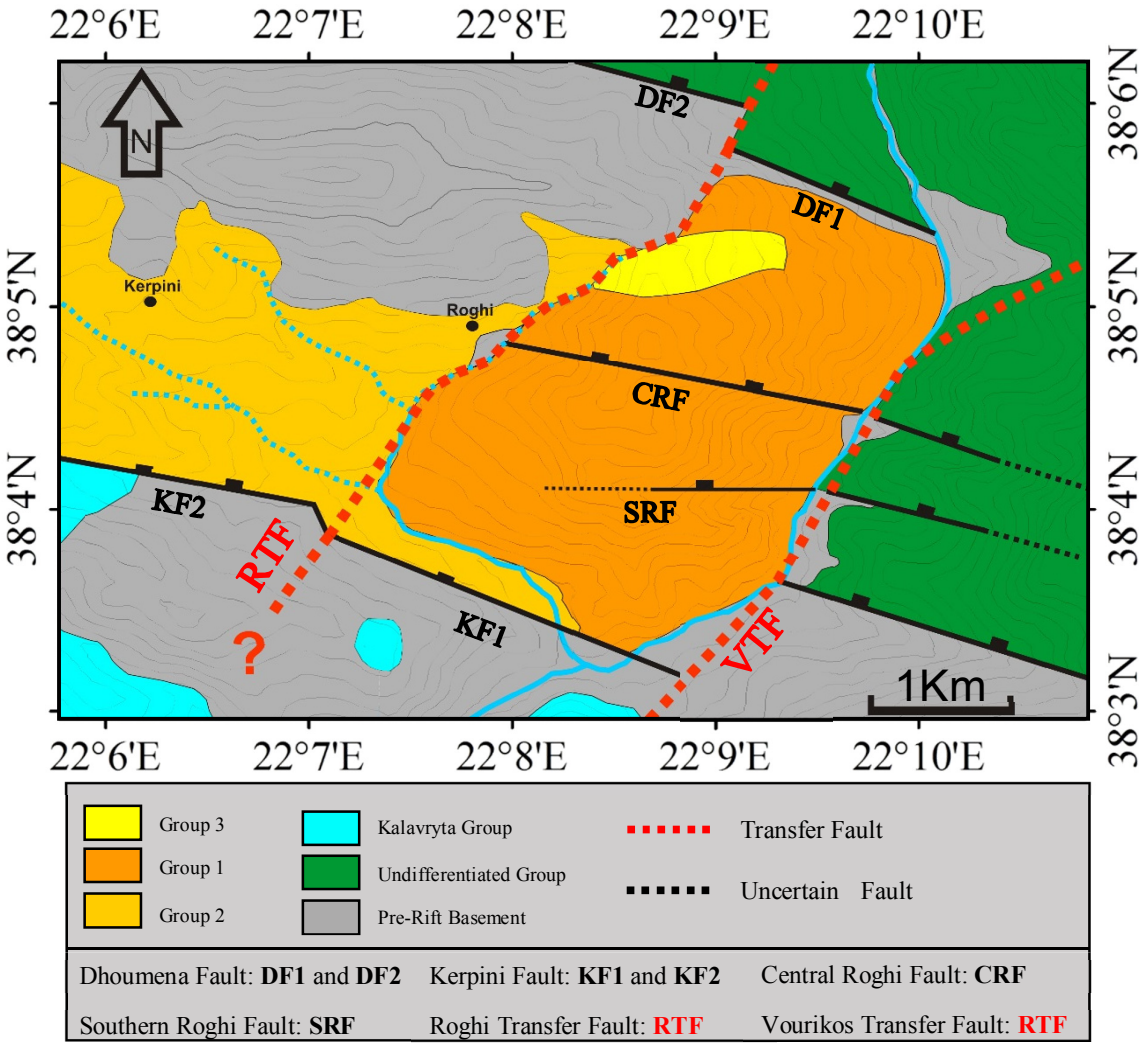

Figure 59 Lithological map of study area with the faults incorporated in the study marked.

5.1.1 Kerpini Fault

The Kerpini Fault is defined as one of the fault block bounding faults. It is not clearly visible in the LiDAR dataset, but this fault could be traced during fieldwork as there is a basement/sediment contact on the southern side of Roghi Mountain (Figure 23).The fault trace interpretation agrees with previous work (Collier and Jones, 2004; Dahman, 2015; Ford et al., 2013; Syahrul, 2014). The Kerpini Fault has been interpreted to consist of two parts. This division was defined because of a small northward step in the fault, the Kerpini Fault is therefore divide in KF1 and KF2 (Figure 59). KF1 was interpreted strike 119°, and the KF2 115°, while the dip angle could not be measured directly but is assumed to be 40° for both

segments, this is based on the dip angle of similar faults previously mapped in the area (Dahman, 2015; Ford et al., 2013). The displacement of the fault was calculated by projecting the unconformity surfaces in the hanging wall and in the footwall of the fault, and using simple trigonometry (Figure 61). The faults are assumed to have dip slip displacement (Ford et al., 2013).

The basement outcrop in Segment III was used for projecting the unconformity surfaces of the hanging wall of the Kerpini Fault, and a dip of angle of 22° was measured for the unconformity. The same dip angle was assigned for the projection of the unconformity in the footwall of the Kerpini Fault, although this is less certain. The displacement for the KF1 was calculated to ca 1600 m.

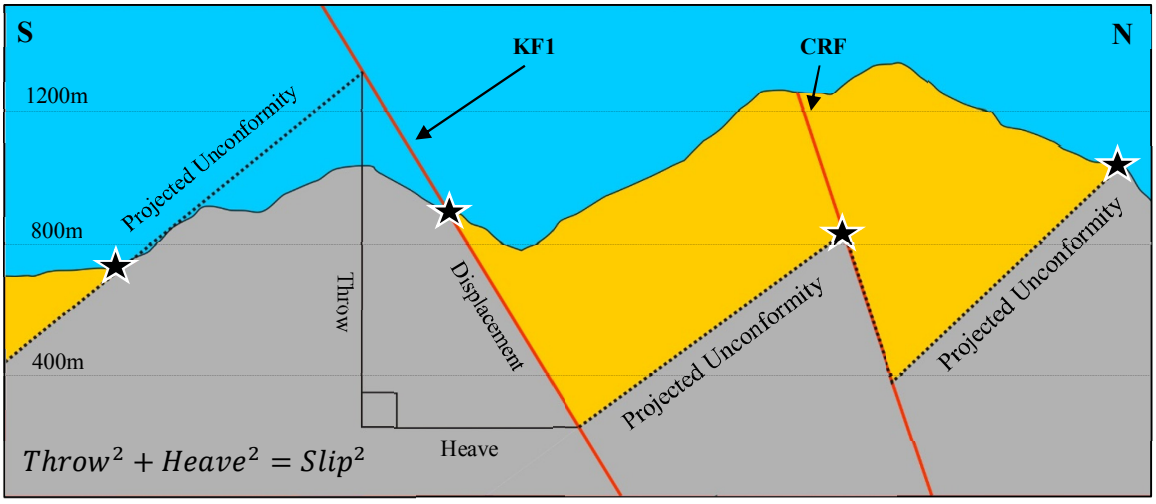

Figure 61 Example of how the displacement of faults were calculated. The black stars represent exposed basement outcrops which unconformities were projected from. Elevation relative to sea level.

5.1.2 Dhoumena Fault

Defined as the northern fault block bounding fault, the Dhoumena Fault interpretation agrees with Syahrul (2014) where the fault is divided in two segments. Both segments, DF1 and DF2 dip 48°, and strike 110°. These two fault segments are assumed to be hard linked by the Roghi Transfer Fault (RTF in Figure 59) as interpreted by Syahrul (2014) and Dahman (2015). The displacement for DF1 was estimated by Dahman (2015) to 1200 m.

5.1.3 Central Roghi Fault

Along the eastern Roghi Mountain profile the basement/sediment contact close to the Vourikos River and higher up, as well as the distinct change in outcrop characteristics observed between Segment III and IV, strongly indicate the presence of a fault. On the western profile this fault is interpreted to be present between Segment VI and VII, where there is a clear dip change

between the beds of the two segment. By correlating these contacts and placing a fault plane between them, the fault plane has a strike of 112°, and a dip angle of 56°.

There are however two possibilities for the interpretation in regards to the geometries of the CRF:

1) The fault continues through to the top of the sedimentary succession of Roghi Mountain (Dahman, 2015; Syahrul, 2014).
2) The fault is eroded and unconformably overlain by a distinctively younger sequences of sediments deposited after the final movements of the CRF.

This is uncertain due to the limited bed exposure near the top of Roghi Mountain (marked with blue rectangles in Figure 62 and Figure 63).

To estimate the displacement of the CRF (Figure 62 and Figure 63), the unconformity visible in Segment V was projected towards the CRF fault plane. The dip angle of the unconformity at the outcrop in Segment V is 35°, this is based on the dip of the overlying sediments. The displacement of the CRF is estimated to 750 m at the eastern profile of Roghi Mountain (at the basement outcrop in Figure 62), and decreasing towards the east to 450 m at the western profile (Figure 63).

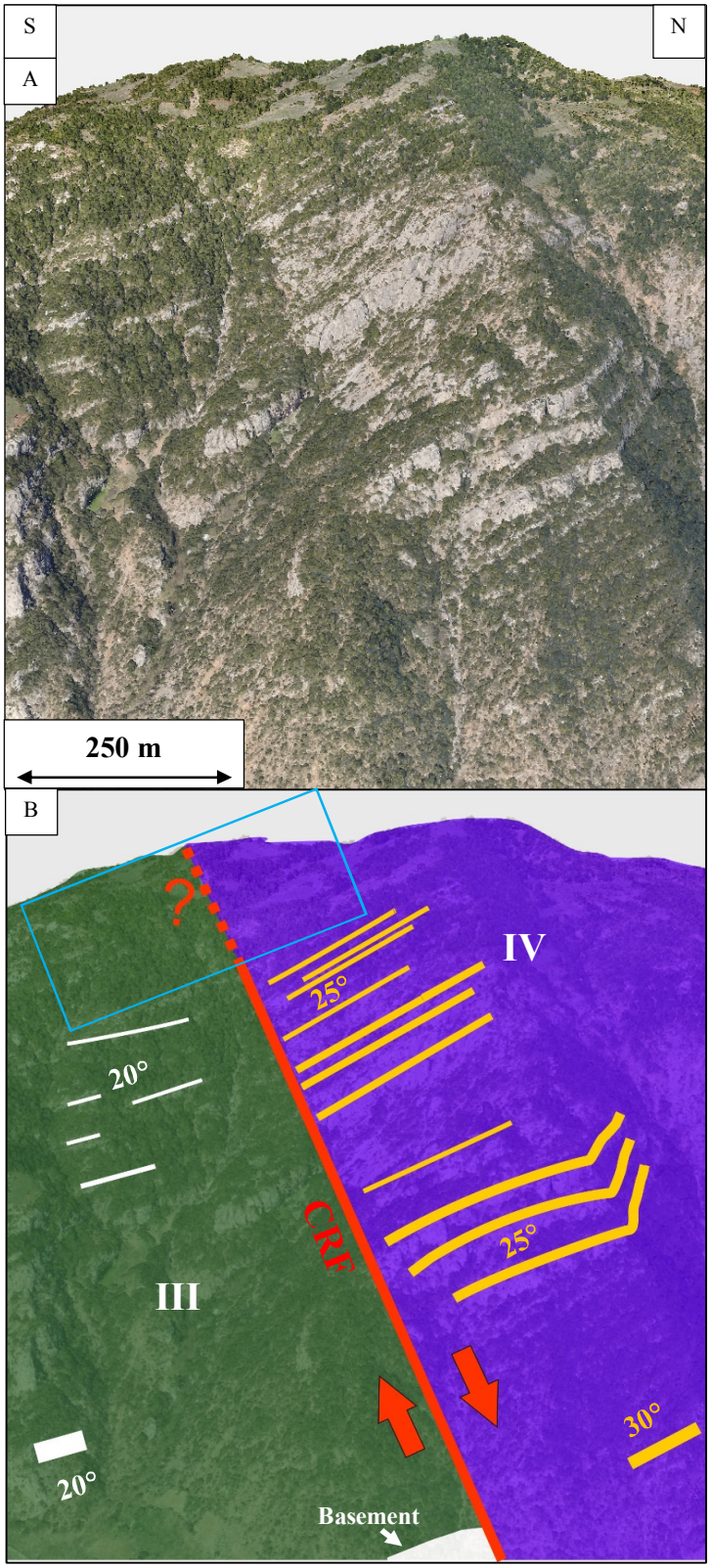

Figure 62 A) LiDAR representation of eastern profile. B) Interpretation of CRF. Within the blue rectangle no beds are visible on either side of the fault. This could indicate that the CRF does not carry on through the entire vertical succession. The segment locations displayed in this figure is visible in Figure 20 and 22.

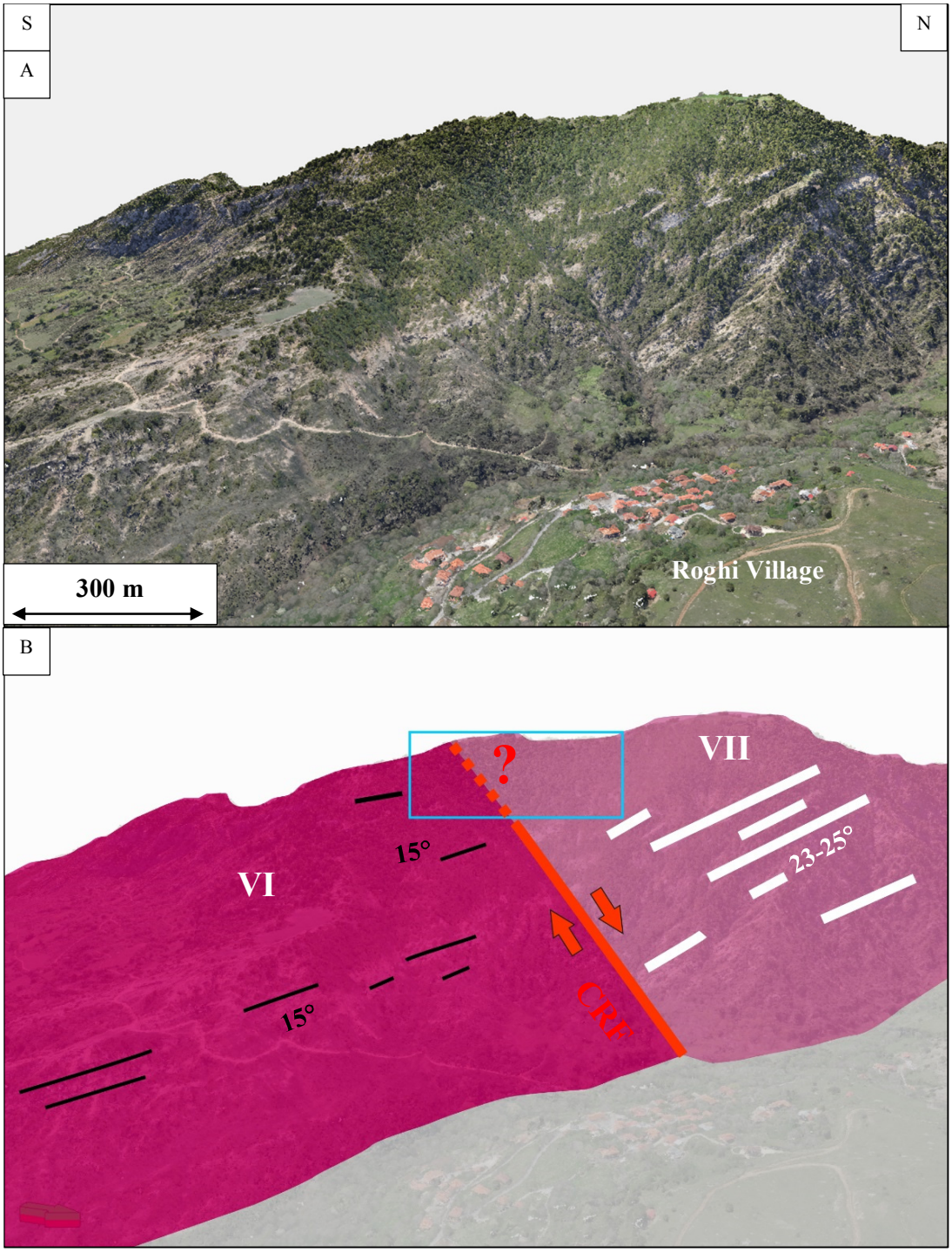

Figure 63 A) LiDAR representation of western profile of Roghi Mountain. B) Interpretation of CRF, within the blue rectangle no beds are visible, creating uncertainty in determining how far the CRF carries on through the vertical succession. Both A) and B) are mirrored such that north is to the right in the figure, this is for easy comparison with Figure 62. The segment locations displayed in this figure is visible in Figure 20 and 47.

5.1.4 Southern Roghi Fault

The SRF (Figure 59) is a relatively small fault within Roghi Mountain with an estimated displacement of only ca 50 m. The fault was identified by observing three distinct layers (Figure 64) that appeared continuous across Segment II and III (correlation between segments described in detail in chapter 5.1). Two observations were made that support the presence of a fault.

1. IIa2 and IIIa2 (Figure 64) has a distinct bed (marked in blue in Figure 64) which could be identified on both sides of the interpreted fault. This bed was considered distinct because it has a thick conglomeratic bed below it, is then "sandwiched" in heavy vegetation, and finally overlain by a second quite massive conglomeratic unit.
2. The thickness of IIa1/IIIa1, IIa2/IIIa2 and IIa3/IIIa3 appears constant across the presumed fault.

The strike of the fault is interpreted to be ca 90° with a dip angle of 70°. With no evidence for this fault on the western profile of Roghi Mountain, the SRF is expected to decrease in displacement towards the west, just as the CRF. Moving up the vertical succession, the fault becomes less obvious. This leaves the two possible interpretations previously discussed for the CRF.

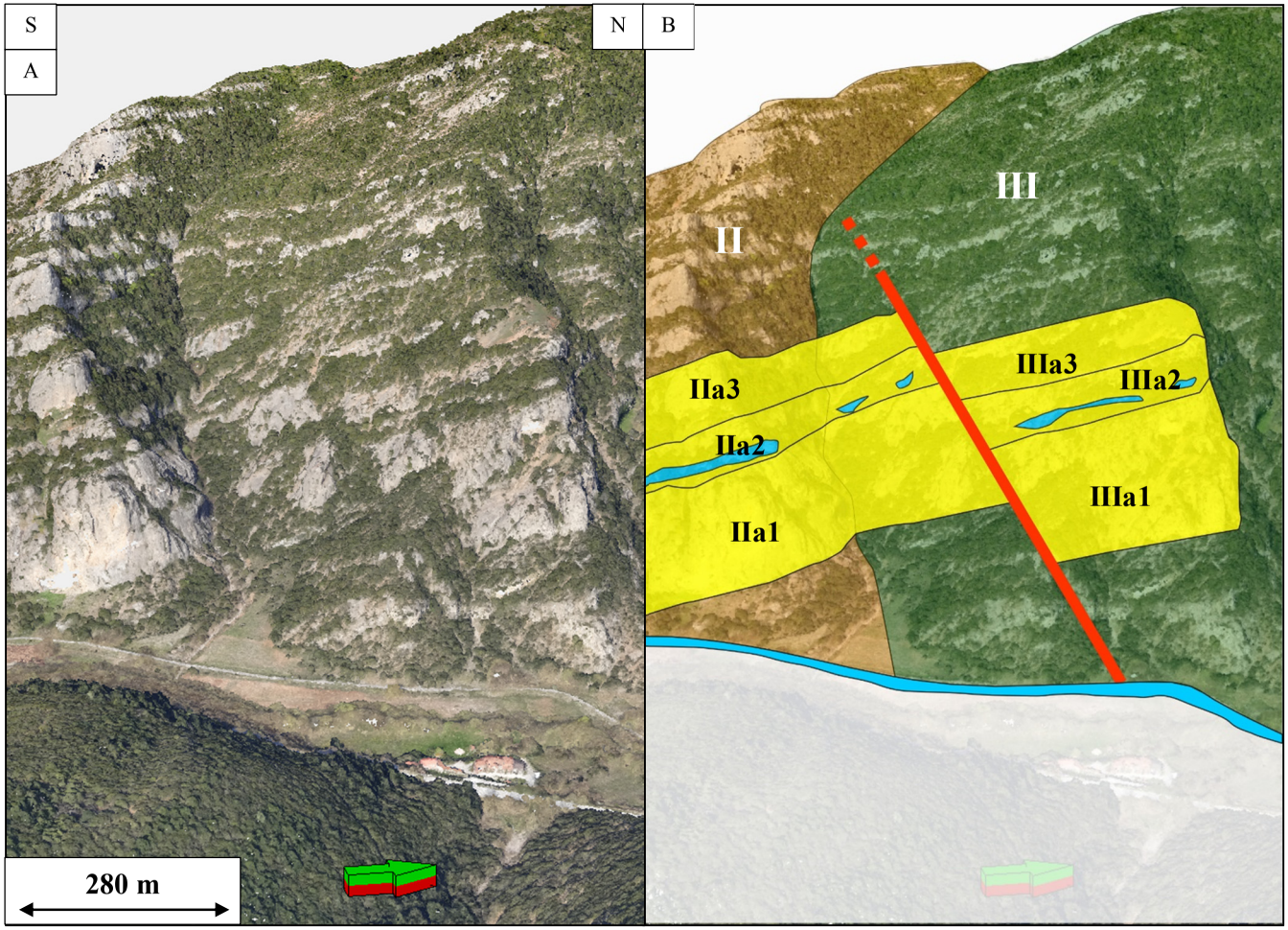

Figure 64 A) LiDAR representation of the eastern profile of Roghi Mountain. B) Interpretatin of the SRF. The segment locations displayed in this figure is visible in Figure 20 and 22.

5.1.5 Roghi Transfer Fault

The RTF (Figure 59) has been inferred to explain the difference in unconformity level between Group 2 and Group 1 (Figure 59) within the Kerpini Fault Block (Syahrul, 2014). Since this fault is not exposed the dip and strike of the fault is uncertain. Syahrul (2014) (supported by Dahman (2015)) suggested a near 90° dip angle and the strike of the fault follows the western profile of Roghi Mountain. The RTF appears to hard link the DF1 and DF2 fault segments and also appears to interact with the step in the Kerpini Fault (in the link between KF1 and KF2). The vertical throw component is estimated to be ca 360 m just north of the CRF, and ca 200 m just south of CRF.

5.1.6 Vourikos Transfer Fault

Following the Vourikos river, the VTF was inferred by Syahrul (2014), and later supported by Dahman (2015). This fault explains the sudden termination (or possible step) of the Kerpini Fault and the difference in unconformity level between the eastern and western side of the Vourikos river.

5.2 Cross Segment Layer Correlation

Observations made for each of the segments in Chapter 4 suggest that many layers share the same characteristics and can be correlated across the different segments. To correlate between the segments discussed in Chapter 4, two main criteria were set to define which layers were to be regarded to be a part of the same depositional sequence.

1. Sequences should be defined by having similar layer geometries (dip and dip direction) and/or other strong correlative indicator such as distinct colour, bed thickness, and thickness variation trends that could indicate facies changes within a depositional sequence.
2. Layers of the same units should be traceable across segment boundaries or the projected planes of the layers should match.

These criteria resulted in the interpretation of five different sequences. Figure 65 and Figure 66 display the various layer groups discussed in Chapter 4. The five interpreted sequences are displayed in Figure 67,Figure 68,Figure 69 and Figure 70.

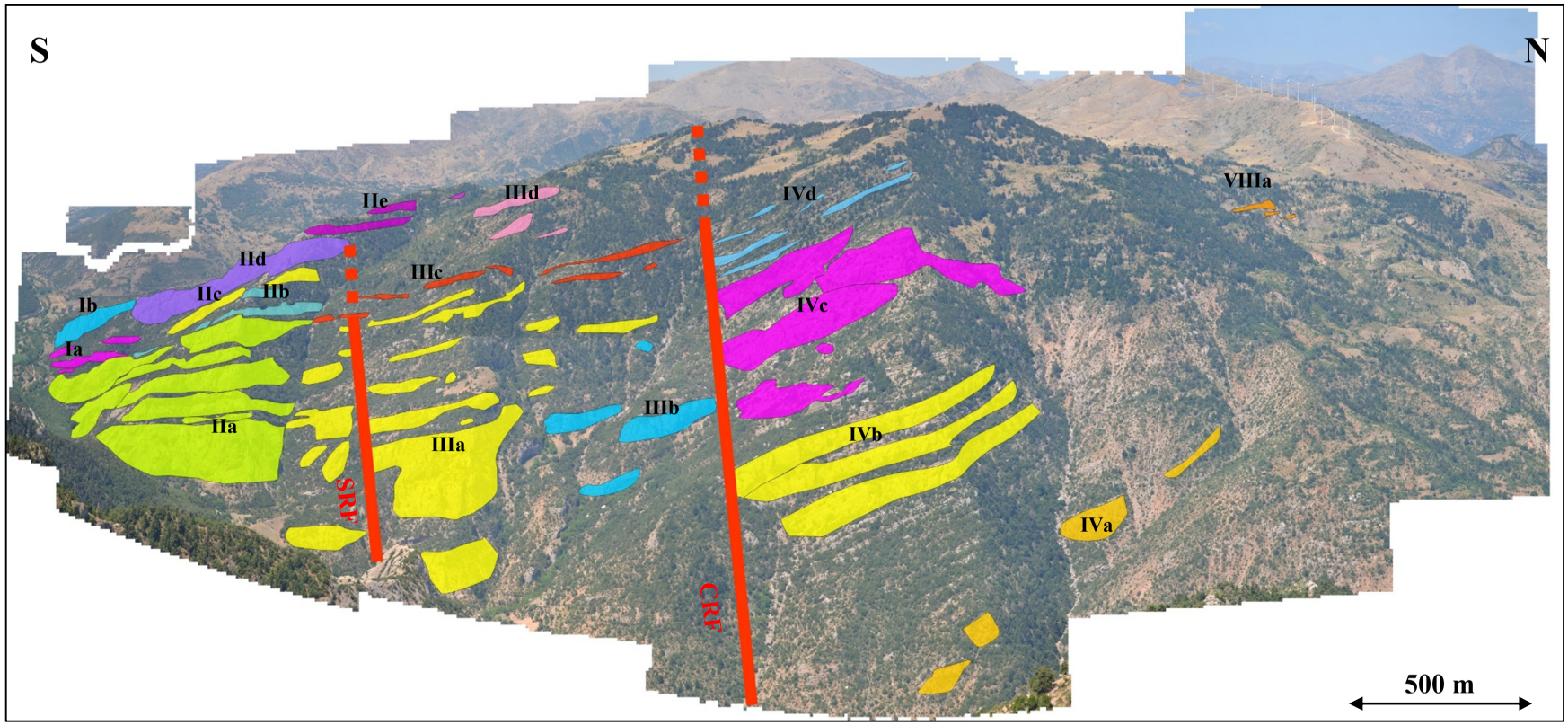

Figure 65 Overview of all of the different layer groups defined for the eastern profile of Roghi Mountain with fault interpretations.

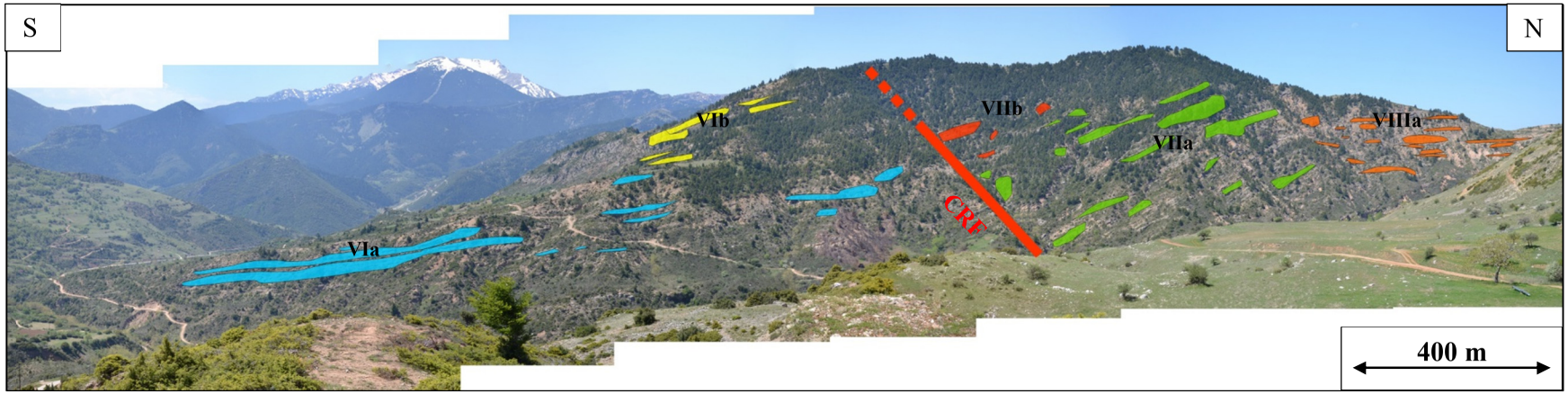

Figure 66 Overview of all of the different layer groups defined for the western profile of Roghi Mountain with fault interpretations. This figure has been mirrored such that north is towards the right. This is done for easy comparison with Figure 65.

5.2.1 Sequence 1

This sequence is divided in a lower and a upper part. The lower part consist of layer group Iva (Figure 65) and Va (not visible in Figure 65 due to perspective of photograph). Both layer groups appear to have, more or less, the same colour and are both estimated to be steeply dipping, which indicates that they were deposited at the same time, and later rotated. Both these layer groups are located north of the CRF.

5.2.1.1 Lower Sequence 1

This sequences consist of layer group IVa and Va. These are the steepest dipping layers observed within the Roghi Mountain outcrops. The outcrops of this sequence is limited, therefore the bed geometries are highly uncertain. Because of the uncertainty related to the bed geometry, layer group IVa and Va have been interpreted to be part of the same sequences due to their similar colour and since they are interpreted to directly overlay the basement north of the CRF.

5.2.1.2 Upper Sequence 1

The upper part of Sequence 1 can be correlated across the mountain from east to west and is composed of the layer groups IVb, IVc, IVd and VIIa (Figure 65 and Figure 66). These layer groups are correlated together because they appear to have the same bed orientation. This is especially evident for layer groups IVd and VIIa where westward projected planes (from IVd) align exactly with beds of layer group VIIa. When projecting layer groups IVa, IVb and IVc through the mountain they do not reach high enough in the elevation on the western profile to outcrop. Discussed earlier in chapter 4.2.4 tracing beds in layer group IVc is challenging, but as both the overlying and underlying layers have a dip angle of 25° it can be assumed that these layers are all part of the same unit.

Correlation of Sequence 1 across the mountain is also based on the interpretation that layer groups (IVa,IVb, IVc, IVd and VIIa) truncate against the CRF (Figure 65 and Figure 66). The beds of Sequence 1 that outcrop on the eastern and western profiles appear slightly different in thickness. This can be explained by that there are facies changes, observed as thickness variations in layer group IVb (Figure 41), occurring in the east-west direction. Between the lower and upper part of Sequence 1 there might be a minor unconformity since there is a 5° dip angle change between these layers. Or, this could be interpreted as evidence for continuous growth strata in Sequence 1.

5.2.2 Sequence 2

This sequences is interpreted to consist of a upper and a lower part.

5.2.2.1 Lower Sequence 2

The lower part consist of layer groups IIa, IIIa and IIIb (Figure 65 and Figure 66). This lower part of Sequence 2 (Figure 68) contain the thickest conglomerate beds visible in Roghi Mountain. The dip and dip direction is more or less the same for these layers across Segment I and II. Layers can be traced across the boundary between Segment II and III and over the SRF, which could explain the minor difference in dip direction between layer groups IIa and IIIa. Layer group IIIb (Figure 65) has also been included as a part of Sequence 1, this is done even though the bed exposure here is poor, yet there is not any evidence for there to be a change in dip angle, dip direction or colour. Therefore, Sequence 1 is interpreted to terminate against the CRF (Figure 68).

5.2.2.2 Upper Sequence 2

The upper part is interpreted to consist of layer group Ia, IIb, IIc and IIIc (Figure 65 and Figure 66). The layer geometries here appear anomalous compared to most other layers of Roghi Mountain which are dipping at a constant angle. Although there is no clear contact or surface visible, these layers could be interpreted to downlap/onlap on a minor erosional surface because of the irregular shape of these layers.

5.2.3 Sequence 3

This unit is only comprised of layer group VIa (Figure 66). These layers have a similar dip angle to that of Sequence 4. However, there are a few characteristics separating the layer groups of these two sequences. Field observations suggest that Sequence 3 layer groups have a high frequency of interchanging shale layers and channelized sandstones within conglomerate layers. This sort of interchanging beds are not visible in the layer groups of Sequence 4. In addition, the dip direction of the layer group of Sequence 3 is almost directly south (185°). This is not the case for layer groups of Sequence 4. Thickness analysis on layer group VIa could not be carried out due to limited bed exposure in the outcrop. No beds with the geometries similar to layer group VIa beds are visible on the eastern profile of Roghi Mountain, therefore this sequences is assumed to pinch out towards the east. The similarities between Sequence 3 and 4 suggest that these sequences are deposited over the same timespan, or at least they conformably overlay each other. However, the distinct variations between shale, channelized

sandstone and conglomerate that is unique for Sequence 3 could suggest that these deposits have a different source than Sequence 1,2, 4 and 5. Alternatively, these could be the distal parts of the alluvial deposits of Sequence 4.

5.2.4 Sequence 4

Covering the upper part of Roghi Mountain (Figure 68 and Figure 70), this sequence is correlated across most of the defined segments. The correlation and interpretation of the southern most part of this sequence represents one of the most challenging and uncertain areas of the Roghi Mountain outcrop. The correlation of this sequence is based on a very limited amount of outcropping layers, therefore much of the interpretation is based on the projection of different layer groups. Consequently, the correlation of Sequences 4 can be contested, as it is mostly based on the lack of any prominent features, as can be observed in other parts of Roghi Mountain.

Sequence 4 is interpreted to consist of the gently dipping beds of layer group Ib, IId, IIe and IIId (Figure 65 and Figure 66). Layer group IIe and IIId dip at an angle of 15° with a relatively similar dip direction (220-210°) and the thickness of these layers is quite similar in the different segments mentioned. The thick beds of layer group Ib and IId (Figure 65 and Figure 66) is challenging to interpret because no clear bedding is visible, therefore the geometries of these two layer groups is uncertain.

Except for the for layer groups IIe and IIId there are not any clear layers outcropping near the top of the mountain. This suggest that the depositional sequences loses energy northward, as the vegetated areas are assumed to be dominated by finer grained deposits. However, the lack of outcropping layers also allows for several interpretations. Either Sequence 4 carries across the entire top of Roghi Mountain, (as presented in Figure 68 and Figure 70), a viable interpretation when projecting the two layer groups through the mountain. This is further strengthened by the observation that no clear displacement is visible for the SRF and CRF faults beyond the unconformity marked in Figure 68 and Figure 70. Alternatively Sequence 4 truncates against the CRF and Sequence 2 layers continue further up the vertical succession. This would also imply that Sequence 2 experienced a decrease in depositional energy up the vertical succession.

5.2.5 Sequence 5

This sequence is composed of the layer group VIIIa (Figure 65 and Figure 66). The beds of layer group VIIIa is the most gently dipping layers of all layers groups defined for Roghi

Mountain. This suggest that Sequence 5 is the youngest deposits in relation to the sequences defined for Roghi Mountain. The bed structure and lithology observed in this sequence (described in chapter 3.1.2.3) suggest that this sequences sourced from a different depositional system than the other sequences.

5.3 Geological Contacts

From the correlation of these five sequences, three contacts have been identified within the Roghi Mountain sedimentary sequences.

1. Beds of Sequence 2 and 3 have an angular contact with beds of Sequence 1, this contact can be identified visually as the CRF.
2. Beds of Sequence 1,2 and 3 appear truncated against beds of Sequences 4.
3. Beds of Sequence 1 and 4 are truncated against beds of Sequences 5.
4. Beds of Sequence 3 are expected to onlap Sequence 2, this contact is however not visible in the outcrops of Roghi Mountain.

Of these three contacts only the first contact was interpreted as a fault, the other two are regarded as depositional contacts.

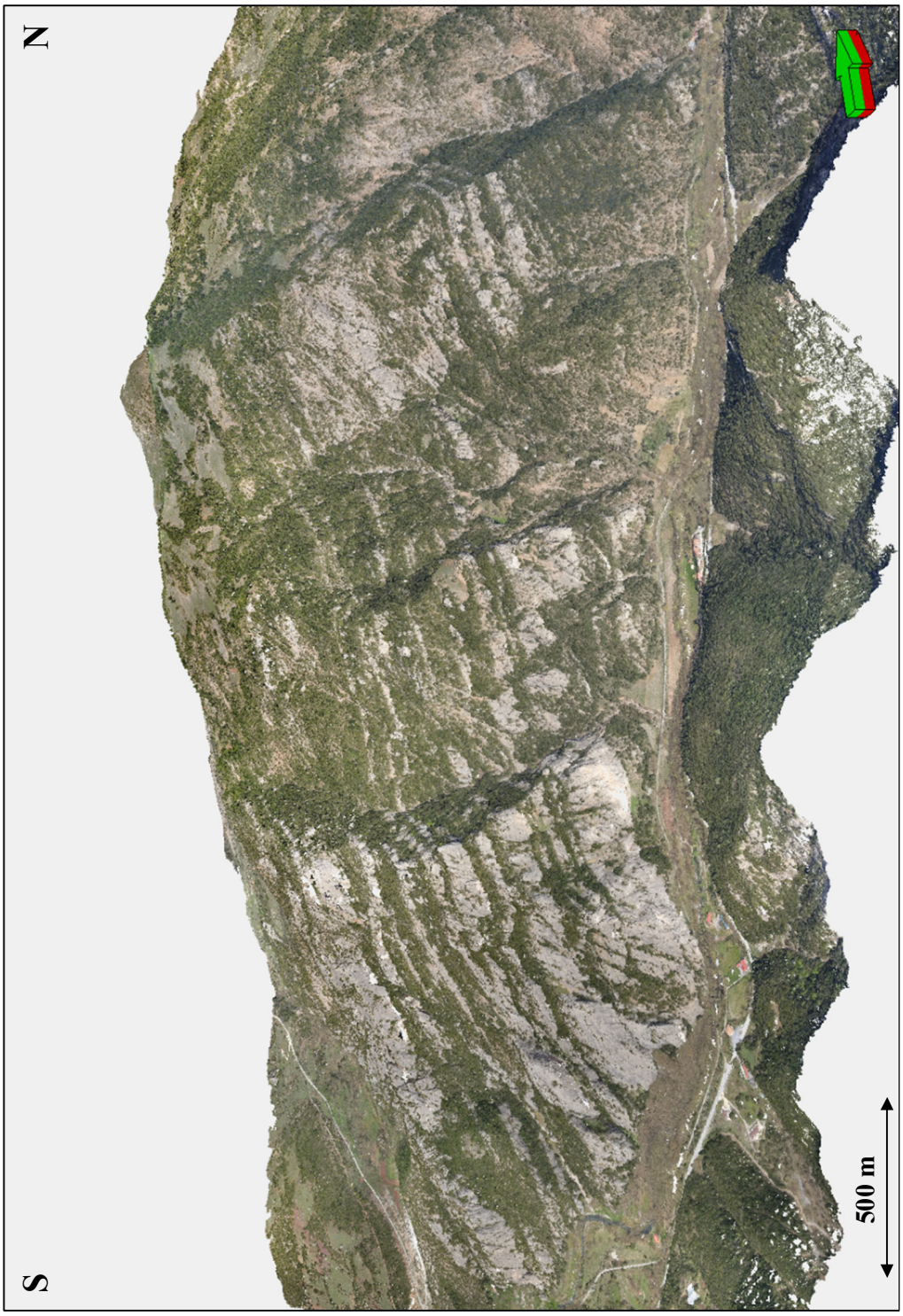

Figure 67 LiDAR representation of eastern profile of Roghi Mountain.

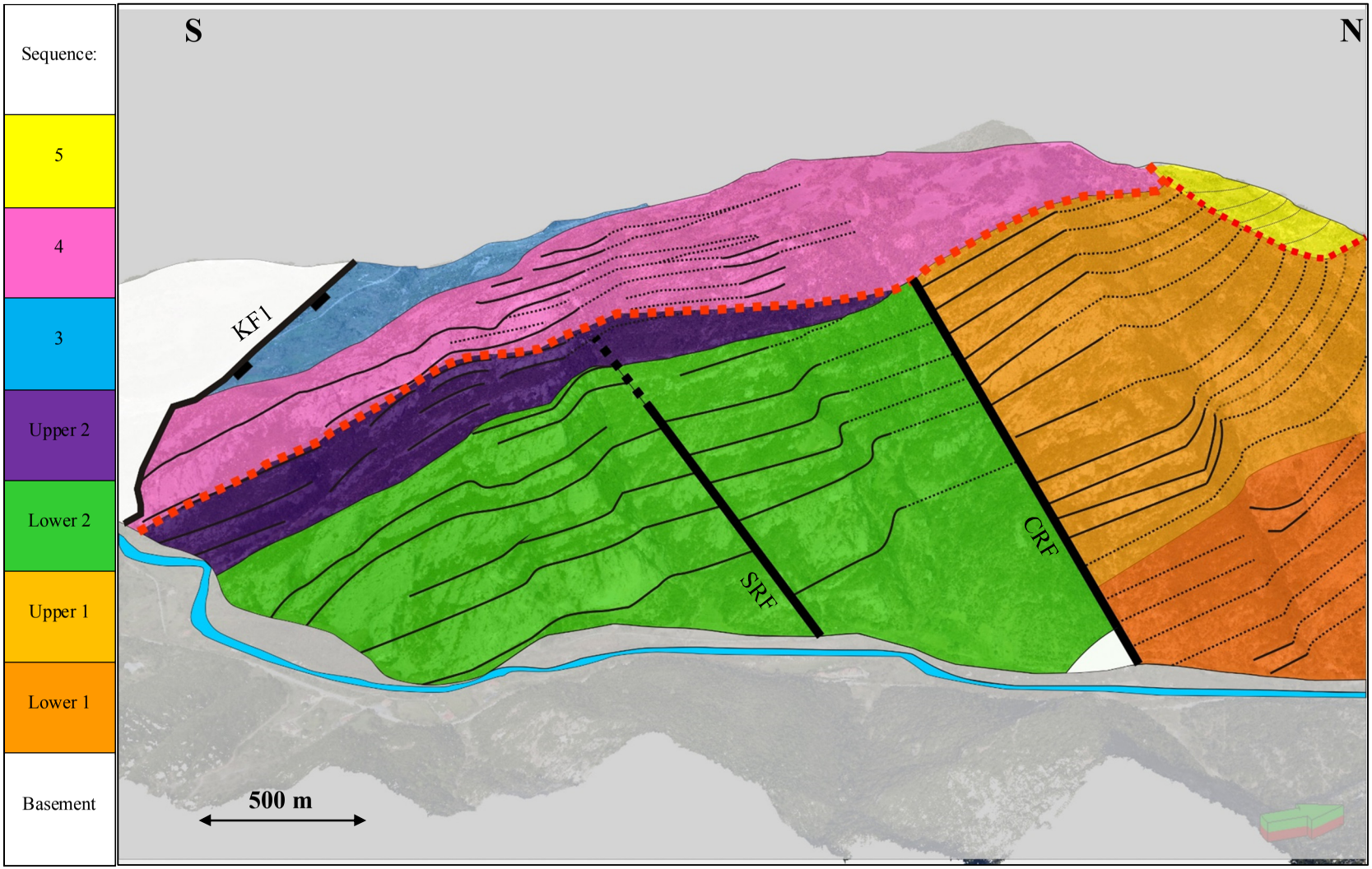

Figure 68 Interpreted sequences of Roghi Mountain, same view perspective as in Figure 67.

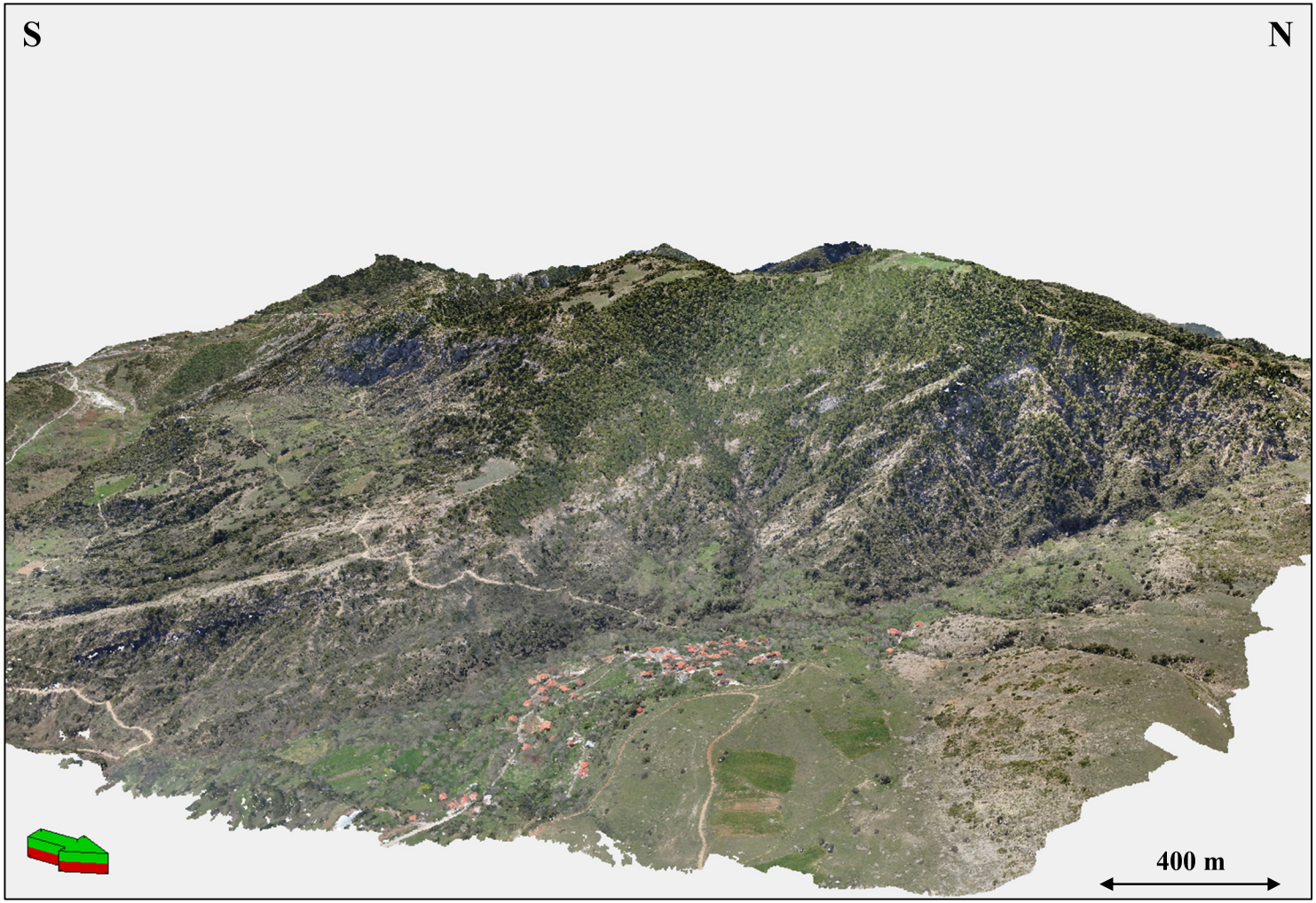

Figure 69 LiDAR representation of western profile of Roghi Mountain. Image is mirrored for easy comparison with Figure 68.

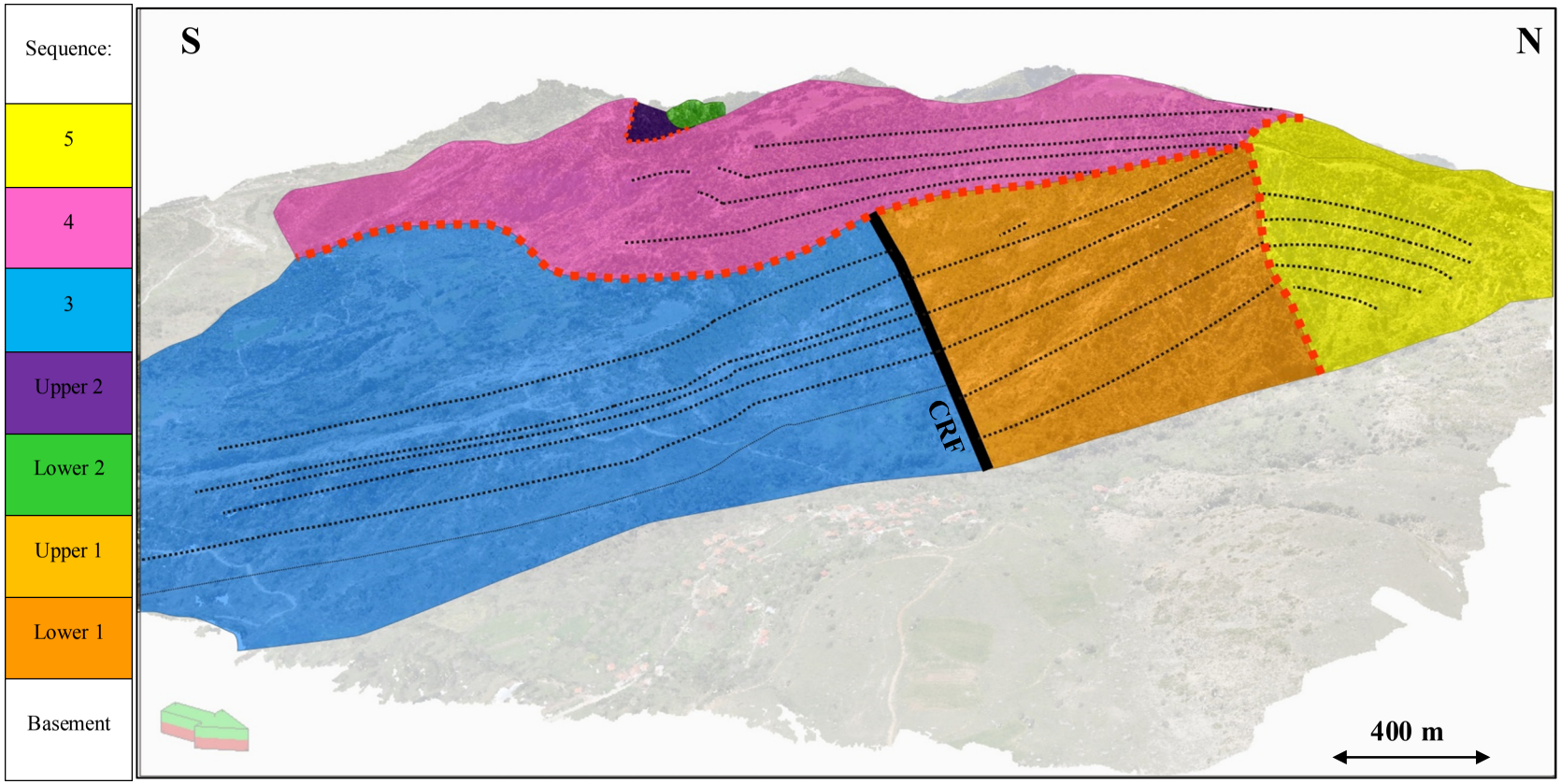

Figure 70 Interpreted sequences of Roghi Mountain, same view perspective as in Figure 69.

Chapter 6: Model

Creating a complete 3D model of Roghi Mountain that properly represents the outcrop requires a number of observations that are very accurate which reliable and consistent interpretations can be based on. This is critical as the quality of the model is only as good as the input data the model is built on. Creating a detailed model that is geological consistent requires a reliable interpretation as errors or misconceptions in the interpretation are quite revealing when attempting to model them in 3D space. By creating a 3D model of the study area that is geological reasonable helps to understand more about the study area, and it confirms or highlights flaws in the interpretation. The geological model was created with the aim of displaying the faults and internal relationships between the different sequences discussed in Chapter 5.

6.1 Modelling Workflow

To generate the 3D model a number of inputs are defined. This input consist of horizons, representing the different layer groups and unconformities, faults and a model boundary. After the model boundary is defined the "grid" is generated (as described in chapter 2.3.6). The gridding process generates a series of "model segments" (Figure 0). A "model segment" represents an area confined by faults and/or the model boundary. This allows for model inputs to be defined for each of the "model segments", i.e. allowing only certain horizons (representing layer groups) to be truncated against faults and not continue across the entire model. The input data is generally extrapolated over a much greater compared to how it was interpreted originally, when this data is then confined by a "model segment" it will be truncated towards the edges of the segment creating a consistent model where there are no empty grid cells caused by the lack of input data.

Not all horizons were to desired to be effected by faulting and continue across several "model segments", this required that the faulting relationships for each horizons had to be defined.

Another critical parameter that had to be determined prior to model construction was the horizon relationships. I.e. the relative age of the different sequences had to be established prior to modelling. This parameter controls the truncation of the different horizons (layer groups) in the model. The relative age of Sequence 1 to 5 was determined by the assumption that the most steeply dipping layers are the oldest, and layers are younger up the vertical succession as the dip angle decreases.

6.2 Structural Model Framework

The input data that represents the framework of the 3D structural model is based on three main inputs: 1) Planes representing the layer groups defined for each of the sequences in chapter 5.2; 2) Fault interpretations from field work, LiDAR data analysis and from previous work done in the study area; 3) Unconformities mapped in the field and inferred through the cross-segment correlation (chapter 5.2).

6.2.1 Faults

Faults were modelled as, more or less, planar features i.e. with a constant dip and strike (Figure 0). There are however two exceptions, which are the Vourikos and Roghi faults. These two faults are modelled with a vertical dip angle as these are transfer faults, however the strike of these faults undulates as these are not traced with certainty in the field and the published dip and strike directions are slightly ambiguous. Faults integrated in the model are presented in Table 3. The strike of the VTF was modelled similar to how it was interpreted by Syahrul (2014), this was done partly to make modelling easier as all of the east-west striking faults were connected to the SRF and VTF faults. One fault was created as a "dummy fault" to get an extra "model segment" such that the minor difference in layer geometries for layer group Ia in Sequence 2 could be modelled. This "dummy fault" does not have any displacement and acts only as a "model segment" boundary.

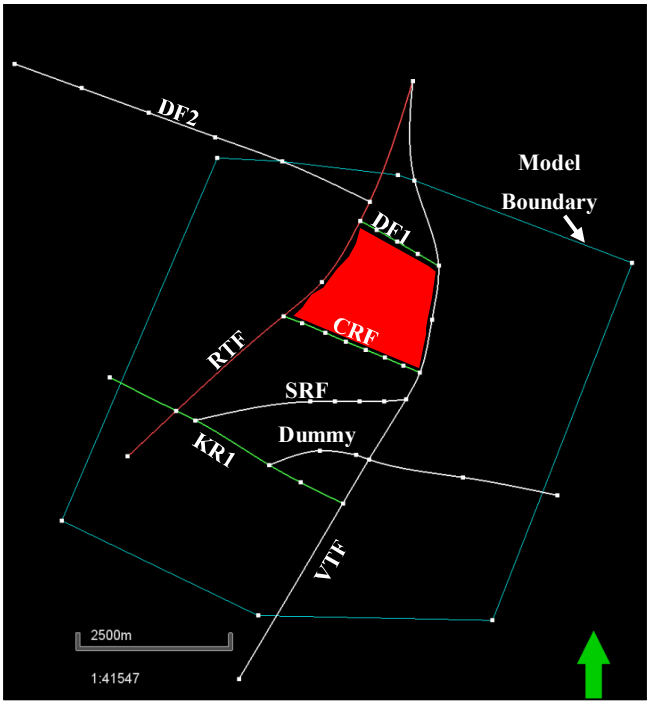

Figure 71 2D representation of fault model (top down view). Red polygon is an example of a "model segment".

Fault Name	Dip	Strike	Remarks
Kerpini Fault	40°	119°	Traced during field mapping.
Dhoumena Fault	48°	110°	From Dahman (2015).
Central Roghi Fault	56°	112°	Traced in field and during LiDAR data analysis. Previously mapped by Syahrul (2014) and Dahman (2015)
Southern Roghi Fault	73°	90°	Traced during LiDAR data analysis.
Vourikos Transfer Fault	~90°	~0-45°	From Syahrul (2014) and Dahman (2015).
Roghi Transfer Fault	~90°	~0-45°	From Syahrul (2014) and Dahman (2015).

Table 3 Representation of all faults integrated in structural 3D structural model.

6.2.2 Unconformities

Three basement/sediment unconformities were modelled as well as two sediment/sediment unconformities.

For the basement-sediment unconformities:

1) Between DF1 and CRF an unconformity plane with a dip direction of 170° and dip angle of 35° was created. This dip direction was assigned because of the mapped unconformity between Group 2 and the basement close to Roghi Mountain (further discussed in chapter 4.2.5), as well as from the contact trace visible in (Figure 45).
2) Between CRF and SRF an unconformity plane with a dip direction of 190° and dip angle of 22° was created. This is the same dip direction as the mapped unconformity between Group 2 and the basement close to Roghi Mountain (Figure 59).
3) Between the SRF and the KR1 the same unconformity plane as between the CRF and SRF was used, the only difference between these two planes is that south of the SRF

the unconformity plane is at 50 m higher elevation. This is based on the estimated displacement from the fault interpretation in chapter 5.1.4.

For the sediment-sediment unconformities:

1) A unconformity plane was generated for the base of Sequence 4. This horizon was created with a dip direction of 185° and a dip angle of ca 18°. This was not modelled as a plane, but followed the interpreted base of Sequence 4.
2) For the unconformity for Sequence 5 an exaggerated U-shape (Figure 0) was generated to make sure this surface would not interfere with any of the other surfaces during modelling. This unconformity was based on the interpreted unconformity at the base of Sequence 5.

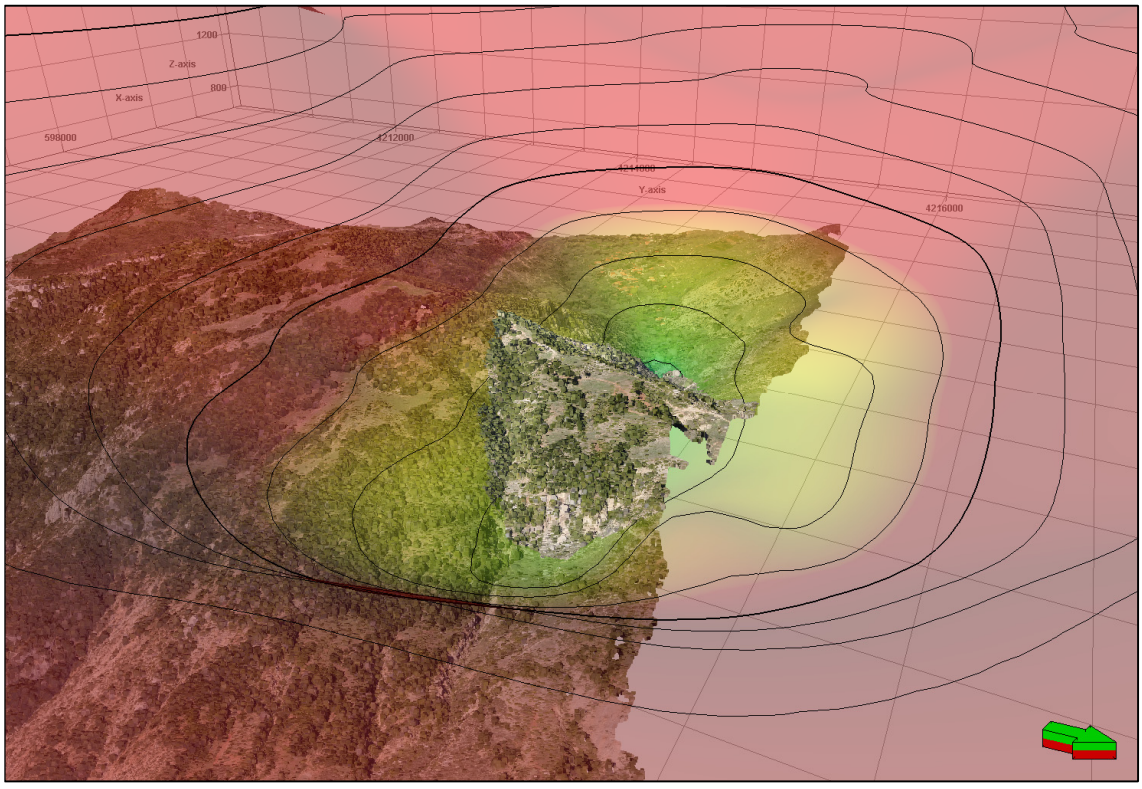

Figure 72 Display of the exaggerated U-shape modelled for the base of Sequence 5. Green arrow indicating north direction.

6.3 Modelling Challenges

There were two main issues when producing the 3D model of the structural interpretation of Roghi Mountain.

1) Firstly was representing the layers of Segment I (layer group Ia). The layer geometries of this segment were slightly different than the other correlated layers in Sequences 2. To be able to display this, a fault was created (Figure 0) such that Segment I could be singled out as a separate "modelling segment". This fault does not have any displacement and acts only as a "barrier" such that the layers of Segment I can be displayed with their proper geometries.
2) There was an issue in the model in regards to the zone division. Zones in Petrel E&P are defined between two model horizons (i.e. layers or unconformity surfaces). In the final model the aim was to colour code the different zones such that they represent the sequence correlation in chapter 5.2. However, the zonation process in Petrel E&P did not generated this desired effect initially as some "model segments" had more horizons than others. This confused the zonation process creating "linked" zones that carried throughout the entire model. This was resolved by inserting the same number of horizons in each "model segment" by coping the uppermost horizon of a "model segment" with a low number of horizons and adding them on top of each other. This resolved the problem and did not create any problems in the geological representation of the different layer groups.

6.4 3D Model Versus Interpretations And Correlations

displays the model of Roghi Mountain colour coded as the sequences in chapter 5.2. Not all details of the outcrop are captured in the model such as every individual bed of Roghi Mountain, but this was not regarded to decrease the value of the model in relation to the project objectives. Another reason for why these features were not included is based on the time it takes to make a detailed model, also the cell size in the grid the model was created in would need to be decreased which increases processing time greatly. Therefore, the modelled horizons are limited to the amount needed to display the layer groups accurately.

The most distinct discrepancy between the sequence interpretations displayed in Figure 70 and the model (Figure 0) is the "outcropping" of Sequence 2 on the western profile in the model of Roghi Mountain. Whether Sequence 2 actually outcrops on the western side of Roghi Mountain could not be determined with certainty form this study. The layer groups of Sequence 2 (for example IIa and IIb in Figure 28) are very thick, no such layers are visible where Sequence 2 supposedly should outcrop on the western side of Roghi Mountain. However, thickness analysis carried out on one of the uppermost layers of Sequence 2 (IIa5 in Figure 32) suggest that this layer thins out towards the west. This could explain why no thick, conglomeratic layers

are visible in the outcrop on the western profile. Figure 0, Figure 0, Figure 0 and Figure 0 exhibit the internal structure of Roghi Mountain.

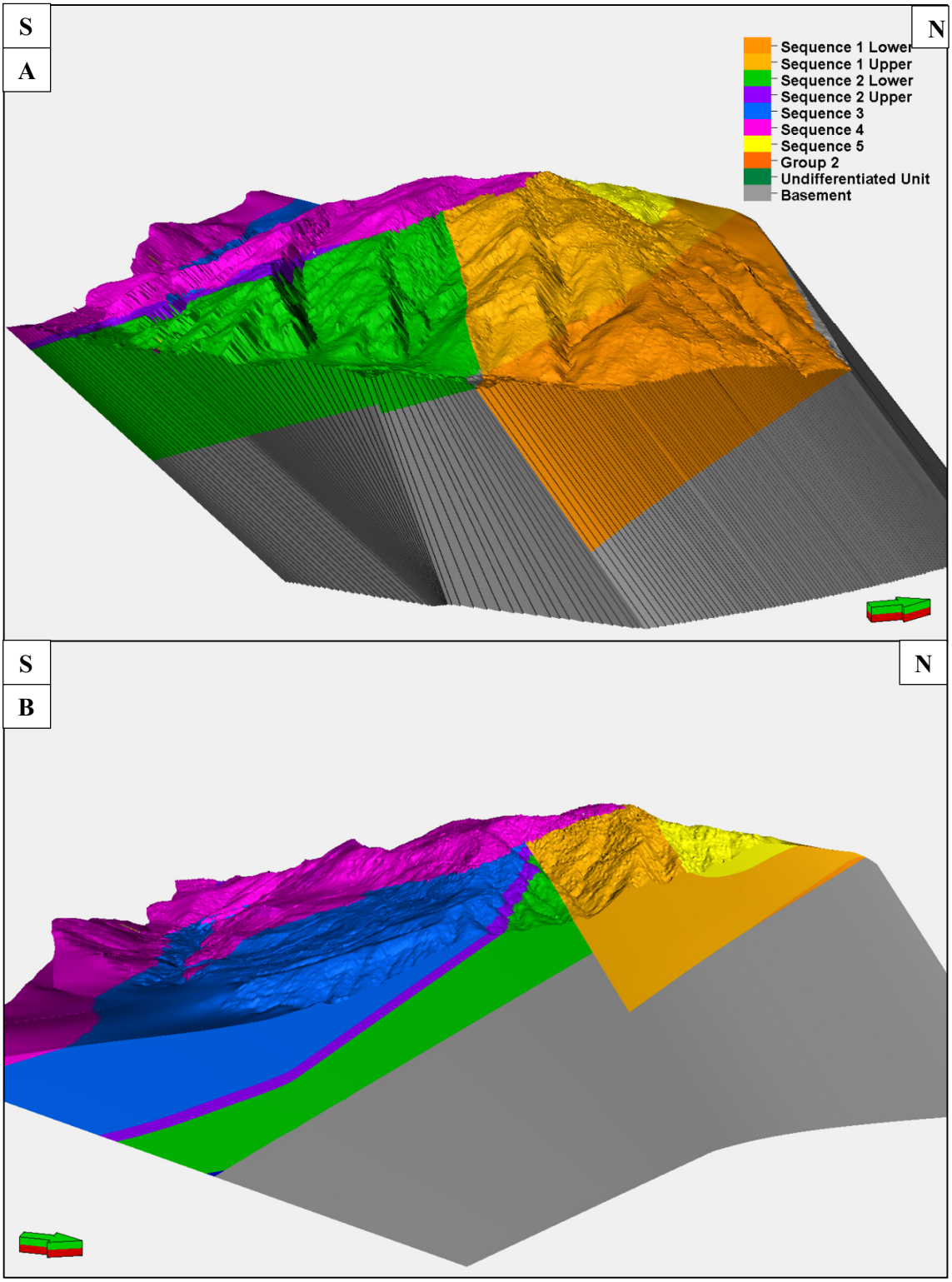

Figure 73 Overview of 3D structural model of Roghi Mountain, coloured in the same sequences as in chapter 5.2. A) represents eastern profile of Roghi Mountain while B) represents the western. The image of B) is mirrored such as north is towards the right.

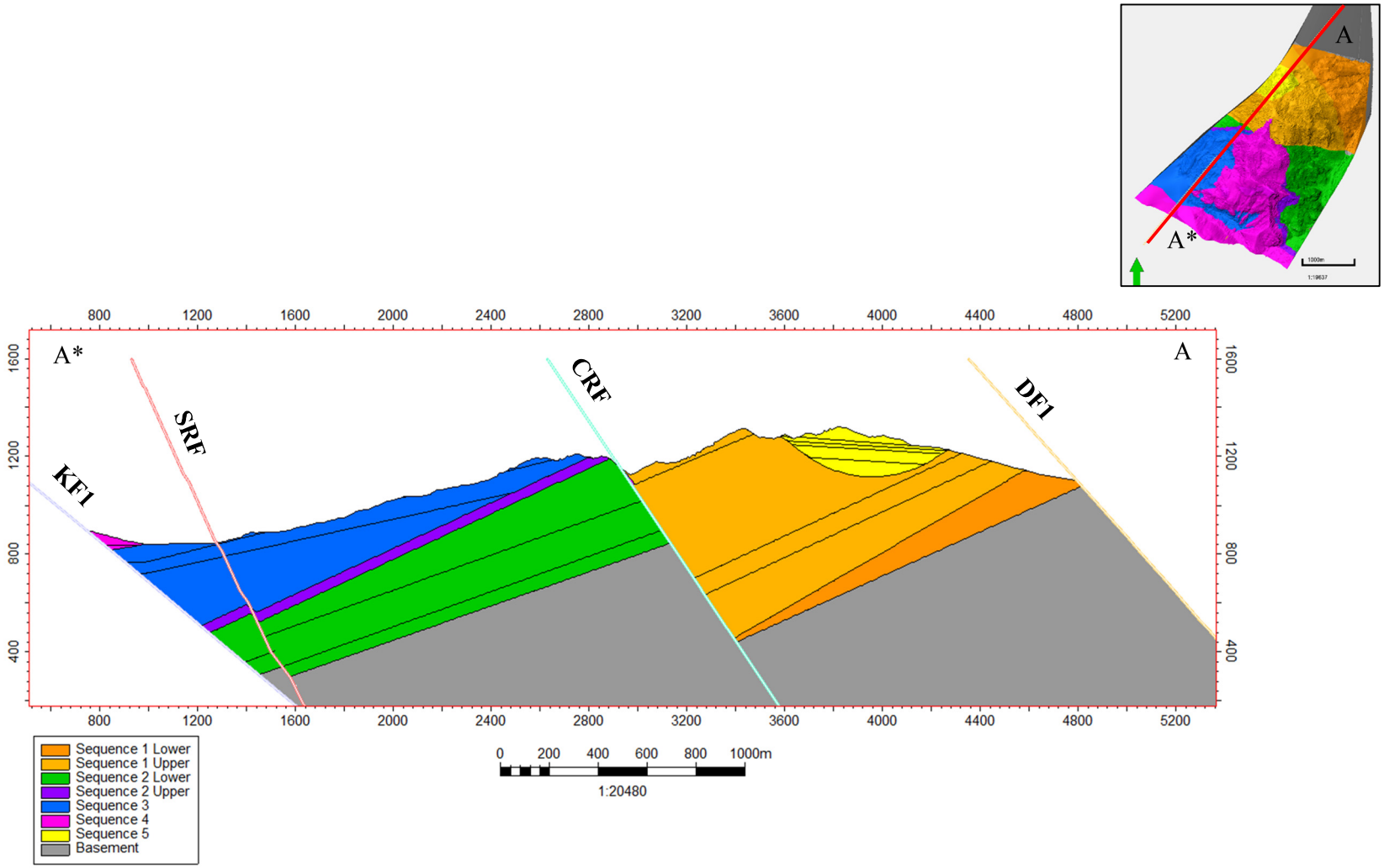

Figure 74 North-south cross section through structural model, direction of cross section indicated in the model overview (top right corner).

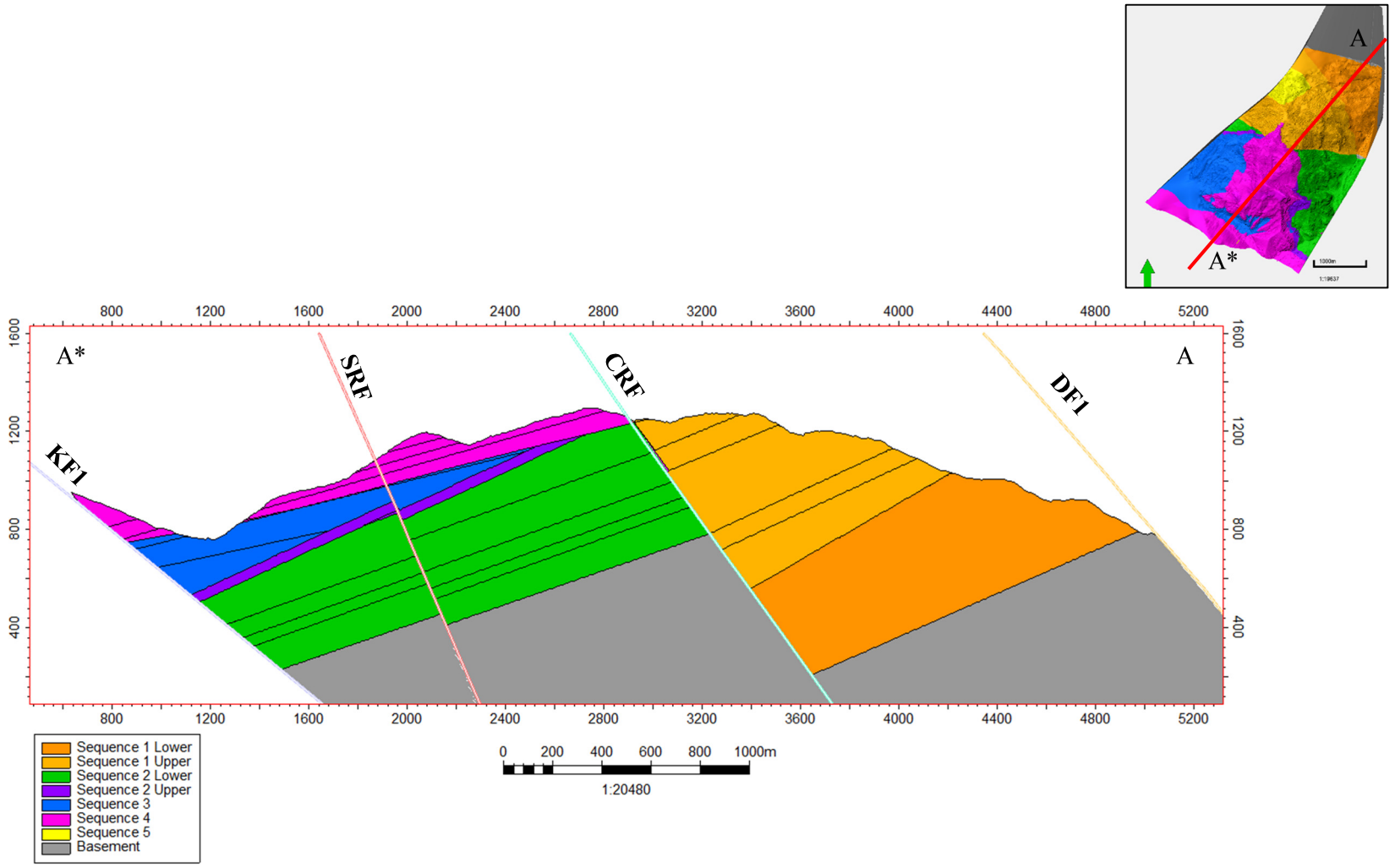

Figure 75 North-south cross section through structural model, direction of cross section indicated in the model overview (top right corner).

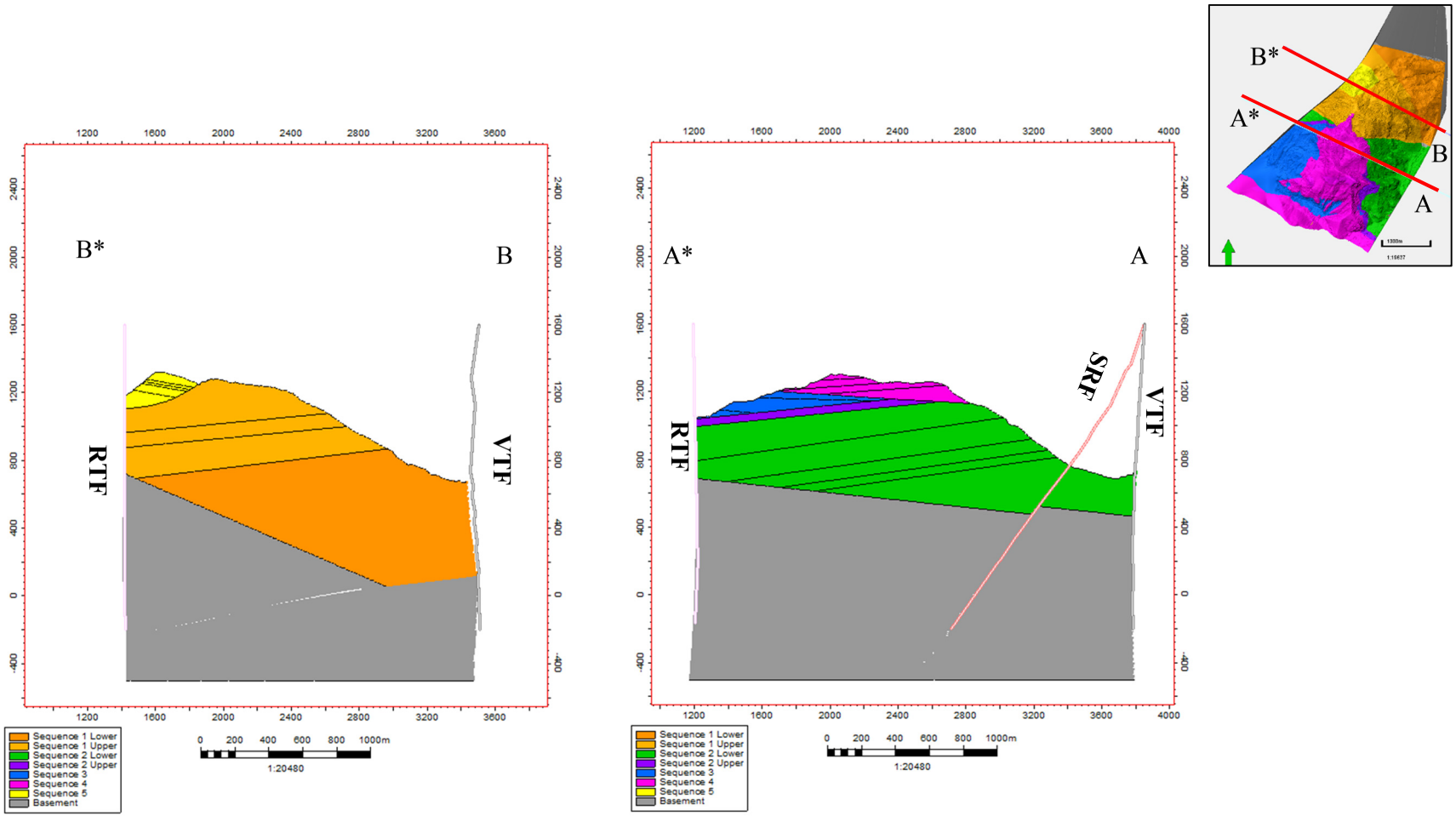

Figure 76 East-west cross sections through structural model, direction of cross sections indicated in the model overview (top right corner).

Chapter 7: Discussion and Evolutionary Model

Through this chapter the workflow and interpretations made in this project is discussed, and an evolutionary model based on all the structural features and defined stratigraphic sequences interpreted in Roghi Mountain is presented.

7.1 Interpretation and Modelling of a LiDAR Dataset in Petrel E&P

Petrel E&P (2014 version) was not suited to handle LiDAR data without the use of the PointCloudViz plugin. Developing a workflow for interpretation and analysis of the LiDAR dataset proved challenging, as no typical seismic interpretation tools could be utilized. However, once the interpretations were complete, the structural modelling tools of Petrel E&P could be used with relative ease to construct the structural model. The challenges faced in modelling were not directly linked to the LiDAR data.

Petrel E&P could be used as an excellent tool for interpretation and modelling based on LiDAR data if some additional features could be added, either to Petrel E&P itself or to an plugin. Some examples of possible features could be:

- Improved data import.
- A standardized set of tools for interpretation similar to those of seismic interpretation.
- Tools to downscale, and segment, point clouds.

7.2 Structure of Roghi Mountain

Creating a 3D model based on interpreting the LiDAR data provided a useful tool for evaluating the interpreted geometries of the sedimentary sequences of Roghi Mountain. The model displays a decreasing dip angle of the sedimentary beds moving up the vertical succession (Figure 74 and Figure 75) which is typical of syn-rift deposition. There are however some assumptions made for the geological interpretation and modelling of Roghi Mountain:

1) The sedimentary layers have been treated as planar features.

This is most likely not true, as alluvial deposits often are point sourced and therefore the geometries (for example thickness and bedding dip) can fluctuate for a individual bed as one follows the bed over a distance. For this project the scale of the alluvial fan deposits are interpreted to be so large (based on the massive exposed conglomerate beds of over 50 m

thickness), and the correlation over a relative small distance, such that this will not undermine the interpretations and model created for Roghi Mountain.

Two assumptions have been made in regards to the basement configuration:

1) The basement unconformities are planar features, i.e. the basement is considered to be a smooth surface in contact with the overlying sedimentary sequences.
2) The geometries of the unconformity is similar to that observed for the rest of the Kerpini Fault block.

By assuming the basement unconformity underneath the Roghi Mountain sediments follows the geometries of the unconformity in the rest of the Kerpini Fault Block, the unconformities underlying Sequence 1 and 2 increase significantly from east to west (Figure 75). No evidence has been found to support these assumptions, and the unconformities might actually have a very different geometry since Roghi Mountain appears to be situated in a minor fault block within the Kerpini Fault Block (i.e. in a intra-fault block).

7.3 Stratigraphic Sequences of Roghi Mountain

There is some uncertainty related to some of the assumptions and interpretation in relation to the five identified stratigraphic sequences of Roghi Mountain:

1) The alluvial fan deposits of Sequence 1, 2 and 4 are assumed to be deposited with the initiation of the Kerpini Fault and sourced from the ancient Vourikos River.

This is based on previous work (Collier and Jones, 2004; Dahman, 2015; Ford et al., 2013; Syahrul, 2014), and supported by the thickness analysis showing that layer groups thicken towards the south-southeast.

2) The relative age between Sequence 1 and 2.

Initially Sequence 1 was interpreted to be the oldest as the steepest beds of Roghi Mountain are interpreted to be a part of this sequence. However, when observing the structural elements of Roghi Mountain, the relative age of the CRF is important for understanding the age relationship between Sequence 1 and 2. If Sequence 1 actually is the oldest stratigraphic unit, then the CRF must have formed prior to the deposition of Sequence 2. However, this appears unlikely as the beds of Sequence 1 would then be expected to truncate against the basement. A more likely interpretation is that Sequence 1 and 2 are conformable, the CRF displaces the two sequences causing, what appears to be, an abrupt facies change between Sequence 1 and 2

(trace of the CRF). Since Sequence 2 is interpreted to be in the hanging wall of the CRF, this implies that the Sequence 1 actually overlays Sequence 2. The beds of Sequence 1 are only the steepest dipping beds of Roghi Mountain because of the increased rotation caused by the CRF fault.

3) The CRF and SRF terminate at the base of Sequence 4.

The lack of outcropping beds at the upper part of Roghi Mountain complicates this interpretation. If the CRF and SRF actually continue through the entire vertical succession of Roghi Mountain, then the part of Sequence 4 that is north of the CRF is then actually a part of Sequence 1. This interpretation could then infer that the CRF fault could be older than the beds interpreted as Sequence 4.

4) The apparent difference between the beds of the eastern and western profiles can be explained by facies changes occurring in the east-west direction.

This is based on the variations observed in the thickness analysis of layers Ia2, IIa5, IVb1.

7.4 Proposed evolutionary model

The evolution of the five stratigraphic sequences of Roghi Mountain can be described in six phases. The source of most of the alluvial sequences are assumed to come from the ancient Vourikos River.

7.4.1 Phase 1

As accommodation space was generated from the initiation of Kerpini Fault, alluvial sediments of Lower Sequence 2 filled the half graben (Figure 79). The Kerpini Fault is assumed to grow rapidly, causing the thick massive conglomeratic beds of Sequence 2 to be deposited. Moving northwards the depositional energy decreases. Towards the end of the Phase 1 there is a minor erosion event and Upper Sequence 2 is deposited.

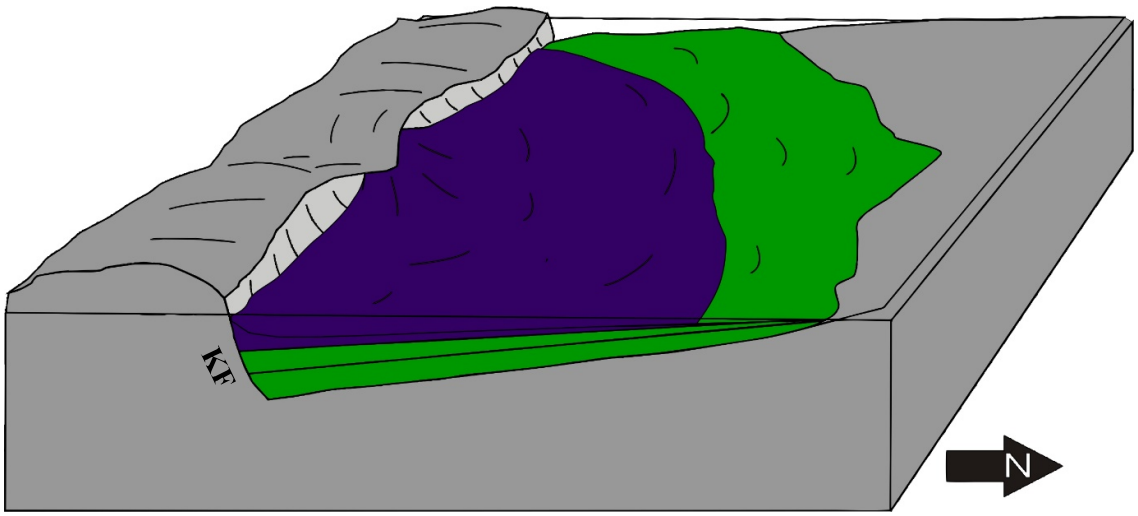

Figure 78 Phase 1 of the evolution of Roghi Mountain is dominated by the deposition of Sequence 2. Figure not to scale.

7.4.2 Phase 2

The Kerpini Fault continued to grow rapidly and Sequence 1 was deposited (Figure 79). Thick conglomeratic beds were deposited, yet the depositional energy of the system might have changed slightly causing the deposited beds to appear more chaotic.

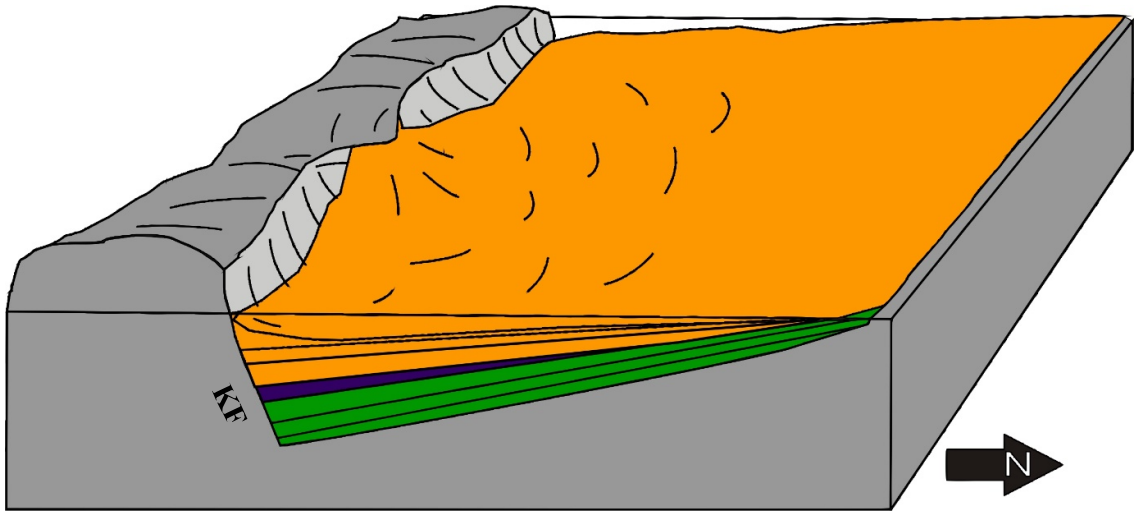

Figure 79 Phase 2 of the evolution of Roghi Mountain. As the Kerpini Fault continued to grow Sequence 2 was deposited. Figure not to scale.

7.4.3 Phase 3

At Phase 3 the displacement shifted northward and the CRF (and SRF but not marked in the figures of this chapter) fault became active down-throwing the sedimentary units north of the fault, and at the same time increasing the rotation of the beds of Sequence 1 relative to the beds of Sequence 2. After the CRF was active, an extensive erosion event occurred across the half graben that removed a significant amount of the, at this point, faulted Sequence 1 and 2 (Figure 80).

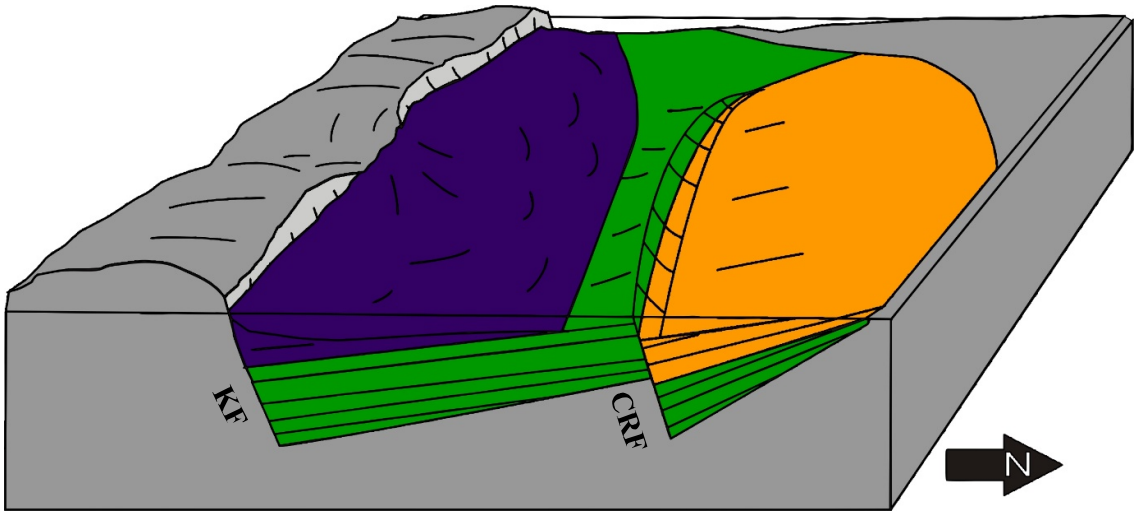

Figure 80 Phase 3 of the evolution of Roghi Mountain. At this stage, the CRF developed and eventually became inactive, then followed erosion of Sequence 1 and 2 across the half graben. Figure not to scale.

7.4.4 Phase 4

During Phase 4, the Kerpini Fault started growing again and accommodation space was generated. Sequence 3 was then deposited (Figure 81), possibly from a different sediment source than Sequence 1 and 2. Then followed the deposition of Sequence 4 covering the underlying sequences. Sequence 3 and 4 could be conformable as these two sequences appear to have experienced the same amount of rotation.

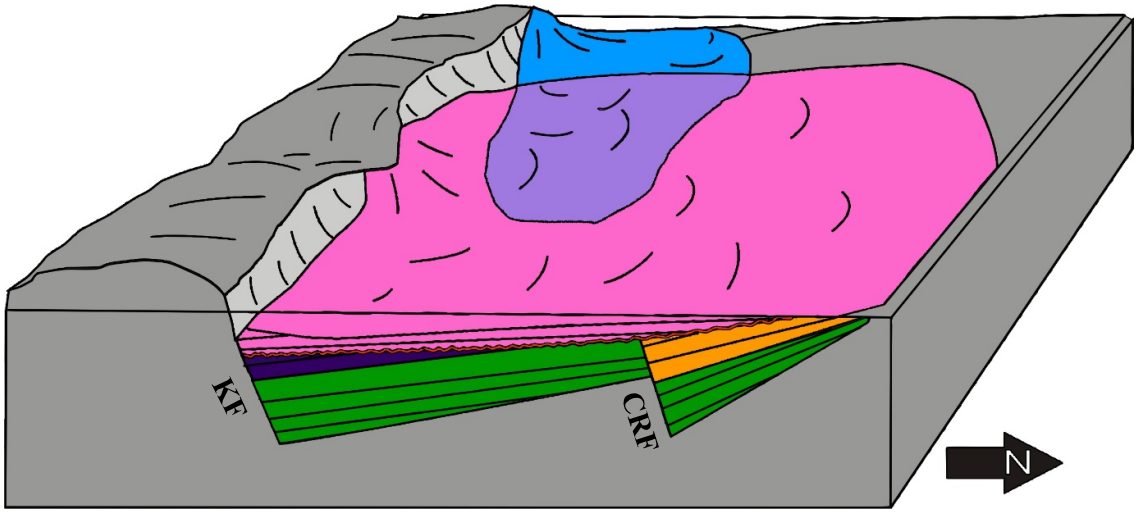

Figure 81 Phase 4 of the evolution of Roghi Mountain. Sequence 3 (marked in blue) is deposited during this stage, possibly from a different source than the underlying sequences. After a short time Sequence 4 covers most of the half graben.

7.4.5 Phase 5

At this phase the Kerpini Fault as become inactive, all of the accommodation space in the Kerpini Fault Block has been filled and there is a shift in the depositional system. The fault block might have experienced a slight uplift in the west, causing drainage systems of the fault block to develop in the west to east direction. At this stage Sequence 5 is deposited (Figure 82) (Dahman, 2015; Syahrul, 2014).

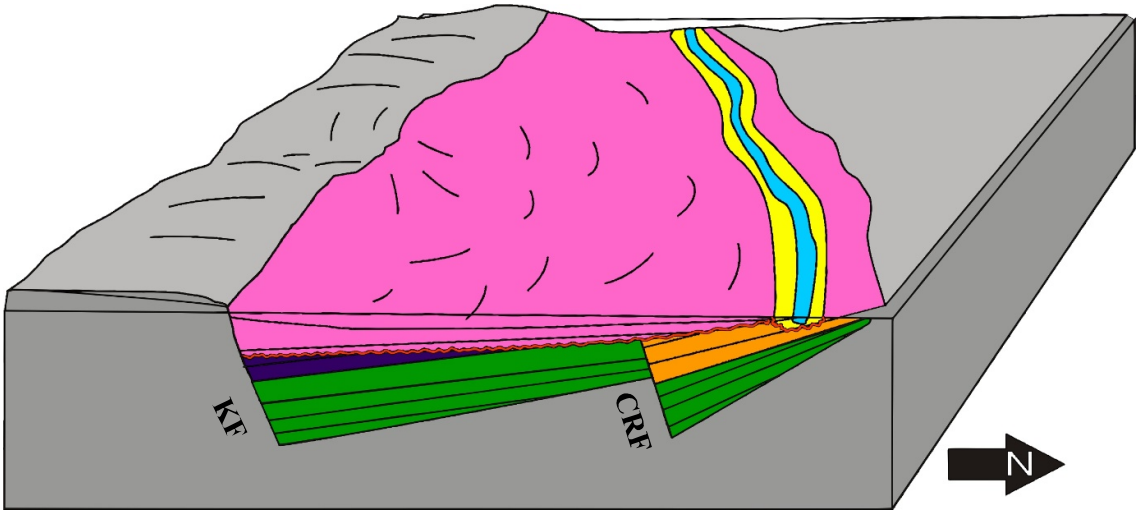

Figure 82 Phase 5 of the evolution of Roghi Mountain. The Kerpini Fault becomes inactive and the accommodation space of the fault block is filled. This, combined with a uplift in the western province of the fault block causes a shit in the depositional system and Sequence 5 is deposited as a more fluvial dominated unit compared to the prior sequences.

7.4.6 Phase 6

Following Phase 5 there was an extensive erosion as the whole region from Kalavryta towards the coast was uplifted (Flotté et al., 2005; Ford et al., 2013; Sorel, 2000). The relative age of the transfer faults (RTF and VTF) could not be determined from this study, but it can be assumed to have formed in relation to the strain experienced on the region due to this uplift. This strain generated the north-south transfer faults creating the Roghi Mountain intra-fault block. Massive erosion occurred at in the Kerpini Fault Block and eventually left the Roghi Mountain outcrop, as it is visible today (Figure 83).

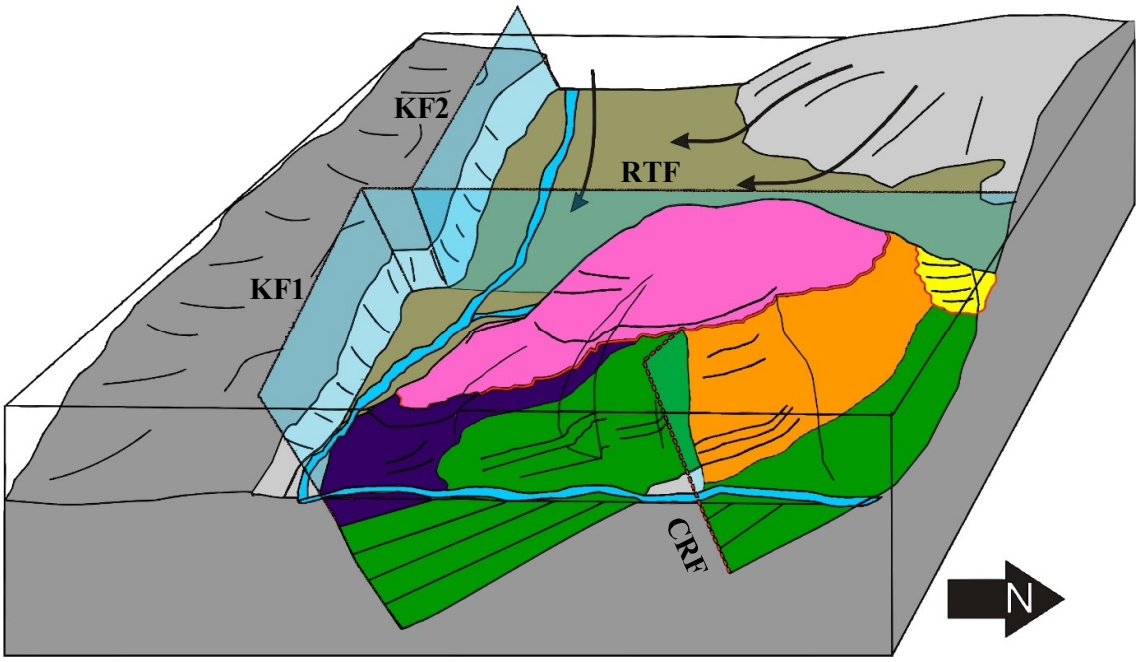

Figure 83 Phase 6 of the evolution of Roghi Mountain. Massive erosion dominated the Kerpini Fault Block at this stage and left the different sequences exposed as they are visible today. Drainage systems of the fault block follows the KF1, KF2 and RTF fault traces. Figure not to scale. Fault planes marked for the various faults of the area. Arrows indicating erosion and drainage.

7.5 Conclusions

Key conclusions from this project:

- A workflow for the interpretation, analysis and modelling of LiDAR data in Petrel E&P was generated.
- The structural interpretation and 3D modelling suggest that the Roghi Mountain deposits are in fact syn-rift deposits with evidence of growth strata and syn-depositional unconformities.
- Supporting previous work (Dahman, 2015; Syahrul, 2014), the CRF crosses Roghi Mountain from east to west, the displacement of the fault is estimated to 750 m.
- A minor fault (SRF) has been identified on the eastern profile of Roghi Mountain.
- The stratigraphic succession of Roghi Mountain can be divided in five different sequences which describe the geological evolution of the syn-rift sedimentary sequence.
- One major syn-depositional unconformity has been identified at the base of Sequence 4.
- Thickness analysis of the LiDAR data suggest that there are facies changes occurring in the east-west direction across Roghi Mountain that can explain why beds deposited in the same depositional sequence appear differently from the eastern and western profiles.

References

Armijo, R., B. Meyer, A. Hubert, and A. Barka, 1999, Westward propagation of the North Anatolian fault into the northern Aegean: Timing and kinematics: Geology, v. 27, p. 267-270.

Armijo, R., B. G. C. P. Meyer, G. C. P. King, A. Rigo, and D. Papanastassiou, 1996, Quaternary evolution of the Corinth Rift and its implications for the Late Cenozoic evolution of the Aegean: Geophysical Journal International, v. 126, p. 11-53.

Avallone, A., P. Briole, A. Agatza-Balodimou, H. Billiris, O. Charade, C. Mitsakaki, A. Nercessian, K. Papazissi, D. Paradissis, and G. Veis, 2004, Analysis of eleven years of deformation measured by GPS in the Corinth Rift Laboratory area: C. R. Geosci., v. 336, p. 301-311.

Bell, R. E., L. C. McNeill, J. M. Bull, and T. J. Henstock, 2008, Evolution of the offshore western Gulf of Corinth: Bulletin of the Geological Society of America, v. 120, p. 156-178.

Bell, R. E., L. C. McNeill, J. M. Bull, T. J. Henstock, R. E. L. Collier, and M. R. Leeder, 2009, Fault architecture, basin structure and evolution of the Gulf of Corinth rift, central Greece: Basin Research, v. 21, p. 824-855.

Collier, R., and G. Jones, 2003, Rift Sequences of the Southern Margin of the Gulf of Corinth (Greece) as Exploration / Production Analogues, AAPG International Conference, Barcelona, Spain, AAPG Search and Discovery Article.

Collier, R., and G. Jones, 2004, Rift Sequences of the Southern Margin of the Gulf of Corinth (Greece) as Exploration / Production Analogues*.

Dahman, A., 2015, The Vouraikos Valley: an example of rift segmentation in the Corinth Graben, Greece, University Of Stavanger, Stavanger, 82 p.

Doutsos, T., and S. Kokkalas, 2001, Stress and deformation patterns in the Aegean region: Journal of Structural Geology, v. 23, p. 455-472.

Finnesand, S., 2013, Analysis of Structural Control in Fault Interactions and their Sediment accumulation in the Gulf of Corinth rift, Greece., University of Stavanger, Stavanger, 87 p.

Flotté, N., D. Sorel, C. Müller, and J. Tensi, 2005, Along strike changes in the structural evolution over a brittle detachment fault: Example of the Pleistocene Corinth-Patras rift (Greece): Tectonophysics, v. 403, p. 77-94.

Ford, M., S. Rohais, E. A. Williams, S. Bourlange, D. Jousselin, N. Backert, and F. Malartre, 2013, Tectono-sedimentary evolution of the western Corinth rift (Central Greece): Basin Research, v. 25, p. 3-25.

Fossen, H., 2010, Structural Geology: Cambridge, Cambridge University Press, 463 p.

Galloway, W. E., and D. K. Hobday, 1996, Terrigenous Clastic Depositional Systems, Applications to Fossil Fuel and Groundwater Resources, v. 2: New York, Springer-Verlag Berlin Heidelberg New York, 489 p.

Gawthorpe, R. L., and M. R. Leeder, 2000, Tectono-sedimentary evolution of active extensional basins: Basin Research, v. 12, p. 195-218.

Ghisetti, F., and L. Vezzani, 2005, Inherited structural controls on normal fault architecture in the Gulf of Corinth (Greece): Tectonics, v. 24, p. 1-17.

Hadland, S., C. Townsend, and A. Escalona, 2016, Geological Mapping And Investigation Into A Proposed Syn-Rift Alluvial Fan Deposit In The Kerpini Fault Block, Greece., EAGE Conference & Exhibition, Vienna, Austria.

Hemelsdaël, R., and M. Ford, 2014, Relay zone evolution: a history of repeated fault propagation and linkage, central Corinth rift, Greece: Basin Research, p. 1-23.

Hemelsdaël, R., M. Ford, F. Malartre, R. L. Gawthorpe, J. Charreau, and S. Sen, 2015, Rivers and Rifting: Evolution of a Fluvial System during Rift Initiation, Central Corinth Rift (Greece)*, AAPG 2015 Annual Convention and Exhibition, Denver, Colorado., Search and Discovery Article #30419.

Jackson, C. A. L., R. L. Gawthorpe, C. W. Leppard, and I. R. Sharp, 2006, Rift-initiation development of normal fault blocks: insights from the Hammam Faraun fault block, Suez Rift, Egypt: Journal of the Geological Society, v. 163, p. 165-183.

Jolivet, L., C. Faccenna, B. Huet, L. Labrousse, L. Le Pourhiet, O. Lacombe, E. Lecomte, E. Burov, Y. Denèle, J. P. Brun, M. Philippon, A. Paul, G. Salaün, H. Karabulut, C. Piromallo, P. Monié, F. Gueydan, A. I. Okay, R. Oberhänsli, A. Pourteau, R. Augier, L. Gadenne, and O. Driussi, 2013, Aegean tectonics: Strain localisation, slab tearing and trench retreat: Tectonophysics, v. 597-598, p. 1-33.

Jolivet, L., L. Labrousse, P. Agard, O. Lacombe, V. Bailly, E. Lecomte, F. Mouthereau, and C. Mehl, 2010, Rifting and shallow-dipping detachments, clues from the Corinth Rift and the Aegean: Tectonophysics, v. 483, p. 287-304.

Kolbeinsen, A., 2013, Analysis of Structural Controls in Alluvial Fan Deposition During Late Syn-rotational Faulting Phase in a Half-graben Rift System. The Gulf of Corinth, Greece., University of Stavanger, Stavanger, 69 p.

Laux, D., and A. Henk, 2015, Terrestrial laser scanning and fracture network charachterisation - perspectives for a (semi-) automatic analysis of point cloud data from outcrops: Z.Dt.Ges.Geowiss, v. German J. Geol., p. 166.

Leeder, M. R., G. H. Mack, A. T. Brasier, R. R. Parrish, W. C. McIntosh, J. E. Andrews, and C. E. Duermeijer, 2008, Late-Pliocene timing of Corinth (Greece) rift-margin fault migration: Earth and Planetary Science Letters, v. 274, p. 132-141.

Moretti, I., D. Sakellariou, V. Lykousis, and L. Micarelli, 2003, The Gulf of Corinth: An active half graben?: Journal of Geodynamics, v. 36, p. 323-340.

Morley, C. K., 1995, Developments in the structural geology of rifts over the last decade and their impact on hydrocarbon exploration: *in* J.J Lambise, ed., Hydrocarbon Habitat in Rift Basins: Geological Society Special Publication, v. No. 80, p. 1-32.

Mrlina, J., 2014, Do active transverse faults exist on the southern coast of Corinth rift?: Near Surface Geoscience 2014 - 20th European Meeting of Environmental and Engineering Geophysics.

Ori, G. G., 1989, Geologic history of the extensional basin of the Gulf of Corinth (?Miocene-Pleistocene), Greece: Geology, v. 17, p. 918-921.

Palyvos, N., F. Lemeille, D. Sorel, D. Pantosti, and K. Pavlopoulos, 2008, Geomorphic and biological indicators of paleoseismicity and Holocene uplift rate at a coastal normal fault footwall (western Corinth Gulf, Greece): Geomorphology, v. 96, p. 16-38.

Palyvos, N., M. Mancini, D. Sorel, F. Lemeille, D. Pantosti, R. Julia, M. Triantaphyllou, and P. M. de Martini, 2010, Geomorphological, stratigraphic and geochronological evidence of fast Pleistocene coastal uplift in the westernmost part of the Corinth Gulf Rift (Greece): Geological Journal, v. 45, p. 78-104.

Palyvos, N., D. Sorel, F. Lemeille, M. Mancini, D. Pantosti, R. Julia, M. Triantaphyllou, and P. M. De Martini, 2007, Review and new data on uplift rates at the W termination of the Corinth rift and the NE Rion graben area (Achaia, NW Peloponnesos): 11th International Congress, p. 412-424.

Rognmo, T., 2015, Sedimentary infill in the Kalavrita faulted block, south-central Gulf of Corinth, Greece, University of Stavanger, Stavanger, 92 p.

Rohais, S., R. Eschard, M. Ford, F. Guillocheau, and I. Moretti, 2007, Stratigraphic architecture of the Plio-Pleistocene infill of the Corinth Rift: Implications for its structural evolution: Tectonophysics, v. 440, p. 5-28.

Skourlis, K., and T. Doutsos, 2003, The Pindos Fold-and-thrust belt (Greece): Inversion kinematics of a passive continental margin: International Journal of Earth Sciences, v. 92, p. 891-903.

Skourtsos, E., and H. Kranis, 2009, Structure and evolution of the western Corinth rift, through new field data from the northern Peloponnesus, Geological Society Special Publication, p. 119-138.

Sorel, D., 2000, A Pleistocene and still-active detachment fault and the origin of the Corinth-Patras rift, Greece: Geology, v. 26, p. 83.

Stuveland, M. E., 2015, Kalavryta and Kerpini Fault Block: Investigation into correlation and nature of sub-horizontal layers; Corinth Graben, Greece., University of Stavanger, Stavanger, 111 p.

Syahrul, R. A., 2014, Fault Controlled Sedimentation: A Case Study of the Kerpini Fault, Greece, University of Stavanger, Stavanger, 142 p.

Taylor, B., J. R. Weiss, A. M. Goodliffe, M. Sachpazi, M. Laigle, and A. Hirn, 2011, The structures, stratigraphy and evolution of the Gulf of Corinth rift, Greece: Geophysical Journal International, v. 185, p. 1189-1219.